Nanofluidic Devices for Rapid Analysis of DNA and Proteins

by

Jianping Fu

M.S. Mechanical Engineering (2002)
University of California at Los Angeles

B.E. Mechanical Engineering (2000)
University of Science and Technology of China

Submitted to the Department of Mechanical Engineering
in Partial Fulfillment of the Requirements for the Degree of
Doctor of Philosophy in Mechanical Engineering

at the

Massachusetts Institute of Technology

June 2007

Signature of Author____
Department of Mechanical Engineering
April 2, 2007

Certified by____
Jongyoon Han
Department of Electrical Engineering and Biological Engineering
Doctoral Thesis Supervisor

Certified by____
Alan J. Grodzinsky
Department of Electrical Engineering, Mechanical Engineering
and Biological Engineering
Chairman, Doctoral Thesis Committee

Accepted by____
Lallit Anand
Chairman, Department Committee on Graduate Students
Department of Mechanical Engineering

Nanofluidic Devices for Rapid Analysis of DNA and Proteins

by

Jianping Fu

Submitted to the Department of Mechanical Engineering
on April 2, 2007 in Partial Fulfillment of the
Requirements for the Degree of Doctor of Philosophy
in Mechanical Engineering

ABSTRACT

Direct analysis of biologically-relevant entities such as nucleic acids and proteins offers the potential to outperform conventional analysis techniques and diagnostic methods through enhancements in speed, accuracy, and sensitivity. Nanofluidic systems with critical dimensions comparable to the molecular scale open up new possibilities for direct observation, manipulation and analysis of biomolecules (single or ensemble), thus providing a novel basis for ultra-sensitive and high-resolution sensors and medical diagnostic systems. Inspired by this concept, we have developed a new class of nanofluidic filter devices and have implemented them as controllable molecular sieves for rapid analytical separation of various physiologically-relevant molecules such as dsDNA and proteins. In addition, we have conducted theoretical studies of molecular sieving process in the context of periodic free-energy landscapes created by the patterned nanofluidic filter arrays. The kinetic model constructed based upon the equilibrium partitioning theory and the Kramers rate theory properly describes the field-dependent sieving behavior, presenting notable progress beyond the existing equilibrium model in conventional gels. In this thesis, we have further developed a microfabricated anisotropic sieving structure consisting of a two-dimensional periodic nanofluidic filter array (anisotropic nanofilter array, ANA). The designed structural anisotropy in the ANA causes different-sized biomolecules to follow distinct migration trajectories, leading to efficient continuous-flow separation. Continuous-flow separation of dsDNA and proteins covering broad biological size scales were achieved within a few minutes, thus demonstrating the potential of the ANA as a generic molecular sieving structure for an integrated biomolecule sample preparation and analysis system.

Thesis Supervisor: Jongyoon Han

Title: Karl Van Tassel Career Development Associate Professor, Department of Electrical Engineering and Computer Science, Department of Biological Engineering

Thesis Committee Chairman: Alan J. Grodzinsky

Title: Director, Center for Biomedical Engineering, Professor of Electrical Engineering, Mechanical Engineering and Biological Engineering

Acknowledgments

I owe a debt of gratitude to many people who have provided support and friendship over the course of my doctoral research. I would first like to thank my thesis advisor, Professor Jongyoon Han, for his guidance, support, and encouragement. It was Professor Han who guided me into the exciting field of micro/nanofluidic BioMEMS. I also like to give special thanks to him for his insights of the sieving properties of the nanofluidic filter structure. His insights helped build the foundation of this whole thesis. I would also like to thank the other members of my thesis committee, Professor Alan Grodzinsky, Professor Paul Matsudaira, and Professor William Deen, for being encouraging and supportive for my doctoral research. I also like to thank Professor Joel Voldman and Professor Scott Manalis for their help in other different ways.

It has been my pleasure to work with my fellow graduate students in the Prof. Han's laboratory. Especially I like to thank Pan Mao for his help with the scanning electron microscopy and Ying-Chih Wang for his help setting up the fluorescence microscopy. I would also like to thank other lab members: Hansen Bow, Reto B. Schoch, Yong-Ak Song, Jeong Hoon Lee, Sung Jae Kim, Philip Dextras, Aniruddh Sarkar, Vincent Liu, Noel Reyes-Gonzalez, and Arnaud Le Coguic. Special thanks go to some wonderful undergraduate and visiting students who have worked with me: Craig Rothman, Juhwan Yoo (from Caltech), Eung Seok Park (from Korea Univ.) and Hyung-Dong Lee (from Korea Univ.). I also like to thank my fellow graduate students on the 8th floor of MIT building 36 (the Research Laboratory of Electronics): Brain Taff, Mike Vahey and Salil Desai. They have been helpful in different ways over the years.

I must acknowledge the generous financial support from NIH (EB005743), DuPont-MIT Alliance, NSF (CTS-0347348) and Singapore-MIT Alliance (SMA-II, CE program). The MIT Microsystems Technology Laboratories is acknowledged for support in fabrication of the nanofluidic devices.

All this would not have been possible without the love and support of my parents and my sister. My parents have always sacrificed to put the concerns and welfare of their children before their own. Lastly I would like to express my love and gratitude to my wife, Yangwei Situ, who has helped me in more ways than I can describe. Thanks for her understanding, support, encouragement, and love. I owe her so much! I would like to dedicate this thesis to my loving wife and our coming daughter in the summer.

Table of Contents

List of Figures

Chapter 1

Introduction

1.1 Bioseparation for biological and biomedical applications

The ability to purify, separate and identify biomolecules accurately and efficiently out of a complex biological sample is of utmost importance in modern biology and biomedical engineering [1-3]. In the new challenge of systems biology, one needs to separate and identify many different proteins, polysaccharides and other biologically-relevant macromolecules from cell extracts or other complex biological fluids (such as human blood serum) [3]. This separation / identification should be done with sample amount as small as possible. Because of large number of analytes involved in the analysis, it is essential to make the biomolecule analysis process automatic, requiring minimum human intervention. None of the conventional separation technologies satisfies all these requirements. Gel electrophoresis and chromatography techniques routinely used for separating proteins based on size or other chemical properties are generally slow, hard to automate and requiring bulky equipments [1, 2]. Capillary electrophoresis (CE) is a fast analysis technique but only separates biomolecules based on the charge-to-size ratio of the biomolecule, and cannot analyze neutral biomolecules [4]. The microfluidic biomolecule separation systems demonstrated a lot of success in miniaturizing and automating biomolecule analysis processes [5-8], such as DNA sequencing, but most microfluidic biomolecule separation systems adopt the same random nanoporous sieving materials in their separation systems, inheriting the limitations of conventional techniques.

The common, underlying problem of all of these biomolecule separation and analysis techniques is the lack of engineering control for the molecular sieving process. For purification and separation of biomolecules, various kinds of nanoporous materials, such as polymeric gels, are used extensively as molecular sieve matrixes. These gels provide nanometer-sized pores that are desirable for molecular sieving and filtering, but their random physical and chemical properties are hard to control and optimize, which prevent controllable experimental studies and theoretical modeling. In this proposed thesis, an artificial molecular sieve with designed shape and size is proposed to replace random nanoporous sieve materials, so that a direct control over the molecular sieving process is possible. Microfabricated nanofluidic structures provide promising opportunities to serve as regular molecular sieves. Unlike random polymer gels, we can precisely engineer the size and shape of nanofluidic molecular sieves, typically with the accuracy of ~1 nm. The regularity of nanofluidic molecular sieves makes it possible to construct theoretical models for the molecular sieving processes. Finally, the solid molecular sieves (either Si or glass based) are more mechanically and chemically robust than organic polymer-based materials; they are re-useable and can endure harsh solvents and extreme pH conditions.

1.2 Micro/nanofluidic sieving structures for biomolecule separation

Gel filtration chromatography and gel electrophoresis are the two most commonly used techniques for separation of biologically-relevant macromolecules (such as nuclei acids and proteins) based on size [1, 2]. Both techniques use gelatinous materials consisting of cross-linked three-dimensional pore networks where the sieving interactions with the migrating biomolecules determine the separation efficiency. Both gel filtration chromatography and gel electrophoresis represent the current standard for size-based separation of biomolecules in laboratories. However, poor separation resolution in gel filtration chromatography and difficult sample recovery with gel electrophoresis make neither method optimal in separating complex biological mixtures for downstream analysis. Recently, various microchip-based separation systems had been developed by using liquid or solid polymeric gel materials as sieving media contained in microchannels [5-8], and such systems had demonstrated fast separation of various biologically-relevant macromolecules (*e.g.*, DNA, proteins and carbohydrates) with high resolution. However, there are still major disadvantages associated with these microchip-based separation systems. First, the foreign sieving matrices pose intrinsic difficulties for the integration of multi analytic steps into an automatic bioanalysis microsystem. And second, the microchip-based systems demonstrated so far are limited for analytical separation of biomolecules. Harvesting purified biomolecule samples for downstream bioanalysis with the microchip-based systems is not trivial, which clearly limits their usage for the sample preparation purpose based on microsystems.

Recently, there had been great interest in switching from disordered porous gel media to patterned regular sieving structures, in the hope of achieving more efficient separation than gels in terms of separation speed and resolution. Colloidal templating of self-assembled bead arrays was recently applied to construct sieving gels comprising a periodic array of voids by selectively etching out of self-assembled silica beads (~100 nm in diameter) included during gelation [9]. The regularity of the void array made the direct experimental verification of the molecular sieving mechanism (*i.e.*, entropic trapping) possible via diffraction measurements. Another paper by Nykypanchuk and Hoagland reported a similar approach to template a two-dimensional gel with close-packed spherical beads, and direct observation of jump dynamics of long DNA between the cavities was achieved with fluorescence microscopy [10]. More recently, Zeng and Harrison used self-assembled silica beads arrays confined in microfluidic channels as the sieving matrix to separate both DNA and proteins with high resolution [11]. Sano *et al.* recently reported a size-exclusion chromatography device that used an anodic porous alumina as the separation matrix [12]. The porous alumina membrane traps smaller biomolecules more frequently, therefore they elute slower than the larger biomolecules in the channel. The porous alumina membrane has a uniform nanoscale pore distribution, and it does not require any nanolithography, therefore the fabrication of the membrane is relative easy and inexpensive. More recently, Tabuchi *et al.* reported a technology using a core-shell type nanosphere and nanoparticle medium in conjunction with a pressurization technique to carry out separation of a wide range of DNA fragments (100 base pairs (bp) to 20 kilo base pairs (kbp)) with high speed and high resolution on a microchip format [13]. In their device, optimal pressure conditions and concentrations of packed nanospheres were considered to be important for achieving improved DNA separation.

Various semiconductor microfabrication techniques have also been employed to fabricate regular microstructures or nanostructures as confining sieving media to separate biomolecules. So far, a wide range of regular sieving structure designs have been reported, both theoretically and experimentally. Examples include arrays of micrometeror nanometer-sized pillars that mimic gel fibers [14-18], channels with alternating deep and shallow regions that form entropic trap arrays [19-21], and asymmetric obstacle courses that act as Brownian (thermal) ratchets [22-25]. The regular arrays of micrometer- or nanometer-sized pillars have been fabricated by different groups with either contact lithography (with pillar diameter and spacing down to 1 μm) [14, 16] or e-beam lithography (with pillar diameter and spacing down to 100 nm) on silicon substrates [17, 18]. The advantages of such microlithographically fabricated devices include the precise control over the sieving matrix geometry and the design flexibility. Doyle *et al.* recently used another novel approach to construct columnar microstructures and applied a homogeneous magnetic field to a suspension of superparamagnetic particles contained in microchannels [15]. Their method provides additional sieving structure (or pore size) tunability after device construction, which is not possible with microlithography techniques. By applying two alternating electric fields of different directions and different magnitudes, Huang *et al.* recently devised a “DNA Prism” device that can continuously separate long DNA molecules with high speed [16]. In this design, the longer DNA molecules only follow the strong electric field component while the shorter ones migrate in the direction of the sum electric field vector.

Han and Craighead recently designed an entropy-based separation system where a microfluidic channel was defined with a sequence of deep and shallow channels [19, 20]. For long DNA molecules with diameters greater than the shallow region constriction size, passage requires the DNA molecule to deform and form hernias at the cost of internal conformational entropy. Longer DNA molecules have a larger surface area contacting the constriction and thus have a greater probability to form hernias that initiate the escape process, therefore longer DNA molecules advance faster than shorter DNA molecules. Another example of entropy-based separation system was demonstrated recently based on the concept of entropic recoil [26]. Long DNA molecules were driven into the pillared area by applied electric field. When the field was switched off, any DNA molecule resting entirely within the pillared area remained within, whereas those that had any region outside the pillared area relaxed back into the bulk liquid to maximize their conformational entropy. Since shorter DNA molecules have a greater probability to be driven entirely into the pillared area, they would not relax back and therefore their effective mobility in the device would be greater.

The concept of Brownian ratchets has been applied to construct asymmetric obstacle courses that provide a spatially asymmetric steric potential for biomolecule separation [22-25]. The basic idea is to use such asymmetric obstacles to rectify the Brownian motion laterally and thereby deflect diffusing biomolecules based on their sizes. So far, the Brownian ratchet systems have been successfully demonstrated for long DNA and phospholipids [24, 25], even though the separation resolution reported so far was not ideal. Previous theoretical studies had argued that simply downscaling the Brownian ratchet geometry to nanometer range would improve the biomolecule separation. However, more recent theoretical and experimental works have suggested that such approach still remains as an open question due to the critical nature of the biomolecule size with respect to the ratchet barrier gaps as well as the complexity of the effect of the ratchet boundary conditions on the separation [27, 28].

The regular molecular sieving structures discussed so far in this section have proven efficacious only for separation of long DNA and microspheres, and their applicability to smaller, physiologically-relevant macromolecules, such as proteins, remains questionable, which clearly limits progress on a future integrated bioanalysis system. In this thesis, we will explore the interesting possibility of constructing regular molecular sieving structures based on nanofluidic filters to separate physiologically-relevant biomolecules covering broad biological size scales, including both dsDNA and proteins.

1.3 Thesis outline and scopes

Separation of biomolecules by size is an important analytical and preparative technique in biology, medicine, chemistry, and various industries. Fractionation of biological molecules, such as nucleic acids and proteins, plays a central role in genomic and proteomic analysis. In the new challenge of systems biology, as well as in the applications of biomarker detection and biosensing, this task becomes even more important because of the lack of protein's equivalents of amplification, fractionation and sequencing techniques.

This thesis seeks to use microfabricated regular nanofluidic filters (nanofilters) as controllable sieving media for size-fractionation of various biologically-relevant macromolecules, including dsDNA, proteins, and polysaccharides, based on the Ogston sieving mechanism [29-31]. Using standard microfabrication techniques, we can precisely fabricate shallow nanofilters with gap thickness down to the vicinity of 10 nm. In such a confining nanofluidic channel, molecular transport properties are largely affected by the steric constraints that prevent a partial overlap of molecule with wall [32, 33]. In the proposed thesis, we will construct different microfabricated nanofilter based separation devices and explore the steric interaction of biomolecules in the nanofilter as a potential sieving mechanism for size-fractionation of biomolecules. In the proposed separation system, unlike other conventional random nanoporous sieving material based separation systems, the nanofilters (as a sieving matrix) can be made uniform and controllable, also chemical groups on the wall can be tailored. In addition to the application of biomolecule separation, the nanofilter based artificial sieving structures provide an ideal platform for the theoretical study of molecular dynamics and stochastic motion in confining spaces because of their precisely characterized environment [34, 35].

The specific aims of this proposed thesis include:

1) Design and fabricate one-dimensional nanofilter array based separation devices of various dimensions (with nanofilter gap thickness down to 20 nm to 40 nm and nanofilter pitch number down to 1 μm).
2) Study sieving process of biomolecules when passing through the nanofilter constriction. Demonstrate the feasibility of applying the Ogston sieving effect as a size-based separation mechanism to fractionate different biomolecules. Clarify the roles of nanofilter gap thickness and electric field in the nanofilter array operation. Demonstrate fast separation of biomolecules (such as proteins) with improved nanofilter structure design.
3) Design and fabricate a two-dimensional anisotropic nanofilter array based separation device for continuous-flow size-fractionation of various biomolecules. This device will be ideal for preparatory fractionation of biomolecules with increased sample throughput.

4) Based on understanding of the sieving process across the nanofilter constriction, we will develop a theoretical model for the continuous-flow separation of biomolecules in the two-dimensional periodic nanofilter array. Design guidelines for improving separation efficiency of biomolecules will be provided. Demonstrate fast continuous-flow fractionation of biomolecules (such as proteins) with the two-dimensional nanofilter array based separation devices.

1.4 References

1. Giddings, J. C. *Dynamics of Chromatography. Part 1. Principles and Theory* (Marcel Dekker, New York, 1965).
2. Scopes, R. K. *Protein Purification, Principles and Practice* (Springer-Verlag, New York, ed. 3, 1993).
3. Smejkal, G. B. & Lazarev, A. (eds.) *Separation Methods in Proteomics* (CRC Taylor & Francis, Boca Raton, FL, 2006).
4. Patrick Camilleri (ed.) *Capillary Electrophoresis: Theory and Practice* (CRC Press, Boca Raton, FL, 1998).
5. Wehr, T., Zhu, M. & Mao, D.T. in *Capillary Electrophoresis of Nucleic Acid*, vol. I (eds. Mitchelson, K.R. & Cheng, J.) 167–187 (Humana Press, Totowa, NJ, 2001).
6. Viovy, J.L. & Dukc, T. DNA electrophoresis in polymer solutions: ogston sieving, reptation and constraint release. *Electrophoresis* **14**, 322–329 (1993).
7. Yao, G., *et al.* SDS capillary gel electrophoresis of proteins in microfabricated channels. *Proc. Natl. Acad. Sci. U. S. A.* **96**, 5372—5377 (1999).
8. Callewaert, N., Contreras, R., Mitnik-Gankin, L., Carey, L., Matsudaira, P. & Ehrlich D. Total serum protein N-glycome profiling on a capillary electrophoresis-microfluidics platform. *Electrophoresis* **25**, 3128—3131 (2004).
9. Liu, L., Li, P. & Asher, S. A. Entropic trapping of macromolecules by mesoscopic periodic voids in a polymer hydrogel. *Nature* **397**, 141—144 (1999).
10. Nykypanchuk, D., Strey, H. H. & Hoagland, D. A. Brownian motion of DNA confined within a two-dimensional array. *Science* **297**, 987—990 (2002).
11. Zeng, Y. & Harrison D. J. Self-assembled colloidal arrays as three-dimensional nanofluidic sieves for separation of biomolecules on microchips. *Anal. Chem.* DOI: 10.1021/ac061931h.
12. Sano, T. *et al.* Size-exclusion chromatography using self-organized nanopores in anodic porous alumina. *Appl. Phys. Lett.* **83**, 4438—4440 (2003).
13. Tabuchi, M. *et al.* Nanospheres for DNA separation chips. *Nature Biotech.* **22**, 337—340 (2004).
14. Volkmuth, W. D. & Austin, R. H. DNA electrophoresis in microlithographic arrays. *Nature* **358**, 600—602 (1992).
15. Doyle, P. S., Bibette, J., Bancaud, A. & Viovy, J.-L. Self-assembled magnetic matrices for DNA separation chips. *Science* **295**, 2237 (2002)
16. Huang, L. R. *et al.* A DNA prism: high speed continuous fractionation of large DNA molecules. *Nature Biotech.* **20**, 1048—1051 (2002).
17. Baba, M. *et al.* DNA size separation using artificially nanostructured matrix. *Appl. Phys. Lett.* **83**, 1468—1470 (2003).
18. Kaji, N. *et al.* Separation of long DNA molecules by quartz nanopillar chips under a direct current electric field. *Anal. Chem.* **76**, 15—22 (2004).
19. Han, J., Turner, S. W. & Craighead, H. G. Entropic trapping and escape of long DNA molecules at submicron size constriction. *Phys. Rev. Lett.* **83**, 1688—1691 (1999).
20. Han, J., & Craighead, H. G. Separation of log DNA molecules in a microfabricated entropic trap array. *Science* **288**, 1026—1029 (2000).
21. Duong, T. T. *et al.* Size dependent free solution DNA electrophoresis in structured microfluidic systems. *Microelectronic Engineering* **67**, 905—910 (2003).

22. Ertas, D. Lateral separation of macromolecules and polyelectrolytes in microlithographic arrays. *Phys. Rev. Lett.* **80**, 1548─1551 (1998).
23. Duke, T. A. J. & Austin, R. H. Microfabricated sieve for the continuous sorting of macromolecules. *Phys. Rev. Lett.* **80**, 1552─1555 (1998).
24. Chou, F. *et al.* Sorting by diffusion: an asymmetric obstacle course for continuous molecular separation. *Proc. Natl. Acad. Sci. U.S.A.* **96**, 13762─13765 (1999).
25. van Oudenaarden, A. & Boxer, S. G. Brownian ratchets: molecular separation in lipid bilayers supported on patterned arrays. *Science* **285**, 1046─1048 (1999).
26. Turner S. W. P., Cabodi, M. & Craighead, H. G. Confinement-induced entropic recoil of single DNA molecules in a nanofluidic structure. *Phys. Rev. Lett.* **88**, 128103─128106 (2002).
27. Austin, R. H. *et al.* Ratchets: the problems with boundary conditions in insulating fluids. *Appl. Phys. A* **75**, 279─284 (2002).
28. Huang, L. R. *et al.* Role of molecular size in ratchet fractionation. *Phys. Rev. Lett.* **89**, art. no. 178301 (2002).
29. Viovy, J.-L. Electrophoresis of DNA and other polyelectrolytes: physical mechanisms. *Rev. Mod. Phys.* **72**, 813─872 (2000).
30. Ogston, A. G. The spaces in a uniform random suspension of fibres. *Trans. Faraday Soc.* **54**, 1754─1757 (1958).
31. Rodbard, D. & Chrambach, A. Unified theory for gel electrophoresis and gel filtration. *Proc. Natl. Acad. Sci. U. S. A.* **65**, 970─977 (1970).
32. Giddings, J. C., Kucera, E., Russell, C. P. & Myers, M. N. Statistical theory for the equilibrium distribution of rigid molecules in inert porous networks. Exclusion chromatography. *J. Phys. Chem.* **72**, 4397─4408 (1968).
33. Deen, W. M. Hindered transport of large molecules in liquid-filled pores. *AIChE J.* **33**, 1409─1425 (1987).
34. Bakajin, O. B. *et al*. Electrohydrodynamic stretching of DNA in confined environments. *Phys. Rev. Lett.* **80**, 2737─2740 (1998).
35. Tegenfeldt, J. O. *et al.* The dynamics of genomic-length DNA molecules in 100-nm channels. *Proc. Natl. Acad. Sci. U. S. A.* **101**, 10979─10983 (2004).

Chapter 2

Statics and dynamics of a polymer chain and equilibrium partitioning theory

Polymer systems have been studied extensively in physics, chemistry, biology and engineering sciences. Many biologically-relevant macromolecules can be considered as long linear polymer chains, for example, DNA, RNA, proteins, and polysaccharides. In this chapter, we first consider the statistical mechanics of polymer chains with no interactions between monomers that are far apart along the chain (the so-called "ideal chains"). Then we will discuss the dynamic properties of a single charged polymer chain (*i.e.*, a polyelectrolyte) in an ionic solution. We will then introduce different properties of electromigration of charged polymer chains in confining environments such as gels. At the end of the chapter, we will brief discuss the concept of the equilibrium partitioning theory. More complete and general treatments of statistical mechanics and dynamics of a polymer chain and the equilibrium partitioning theory can be found elsewhere (see Ref. [1-8]).

2.1 Static properties of an ideal linear polymer chain

The model of an ideal polymer chain plays the same role in polymer physics as the notion of an ideal gas in traditional molecular physics. This model represents a chain of immaterial links, each joined with two nearest neighbors (monomers) and having no interaction either with solvent molecules or with other links of the same chain that are far apart along the chain. There are several models for an ideal polymer chain, and each model makes different assumptions about the allowed values of torsion and bond angles between neighboring bonds. A common "ideal" feature of all these models for an ideal polymer chain is the absence of volumetric interactions between different monomers. The range of actual conditions for which the polymer chains behave as ideal ones is not very wide. Nevertheless, the ideal chain models are very helpful, because they allow one to form an idea about the character of thermal motion of polymer chains, or in other words, about the entropic properties of a polymer substance.

In this section, we will first consider the freely jointly chain model and introduce the concepts of the mean-square end-to-end distance $\left\langle R^2 \right\rangle$ and the Kuhn length. We will then consider the free rotating chain model and introduce the persistence length. Last we will consider the worm-like chain model and prove the relation between the Kuhn length and the persistence length. Finally, we will calculate the radius of gyration for an ideal polymer chain.

2.1.1 Freely jointed chain model

We will begin with the simplest model of an ideal polymer chain, a freely jointed chain. We consider a flexible polymer chain of n+1 backbone monomers A_i (with $0 \le i \le n$) as sketched in **Fig. 2.1**. The bond vector $\vec{r}_i$ goes from monomer A_{i-1} to monomer A_i. The polymer is in its ideal state if there is no interaction between monomer A_i and A_j that are separated by a sufficient number of bonds along the chain so that $|i-j| \gg 1$.

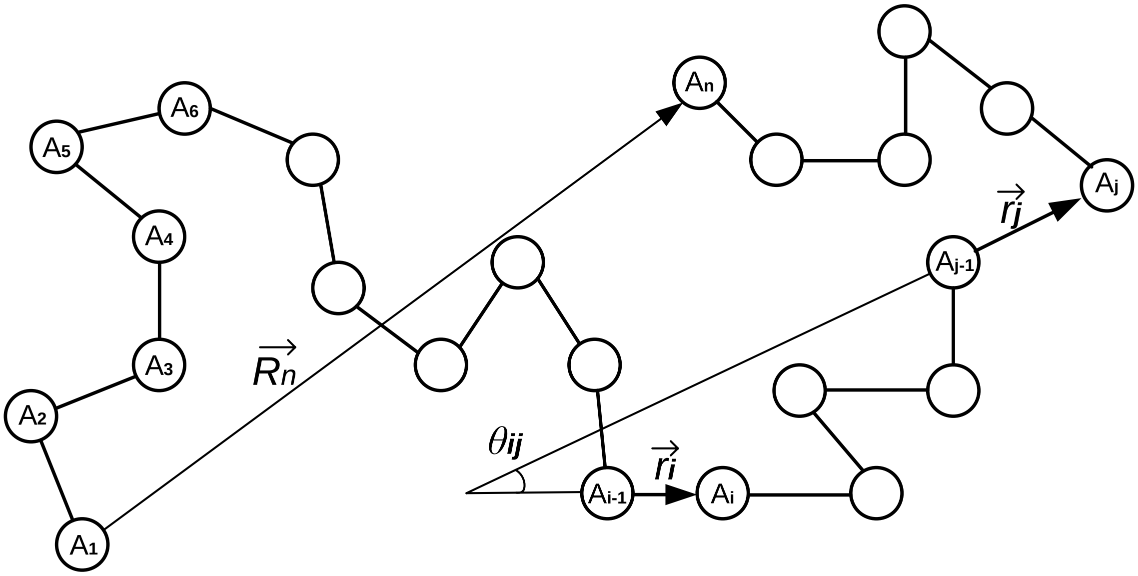

Figure 2.1: One conformation of a flexible polymer chain.

The end-to-end vector is the sum of all *n* bond vectors in the chain

$$\vec{R}_n = \sum_{i=1}^{n} \vec{r}_i \tag{2.1}$$

Different individual chains will have different bond vector conformations and hence different end-to-end vectors. The average end-to-end vector of an isotropic collection of chains of *n* backbone monomers is zero

$$\left\langle \vec{R}_n \right\rangle = 0 \tag{2.2}$$

The ensemble average $\langle \ \rangle$ denotes an average over all possible states of the system (accessed either by considering many chains or many different conformations of the same chain). The simplest non-zero average is the mean-square end-to-end distance $\left\langle R^2 \right\rangle$

$$\left\langle R^2 \right\rangle \equiv \left\langle R_n^2 \right\rangle = \left\langle R_n \cdot R_n \right\rangle = \left\langle \left(\sum_{i=1}^{n} \vec{r}_i \right) \cdot \left(\sum_{j=1}^{n} \vec{r}_j \right) \right\rangle = \sum_{i=1}^{n} \sum_{j=1}^{n} \left\langle \vec{r}_i \cdot \vec{r}_j \right\rangle \tag{2.3}$$

We assume all bond vectors have the same length $l_m = \left| \vec{r}_i \right|$, therefore, the scalar product can be represented in terms of the angle θ_{ij} between bond vector $\vec{r}_i$ and $\vec{r}_j$ as shown in **Fig. 2.1**

$$\vec{r}_i \cdot \vec{r}_j = l_m^2 \cos \theta_{ij} \tag{2.4}$$

The mean-square end-to-end distance $\left\langle R^2 \right\rangle$ becomes a double sum of average cosines as

$$\left\langle R^2 \right\rangle = \sum_{i=1}^{n} \sum_{j=1}^{n} \left\langle \vec{r}_i \cdot \vec{r}_j \right\rangle = l_m^2 \sum_{i=1}^{n} \sum_{j=1}^{n} \left\langle \cos \theta_{ij} \right\rangle \tag{2.5}$$

For a freely jointed chain, there is no correlation between the directions of different bond vectors, therefore $\left\langle \cos \theta_{ij} \right\rangle = 0$, for $i \neq j$. There are only *n* non-zero terms in the double sum ($\langle \cos\theta_{ij} \rangle = 1$ for *i*=*j*). The mean-square end-to-end distance $\langle R^2 \rangle$ of a freely jointly chain is therefore

$$\langle R^2 \rangle = nl_m^2 = l_c l_m \tag{2.6}$$

Where l_c is the contour length of the free jointly chain and $l_c=nl_m$. For the free jointly chain, l_c also equals the maximum end-to-end distance R_{max} of the polymer chain.

In a typical polymer chain, there are correlations between bond vectors (especially between neighboring ones) and $\langle \cos\theta_{ij} \rangle \neq 0$. But in an ideal chain, there is no interaction between monomers separated by a great distance along the chain contour. This implies that there are no correlations between the directions of distant bond vectors, and $\lim_{|i-j|\to\infty} \langle \cos\theta_{ij} \rangle = 0$. It can be shown that for a ideal chain, the sum of average cosines over all the bond vectors *i* and *j* will converge to a finite number, $\sum_{i=1}^{n}\sum_{j=1}^{n} \langle \cos\theta_{ij} \rangle \to nC_n$, where the coefficient C_n is called Flory's characteristic ratio (for an infinite chain, $C_n \rightarrow C_\infty$). Thus, for an ideal chain, the mean-square end-to-end distance $\langle R^2 \rangle$ can be expressed as

$$\langle R^2 \rangle = l_m^2 \sum_{i=1}^{n}\sum_{j=1}^{n} \langle \cos\theta_{ij} \rangle = C_n n l_m^2 \tag{2.7}$$

Therefore, the main property of ideal chains is that $\langle R^2 \rangle$ is proportional to the product of the number of bonds *n* and the square of the bond length l_m^2.

A simple unified description of all ideal polymers is provided by an equivalent free jointed chain. The equivalent chain has the same mean-square end-to-end distance

$\left\langle R^2 \right\rangle$ and the same maximum end-to-end distance R_{max} as the actual polymer chain, but has N freely-jointed effective bonds of length b. This effective bond length b is called the Kuhn length. The contour length of this equivalent freely jointed chain is

$$Nb = R_{\max} \tag{2.8}$$

And its mean-square end-to-end distance is

$$\left\langle R^2 \right\rangle = Nb^2 = bR_{\max} = C_\infty n l_m^2 \tag{2.9}$$

Therefore, the equivalent freely jointed chain has

$$N = \frac{R_{\max}^2}{C_\infty n l_m^2} \tag{2.10}$$

And the equivalent bonds (Kuhn monomers) of length

$$b = \frac{\left\langle R^2 \right\rangle}{R_{\max}} = \frac{C_\infty n l_m^2}{R_{\max}} \tag{2.11}$$

2.1.2 Freely rotating chain model

As the name suggested, the freely rotating chain model considers a polymer chain with fixed bond angle θ and ignores differences between the probabilities of different torsion angles and assumes all torsion angles to be equally possible. To calculate the mean-square end-to-end distance $\left\langle R^2 \right\rangle$ of a freely rotating chain, we need to determine the correlation between bond vectors $\vec{r}_i$ and $\vec{r}_j$. The correlations from bond vector $\vec{r}_j$ at bond vector $\vec{r}_i$ are characterized with a factor of $(\cos\theta)^{|i-j|}$ due to independent free rotations of $|j-i|$ torsion angles between these two vectors. This character of the freely rotating chain defines a persistence segment (the persistence length l_p) of the number of main-chain bonds, which is the scale at which local correlations between bond vectors decay

$$(\cos\theta)^{|i-j|} = \exp\left[|i-j|\cdot\ln(\cos\theta)\right] = \exp\left[-|i-j|l_m / l_p\right] \tag{2.12}$$

where the persistence length l_p is calculated as $l_p = -l_m / \ln\cos(\theta)$. The mean-square end-to-end distance $\langle R^2 \rangle$ of the freely rotating chain can be written as

$$\begin{aligned}
\langle R^2 \rangle &= \sum_{i=1}^{n}\sum_{j=1}^{n}\langle \vec{r}_i \cdot \vec{r}_j \rangle = \sum_{i=1}^{n}\left(\sum_{j=1}^{i-1}\langle \vec{r}_i \cdot \vec{r}_j \rangle + \langle \vec{r}_i^{\,2} \rangle + \sum_{j=i+1}^{n}\langle \vec{r}_i \cdot \vec{r}_j \rangle \right) \\
&= \sum_{i=1}^{n}\langle \vec{r}_i^{\,2} \rangle + l_m^2 \sum_{i=1}^{n}\left(\sum_{j=1}^{i-1}(\cos\theta)^{i-j} + \sum_{j=i+1}^{n}(\cos\theta)^{j-i} \right) \\
&= nl_m^2 + l_m^2 \sum_{i=1}^{n}\left(\sum_{k=1}^{i-1}\cos^k\theta + \sum_{k=1}^{n-i}\cos^k\theta \right)
\end{aligned} \tag{2.13}$$

Since the decay of the correlation between bonds is so rapid, the summation in the above equation can be replaced by an infinite series over k as

$$\begin{aligned}
\langle R^2 \rangle &= nl_m^2 + l_m^2 \sum_{i=1}^{n}\left(\sum_{k=1}^{i-1}\cos^k\theta + \sum_{k=1}^{n-i}\cos^k\theta \right) \\
&\approx nl_m^2 + 2nl_m^2 \sum_{k=1}^{\infty}\cos^k\theta \\
&\approx nl_m^2 + 2nl_m^2 \cos\theta/(1-\cos\theta)
\end{aligned} \tag{2.14}$$

Compared with Eq. (2.7), the Flory's characteristic ratio C_∞ for the freely-rotating chain can be calculated as

$$C_\infty = 1 + 2\cos\theta/(1-\cos\theta) = (1+\cos\theta)/(1-\cos\theta) \tag{2.15}$$

2.1.3 Worm-like chain model (Kratky-Porod model)

The worm-like chain model is a special case of the freely rotating chain model for a very small value of the bond angle θ ($\theta \ll 1$). The worm-like chain model is a suitable model for very stiff polymers, such as double-stranded DNA (dsDNA) for which the chain flexibility is due to thermal fluctuations of the chain contour from a straight line rather than to fluctuations of the bond and torsion angles between the monomers. For small bond angle θ ($\theta \ll 1$), cosθ and ln(cosθ) can be extended as

$$\cos\theta \approx 1-\theta^2/2 \tag{2.16}$$

$$\ln(\cos\theta) \approx -\theta^2/2 \tag{2.17}$$

respectively. Therefore, in the worm-like chain model, the persistence length l_p and the Kuhn length b are calculated as

$$l_p = -l_m/\ln\cos(\theta) = 2l_m/\theta^2 \tag{2.18}$$

$$b = \frac{C_\infty n l_m^2}{R_{\max}} = \frac{1+\cos\theta}{1-\cos\theta}\cdot n l_m^2 \cdot \frac{1}{n l_m \cos(\theta/2)} \approx \frac{4l_m}{\theta^2} \tag{2.19}$$

respectively. In Eq. (2.19), we implicitly use the expression of $R_{max}=nl_m\cos(\theta/2)$. From Eq. (2.18) and (2.19), it is clear that for a worm-like chain, the Kuhn length b is twice persistence length l_p ($b=2l_p$).

In the worm-like chain model, the factor of l_m/θ^2 enters in the expressions of the persistence length l_p and the Kuhn length b. The worm-like chain is defined as the limit of the monomer bond length $l_m \rightarrow 0$ and the bond angle $\theta \rightarrow 0$ at a constant persistence length l_p. These limits also result in the maximum end-to-end distance R_{max} of a worm-like chain equals its contour length ($R_{\max} = nl_m\cos(\theta/2) \approx nl_m$). In fact, the persistence length of a worm-like chain defines a length scale where the floppiness at the molecular scale as characterized by thermal fluctuations (entropy) is balanced by intrinsic elasticity (enthalpy) of the polymer chain. The polymer chain is dominated by its internal elasticity due to enthalpy effects when its contour length l_c is smaller than l_p ($l_c<l_p$), while it is dominated by entropic effects when l_c is larger than l_p ($l_c>l_p$).

The mean the mean-square end-to-end distance $\left\langle R^2 \right\rangle$ of the worm-like chain can be written as

$$\left\langle R^2 \right\rangle = l_m^2 \sum_{i=1}^{n}\sum_{j=1}^{n} \left\langle \cos\theta_{ij} \right\rangle = l_m^2 \sum_{i=1}^{n}\sum_{j=1}^{n} (\cos\theta)^{|j-i|} = l_m^2 \sum_{i=1}^{n}\sum_{j=1}^{n} \exp\left(-\frac{|j-i|}{l_p} l_m \right) \tag{2.20}$$

The summation over bonds can be changed into integration over the contour of the worm-like chain as $l_m \sum_{i=1}^{n} \to \int_0^{l_c} du$ and $l_m \sum_{j=1}^{n} \to \int_0^{l_c} dv$. Therefore, we have

$$\left\langle R^2 \right\rangle = \int_0^{l_c} \left[\int_0^{l_c} \exp\left(-\frac{|u-v|}{l_p} \right) dv \right] du$$

$$= 2l_p l_c - 2l_p^2 \left[1 - \exp(-\frac{l_c}{l_p}) \right] \tag{2.21}$$

Two simple limits exist for Eq. (2.21). The ideal chain limit is for worm-like chains much longer than their persistence length, and the rod-like limit is for worm-like chains much shorter than their persistence length. So we have

$$\left\langle R^2 \right\rangle \approx 2l_p l_c = bl_c \text{ (ideal chain limit)}$$

$$\left\langle R^2 \right\rangle \approx 2l_p l_c - 2l_p^2 \left(1 - (1 - \frac{l_c}{l_p} + \frac{1}{2}(\frac{l_c}{l_p})^2) \right) = l_c^2 \text{ (rod-like limit)} \tag{2.22}$$

The important difference between freely jointly chains and worm-like chains is that each bond of Kuhn length b of the freely jointed chain is assumed to be completely rigid. The worm-like chains are also stiff on length scales shorter than the Kuhn length, but are not completely rigid and can fluctuate and bend. These bending modes lead to a qualitatively different dependence of extensional force on elongation near maximum extension [4, 5].

In this thesis work, for simplicity, we neglect local fluctuation of chain contour of a short worm-like chain, and we will treat the short worm-like chain as a rigid rod-like molecule. We will apply Eq. (2.21) to calculate the end-to-end distance of the equivalent rigid rod-like molecule.

2.1.4 Radius of gyration of an ideal polymer chain

The size of an ideal linear polymer chain can be characterized by either its mean-square end-to-end distance $\left\langle R^2 \right\rangle$ or its square radius of gyration $\left\langle R_g^2 \right\rangle$. The square radius of gyration $\left\langle R_g^2 \right\rangle$ is defined as the average square distance between monomers in a given conformation (monomer vector $\vec{r}_i$) and the polymer chain's centre of mass ($\vec{r}_{cm}$) as

$$\left\langle R_g^2 \right\rangle = \frac{1}{N} \sum_{i=1}^{N} \left\langle (\vec{r}_i - \vec{r}_{cm})^2 \right\rangle \tag{2.23}$$

The centre of mass $\vec{r}_{cm}$ for a linear polymer whose monomers have the same molecular weights can be calculated as

$$\vec{r}_{cm} = \frac{1}{N} \sum_{j=1}^{N} \vec{r}_j \tag{2.24}$$

Therefore, the expression for the square radius of gyration $\left\langle R_g^2 \right\rangle$ takes the form

$$\left\langle R_g^2 \right\rangle = \frac{1}{N}\sum_{i=1}^{N}\left\langle (\vec{r}_i - \frac{1}{N}\sum_{j=1}^{N}\vec{r}_j)^2 \right\rangle \tag{2.25}$$

Through some manipulations of Eq. (2.25), $\left\langle R_g^2 \right\rangle$ can be calculated as [2, 4, 5]

$$\left\langle R_g^2 \right\rangle = \frac{1}{N^2}\sum_{i=1}^{N}\sum_{j=i}^{N}\left\langle (\vec{r}_i - \vec{r}_j)^2 \right\rangle \tag{2.26}$$

Again, we change the summations over the monomers into integrations over the contour of the chain, by replacing monomer indices *i* and *j* with continuous coordinates *u* and *v* along the contour of the chain as $\sum_{i=1}^{N} \rightarrow \int_0^N du$ and $\sum_{j=i}^{N} \rightarrow \int_u^N dv$. Therefore, we have

$$\left\langle R_g^2 \right\rangle = \frac{1}{N^2}\int_0^N \int_u^N \left\langle (\vec{r}(u) - \vec{r}(v))^2 \right\rangle dv du = \frac{b^2}{N^2}\int_0^N \int_u^N (v-u) dv du \tag{2.27}$$

$$\left\langle R_g^2 \right\rangle = \frac{Nb^2}{6} = \frac{\left\langle R^2 \right\rangle}{6} \tag{2.28}$$

Eq. (2.28) shows the classic Debye result relating the mean-square radius of gyration and the mean-square end-to-end distance of an ideal linear chain.

2.2 Dynamic properties of a linear polymer chain

In this section, we will consider the dynamic properties of a linear polymer chain such as diffusion coefficient (*D*) and relaxation time (τ) in two different models: Rouse chain model and Zimm model.

2.2.1 Rouse chain model

The first successful molecular model of polymer dynamics was developed by Rouse. The chain in the Rouse model is represented as N beads connected by springs of root-mean-square size b. The beads in the Rouse model only interact with each other through the connecting springs. Each bead is characterized by its own independent friction with a friction coefficient η. Solvent is assumed to be freely draining through the chain as it moves (the "free-draining" behavior), and no other long-range interaction between monomers is considered (**Fig. 2.2A**).

The total friction coefficient of the whole Rouse chain can be expressed as the sum of the contributions of each of the N beads

$$\zeta_R = N\eta \tag{2.29}$$

Therefore, the diffusion coefficient of the Rouse chain can be obtained from the Einstein relation as

$$D_R = \frac{k_B T}{\zeta_R} = \frac{k_B T}{N\eta} \tag{2.30}$$

The relaxation time (Rouse time) τ_R for a Rouse chain to diffuse a distance of the order of its size is calculated as

$$\tau_R \sim \frac{\langle R \rangle^2}{D_R} \sim \frac{Nb^2}{(k_B T / N\eta)} \sim \frac{N^2 b^2 \eta}{k_B T} \tag{2.31}$$

2.2.2 Zimm model

The viscous resistance imparted by the solvent when a monomer in the polymer chain moves through it arises from the fact that the monomer must drag some of the surrounding solvent with it due to the non-slippery boundary condition. The force acting on a solvent molecule at distance *r* from the monomer becomes smaller as *r* increases, but only slowly (decaying roughly as ~1/*r*). This long-range force acting on solvent and other monomers that arises from motion of one monomer is called hydrodynamic interaction. The Rouse chain model ignores hydrodynamic interaction forces, and assumes the monomers only interact through the springs (bonds) that connect them.

Assume that the polymer chain (and any section of the chain) drags with it the solvent in its pervaded volume. Thus the chain moves as a solid object of size *R* (*R* can be the radius of gyration of the polymer chain; this is the so-called “non-draining” behavior) (**Fig. 2.2B**). The friction coefficient of the chain ζ_Z being pulled through a solvent of viscosity η_s is given by Stokes law as

$$\zeta_Z \sim \eta_s R \sim \eta_s N^{1/2} b \tag{2.32}$$

From the Einstein relation, the diffusion coefficient of a chain in the Zimm model D_Z can be calculated as

$$D_Z \sim \frac{k_B T}{\zeta_Z} \sim \frac{k_B T}{\eta_s N^{1/2} b} \tag{2.33}$$

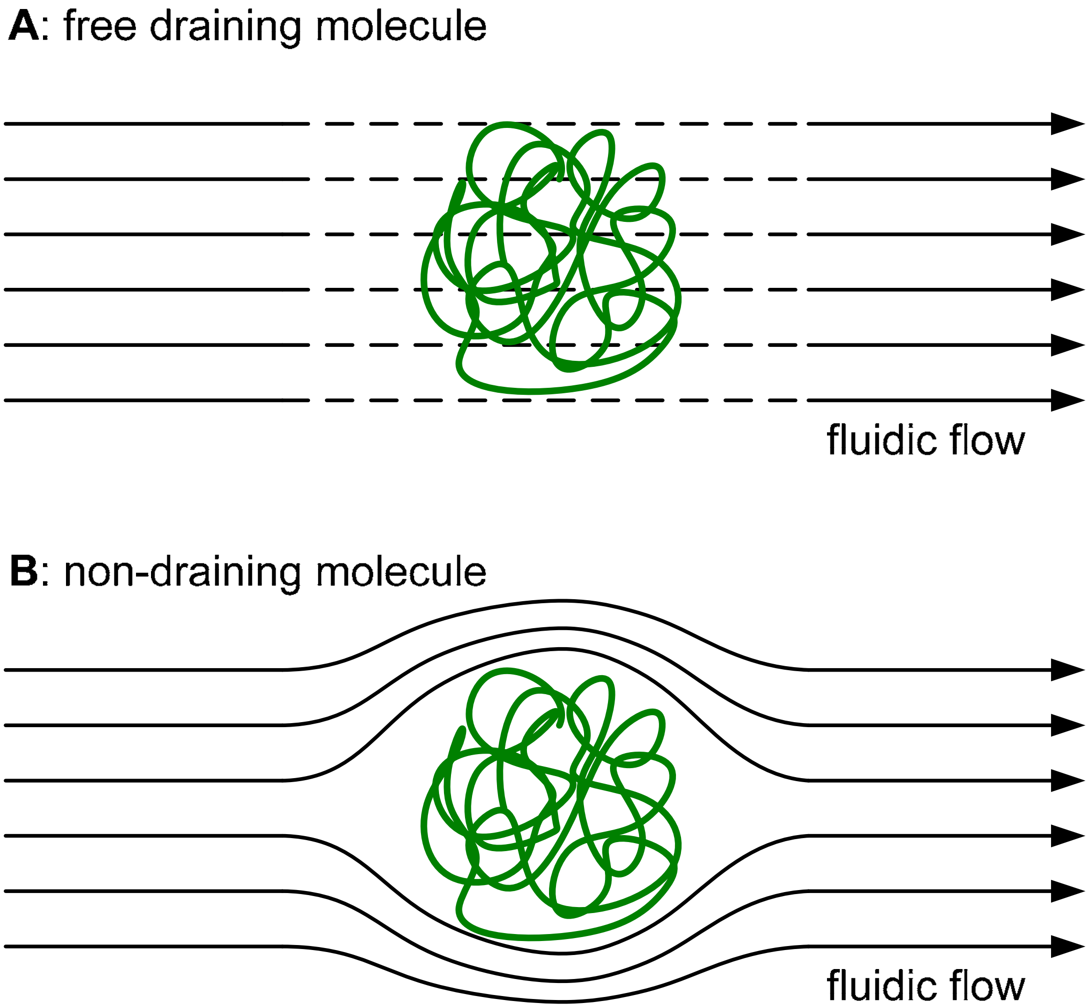

Figure 2.2: Free-draining *vs.* non-draining molecule. (**A**) In a free-draining polymer, fluidic flow can penetrate the polymer chain. There is no hydrodynamic interaction between different monomers. (**B**) In a non-draining polymer, the polymer chain drags with it the solvent in its pervaded volume. Thus the chain moves as a solid object of size *R*. Solvent molecules inside the polymer chain move together with the polymer. (adapted from Ref. [9])

2.3 Electrophoresis of polyelectrolytes and gel separation

We first consider a uniformly charged, linear polymer chain (*e.g.*, a polyelectrolyte) resting in a viscous ionic solution. This charged polymer chain perturbs the distribution of ions in the surrounding solution, with the equilibrium determined by the balance between electrostatic and Brownian forces (thermal fluctuations). The thickness of the equilibrium distribution of opposite-charged mobile ions surrounding the polymer chain can be calculated from the classic *Debye-Hückel* theory (this layer of counterions is called the *Debye* layer with its length of λ_D). The *Debye* length λ_D is the scale over which mobile ions screen out electric fields in the ionic solution. In other words, the *Debye* length is the distance over which significant charge separation can occur. The *Debye* screening length λ_D is given by [10]

$$k^{-1} = \left(\frac{\varepsilon k_B T}{e^2 N_A \sum_i z_i^2 \rho_i}\right)^{1/2} \tag{2.29}$$

where z_i and ρ_i are the number of charge and the number density of i-th ion, ε is the dielectric constant of the solution, N_A is the *Avogadro*'s constant. Under most typical buffer ionic strength, the *Debye* length λ_D is between a few nanometers to tens of nanometers.

We now consider the electrophoretic motion of a polyelectrolyte under an external electric field E applied uniformly across the solution. This electric field exerts an electrostatic force on the polymer chain. However, this field also acts on the surrounding counterion cloud (of thickness λ_D) and drags the surrounding solution in the opposite direction. The hydrodynamic interactions of the *Debye* layer with the migrating polymer chain are largely confined within the *Debye* layer. To simplify our arguments, we limit our discussions to the limit of a thin *Debye* layer as compared to the polymer chain size. The screening effect of this thin *Debye* layer therefore results in two important consequences. First, counterions screen the long-range coulomb potential between charged monomers separated by a distance longer than the *Debye* length. Second, the hydrodynamic interactions between the *Debye* layer and the polyelectrolyte backbone are largely confined within the *Debye* layer. As a result, there is no hydrodynamic or coulomb interaction between monomers of the polyelectrolyte during electrophoresis. In other words, the charged polymer chain is free-draining through solvent, and all the long-range interactions are screened out within the distance of λ_D. Therefore, the Rouse chain dynamics is valid and applicable, and the total friction constant ζ_{tot} of the polyelectrolyte becomes proportional to the chain length (ζ_{tot} ~N). If v is the velocity of the polyelectrolyte in the viscous solution and F_{tot} is the total electric force on the polyelectrolyte, the following equation

$$v = \frac{F_{tot}}{\varsigma_{tot}} = \mu E \tag{2.30}$$

defines the mobility μ. Since both F_{tot} and ζ_{tot} are linearly proportional to N, the mobility μ becomes independent of N. This observation is consistent with experimental observations that the electrophoretic mobility μ of nucleic acids (which is uniformly charged) is independent of their length in a free solution [11]. This length-independent mobility of uniformly charged polyelectrolytes makes it necessary to use the “sieving” properties of gels to separate nucleic acids based on size [12, 13].

Gel electrophoresis is currently the most widely used method in biology laboratory for the analysis of biological macromolecules, such as proteins and nucleic acids. Gel electrophoresis uses gelatinous materials consisting of cross-linked three-dimensional pore networks where the sieving interactions with the migrating biomolecules determine the separation efficiency [12, 13]. The method's wide-spread acceptance is solidly justified, as gel electrophoresis is characterized by unparalleled resolving power, the ability to analyze many samples simultaneously, the requirement for only a minute amount of sample, and many different possibilities for sample detection and recovery. In spite of the popular use of gel electrophoresis, the field of studying physical mechanisms of gel electrophoresis remains a subject of intense investigation [13]. The detailed theoretical study of sieving mechanisms in gel electrophoresis still has been limited by the lack of well-controlled experimental platforms for correlating the size and shape of the sieving pores to the observed molecular dynamic behavior.

Depending on the relative size of the macromolecule compared with the gel mean pore size (*e.g.*, the ratio of the radius of gyration R_g of the molecule to the gel mean pore size a), three basic separation mechanisms have been emerged to explain how flexible linear macromolecules migrate though a constraining gel medium ─ Ogston sieving ($R_g/a<1$), entropic trapping ($R_g/a\sim1$), and reptation ($R_g/a>1$) [12, 13] (**Fig. 2.3**). In Ogston sieving, the macromolecule is smaller than the gel pores or constrictions, and the molecular sieving occurs because of steric interactions of the macromolecules with the gel pore network [14-16]. Since $R_g/a<1$, the molecules move rather freely through the gel matrix, assuming their unperturbed conformations. Entropic trapping applies when $R_g/a\sim1$, and the conformation of the flexible macromolecule must deform or fluctuate to pass through the gel medium's spatial constrains [17-19]. At each point, the number of accessible conformations defines the molecule's local entropy. Entropy differences derived from the gel medium’s spatial heterogeneity drive molecules to partition or localize preferentially in less constrictive spaces, where their enhanced conformational freedom raises entropy. Reptation can be envisioned as a long linear flexible macromolecule occupying multiple pores threading its way through the gel in a snake-like fashion, which is very similar to the “reptation in a tube” process proposed by de Gennes for entangled synthetic polymers [20-23]. In the reptation mechanism, only the end segments of the linear polymer chain can escape as the molecule undergoes random curvilinear motion along the tube axis. Which diffusion mechanism prevails under given conditions in gels remains an open question. Sequential transitions from Ogston sieving to entropic trapping to reptation have been postulated as molecular weight or confinement increases. Such transitions, however, may not always be distinct.

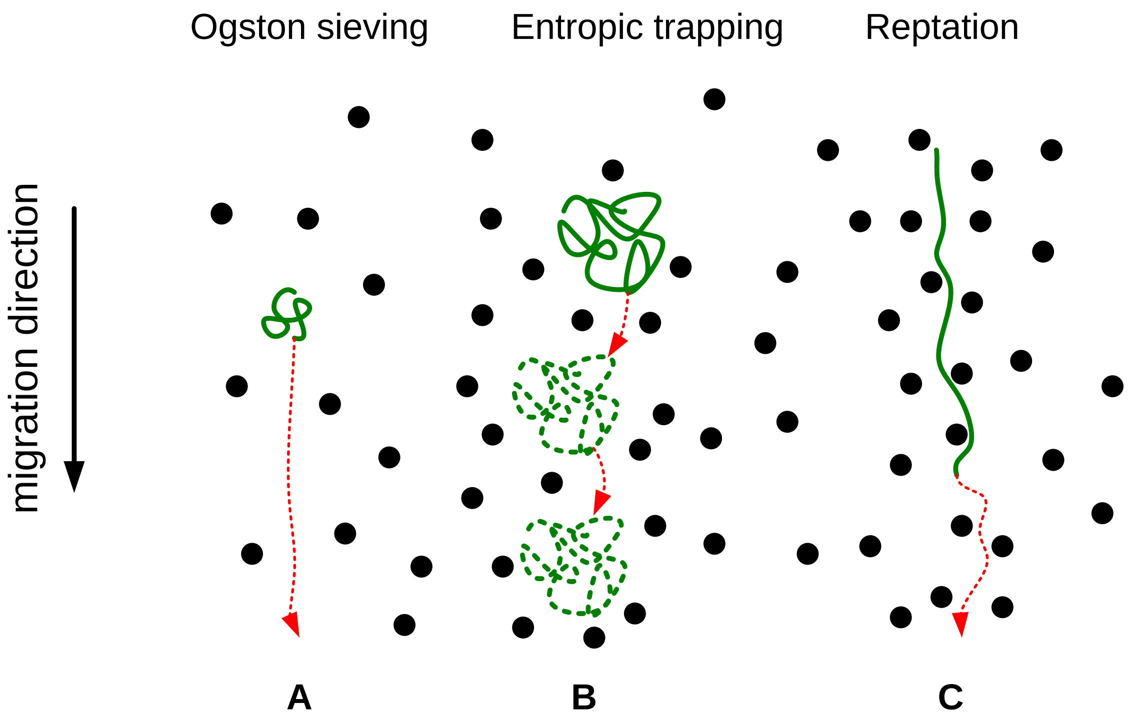

Figure 2.3. Electromigration of linear polyelectrolytes (*green*) in a gel network. *Red* dashed lines indicate migration trajectories. (**A**) Ogston sieving. In Ogston sieving, the polyelectrolyte is smaller than the gel pores or constrictions, and the molecular sieving occurs because of steric interactions of the macromolecules with the gel pore network. (**B**) Entropic trapping applies when the conformation of the flexible molecule must deform or fluctuate to pass through the gel medium's spatial constrains. In entropic trapping, the molecules jump preferentially between larger pores to enhance their conformational freedom entropy. (**C**) Reptation (with orientation). In reptation, the molecule is aligned in the direction of the electric field and reptates head first. (adapted from Ref. [12])

2.4 Gel electrophoresis: Ogston sieving, entropic trapping and reptation

Any theoretical treatment of the physical mechanisms of gel electrophoresis must answer two essential questions. First, what is the nature of spaces which the biomolecules occupy during their migration, and second, how do the molecules pass through these gel pore spaces. To answer the first question, we must first consider the structure of gels. A gel is a colloidal system in which a porous network of interconnected nanopores spans the volume of a liquid medium. In general, gels are solid, jelly-like materials. Both by weight and volume, gels are mostly liquid in composition and thus exhibit densities similar to liquids; however gels have the structural coherence of a solid. The most important parameter to characterize a gel is the average gel pore size. However, due to gels' intrinsic nature of random distributed network, it is probably not reasonable to define a very accurate and definite measurement of a gel pore size, but agreement can be obtained on orders of magnitude, typically 200 nm to 500 nm for agarose gels, and 5 nm to 100 nm for acrylamide gels [13]. In the following sections, we will discuss in details the three sieving mechanisms in gel electrophoresis: Ogston sieving, entropic trapping and reptation.

2.4.1 Ogston sieving and the extended Ogston model

In Ogston sieving, the linear macromolecules can be treated as a rigid sphere, assigning a fixed radius equal to the molecule's average size. In the Ogston sieving mechanism, macromolecule is smaller than the gel pores or constrictions, and the molecular sieving occurs because of steric interactions of the macromolecules with the gel pore network. In Ogston sieving, the molecules can move freely through the gel matrix, assuming their unperturbed conformations. According to the extended Ogston model of gel electrophoresis (also known as the free-volume model) [13-16], the gel is assumed to act as a sieve with a distribution of pore sizes, and the separation is viewed as a process of electric-field-driven partitioning process. The extended Ogston model is established based on the assumption that the ratio of the electrophoretic mobility in the gel μ relative to the mobility in a free solution μ_0 is equal to the fractional volume (or pore space) available to the molecule in the gel. This fractional volume or pore space in turn depends on the probability of no contact of the biomolecule with the gel fibers. The probability is related to the size of the molecule, the thickness of gel fibers, and concentration of the gel. According to the extended Ogston model, the logarithmic of mobility μ of a migrating molecule with a radius of R is [13, 15]

$$\log \mu = \log \mu_0 - \pi l^{'}(r+R)^2 C$$

or $$\log \mu = \log \mu_0 - K_r C \tag{2.31}$$

where $l^{'}$ is the gel fiber length per unit volume, r is the gel fiber radius, C is the total gel concentration, and K_r is the retardation coefficient ($K_r = \pi l^{'}(r+R)^2$). Equation (2.31) has been widely verified in starch, polyacrylamide, and agarose gels for separating small and relative globular objects, such as proteins in their native states [13, 16].

2.4.2 Entropic trapping

Originally the concept of entropic trapping was introduced to understand the motion of long DNA polymers in porous environments such as gels. Smisek and Hoagland, based on the agarose gel electrophoresis experiments, recognized the "entropic-barrier mediated transport" as an intermediate regime between the Ogston sieving regime and the reptation regime [18]. It had also been experimentally demonstrated by Rousseau *et al.* that there exists an entropic trapping transport regime in the polyacrylamide gel electrophoresis [19]. The entropic trapping occurs because molecules spend most of their time in the larger pores and must therefore fight strong entropic forces to cross the narrow passages jointing these large and rare voids (**Fig. 2.2 B**). Entropic barriers transport applies when the conformation of a flexible macromolecule must deform or fluctuate to pass through the gel medium's spatial constraints. At each position, the number of accessible conformations defines the molecule's local entropy. Entropy differences derived from the medium's spatial heterogeneity drive molecules to partition or localize preferentially in less constrictive spaces, where their enhanced conformational freedom raises entropy. Molecular transport then occurs by thermally activated jumps across the intervening entropic barriers. Again, entropic trapping can be regarded as an electric-field-driven partitioning process, but it involves deformation and conformational entropy penalty.

Direct experimental observations of entropic trapping (or entropic-barrier mediated transport) have been recently achieved in artificial molecular sieving systems with precisely controlled geometries [24-26]. Han *et al.* had recently designed an entropy-based separation system where a microfluidic channel was defined with a sequence of deep and shallow channels. Han *et al.* had applied this entropy trap array device to observe the *in situ* jump dynamics of long DNA (DNA deformation and hernias formation) across the nanofilter constriction with fluorescence microscopy [24]. Colloidal templating of self-assembled bead arrays was recently applied to construct sieving gels comprising a periodic array of voids [25]. The regularity of the void array made the direct experimental verification of entropic trapping possible via diffraction measurements [25]. A more recent paper by Nykypanchuk and Hoagland reported a similar approach to template a two-dimensional gel with close-packed spherical beads, and direct observation of jump dynamics of long DNA between the cavities was achieved with fluorescence microscopy [26].

2.4.3 Reptation

The early studies on gel electrophoresis of nucleic acids, including the observations from different groups that the mobilities of DNA fragments are proportional to the reciprocal of their length, led to the development of the reptation model (reptation = snake-like movement) of DNA gel electrophoresis. The reptation model had also been applied to gel electrophoresis of SDS-protein complexes [13]. Reptation can be envisioned as imposing lateral confinement on a diffusing linear macromolecule by enveloping the molecule in a fictitious tube (**Fig. 2.3C**). Only end segments can escape as the molecule undergoes random curvilinear motion along the tube axis. The tube's random contour and the molecule's sliding friction combine to hinder center-of-mass displacement. In contrast to entropic barriers transport, the number of configurations accessible to a reptating macromolecule does not depend on position. The reptation model initially relied on de Gennes' theory of the motion of polymeric molecules in the presence of fixed obstacles

[20]. The interpretation of electrophoresis data was based on the de Gennes' theory which was not originally developed for gel electrophoresis, as was the case earlier with the extended Ogston model. According to the reptation model, molecules orient themselves in the direction of the electric field, and their mobility can be described as [13]

$$\mu = \frac{Nq}{3\xi}(\frac{1}{N} + \frac{E'^2}{3}) \tag{2.32}$$

where q is the effective net charge per DNA base pair, ζ is the frictional coefficient for translational motion along the tube, N is DNA base pair number, and E' is a dimensionless reduced electric field (more discussions can be found in Ref. [13]). Equation (2.32) indicates that mobilities of long DNA molecules, and of shorter DNA molecules at high electric field strengths, will approach a constant value, leading to a loss of resolution. This was indeed observed for long DNA molecules in agarose gels [16].

2.5 Equilibrium partitioning theory

In this section, we will discuss the equilibrium partitioning theory. The partitioning of rigid and flexible molecules between bulk solution and porous solids is an important aspect of hindered diffusion and related topics, such as ultrafiltration, gel exclusion chromatography, and osmotic flow in membranes [6-8]. In fact, the extended Ogston model for gel electrophoresis discussed in the previous section shares a similar foundation established for calculation of partition coefficients for rigid spherical solutes in a random network of rods (by Ogston, more discussion see Ref. [27]).

In this section, we only consider the partitioning of rigid molecules. For flexible molecules, the reader can refer to two other references [28, 29]. The partition coefficient,

K, is the equilibrium ratio of solute concentration within the interstitial space of a porous material to that in the bulk solution. We restrict our attention to the limit of dilute solution; therefore, the effects of solute-solute interaction are negligible. We also only consider the case of a dilute solution in a neutral pore, therefore, no attractive or repulsive force other than the purely steric interactions exists between the molecule and pore wall. Other molecule-molecule and molecule-pore interactions may include long-range attractive or repulsive forces, for example, electrical double-layer effects, adsorptive forces, as well as appreciable solvent molecule size [8, 30, 31]. However, including such long-range interactions often results in the analytical solution of the partition coefficient K impossible.

Giddings *et al.* had established a general foundation for partitioning from the principles of statistical thermodynamics: the partition coefficient revolves around excluded volume in general configurational space, and it is a statistical or configurational entropy phenomenon [7]. The partition coefficient K can be expressed as the ratio of the configurational state integrals for molecules within the pores and within the bulk solution as

$$K = \frac{\int_{\underline{x}}\int_{\underline{\phi}} p(\underline{x},\underline{\phi})\, d^3\underline{x}\, d^3\underline{\phi}}{\int_{\underline{x}}\int_{\underline{\phi}} d^3\underline{x}\, d^3\underline{\phi}} \tag{2.33}$$

Integration is over the set of all molecule center positions $\underline{x}$ lying within the pore space and all molecule orientations $\underline{\phi}$. In Eq. (2.33), $p(\underline{x},\underline{\phi})$ represents the probability density of the molecule having a given configuration $(\underline{x},\underline{\phi})$. For the purely steric case we are interested in this thesis, $p(\underline{x},\underline{\phi})$ is unity for all configurations in which the molecule does not touch the pore wall and zero for disallowed configurations (**Fig. 2.4**) (here we have implicitly assumed that all "accessible" conformations are energetically equal or that only a single conformation exists (*e.g.*, rigid molecule)). This simplification reduces the calculation of K in Eq. (2.33) to a geometric problem, where K is the ratio of the orientation-averaged pore volume available to the molecule center to total pore volume. Inclusion of other long-range interactions may be accomplished by defining and inserting the appropriate Boltzmann factor, $\exp(-\varepsilon_{mp}/k_BT)$, for $p(\underline{x},\underline{\phi})$ into the numerator of Eq. (2.33). Here ε_{mp} is the energy term stemming from the interaction of molecule with the pore wall and other molecules, and k_BT is the thermal energy.

Using the above-mentioned geometric arguments, Giddings *et al.* studied partitioning of axissymmetric molecules in inert rectilinear pores [7]. For the case of rigid, rod-like molecules (with an end-to-end length of L) partitioning in a rectangular pore (with width of d_1 and height of d_0, see **Fig. 2.5**), Giddings *et al.* developed an analytical expression for the partition coefficient K as

$$K(\beta,\rho)=1-\frac{1+\rho}{2\rho}\beta+\frac{2\beta^2}{3\pi\rho} \qquad (\beta\le 1) \qquad (2.34a)$$

$$\begin{aligned}K(\beta,\rho)=&\frac{1}{2\beta}-\frac{\beta}{2\rho}+\frac{2\beta^2}{3\pi\rho}+\frac{\beta}{\pi\rho}\arccos\frac{1}{\beta}\\&-\frac{1}{3\pi\rho}(\beta^2-1)^{1/2}[2\beta+(1/\beta)]\end{aligned} \qquad (1\le\beta\le\rho) \qquad (2.34b)$$

where β is the scaled molecular length and $\beta=L/d_0$, ρ is the scaled pore width and $\rho=d_1/d_0$.

Here it is worthy to mention that all the discussion above permits only monoenergetic configurations, therefore, enthalpy effects (or conformational entropy) are absent. In this case, the standard (Gibbs) free energy change is simply $\Delta F^0 = -T\Delta S^0$. The entropy term ΔS^0 is equal to $\Delta S^0 = k_B \ln(\Omega / \Omega_0)$, where Ω / Ω_0 is the ratio of accessible microscopic configurations or states within the free pore volume compared with those in an equal volume of bulk liquid. The ratio of Ω / Ω_0 is clearly the ratio of configurational integrals and is equal to the partition coefficient *K*. Therefore, we can conclude that the dominant effect in this kind of equilibrium relates to changes in configurational entropy.

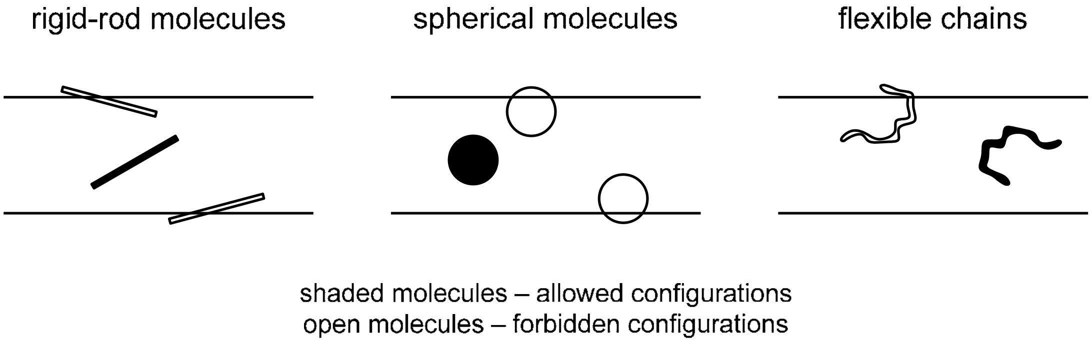

Figure 2.4: Illustration of allowed and forbidden molecular configurations confined in two parallel planes. Certain molecular configurations are forbidden due to the steric repulsion from the pore wall to prevent a partial overlap. In this case, exclusion is essentially a surface effect. (adapted from Ref. [7])

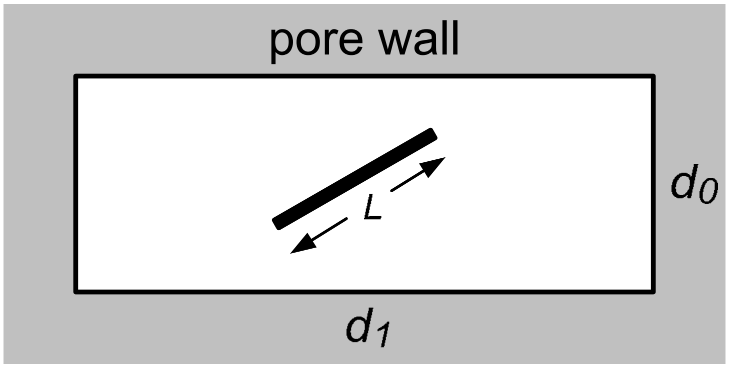

Figure 2.5: Illustration of a rid, rod-like molecule confined in a rectangular pore (with width of d_1 and height of d_0).

2.6 References

1. DeGennes, P. G. *Scaling Concepts in Polymer Physics* (Cornell University Press, Ithaca, NY, 1979).
2. Doi, M. & Edwards, S. F. *The Theory of Polymer Dynamics* (Oxford University Press, Oxford, UK, 1986).
3. Flory, P. J. *Statistical Mechanics of Chain Molecules* (Hanser Publishers, New York, 1989).
4. Grosberg, A. Y. & Khokhlov, A. R. *Statistical Physics of Macromolecules* (AIP Press, New York, 1994).
5. Rubenstein, M. & Colby, R. H. *Polymer Physics* (Oxford, New York, 2003).
6. Giddings, J. C. *Dynamics of Chromatography. Part 1. Principles and Theory* (Marcel Dekker, New York, 1965).
7. Giddings, J. C., Kucera, E., Russell, C. P. & Myers, M. N. Statistical theory for the equilibrium distribution of rigid molecules in inert porous networks. Exclusion chromatography. *J. Phys. Chem.* **72**, 4397─4408 (1968).
8. Deen, W. M. Hindered transport of large molecules in liquid-filled pores. *AIChE J.* **33**, 1409─1425 (1987).
9. Han. J. Entropic trap array device for DNA separation. Ph.D. thesis, Cornell University, 2001.
10. Probstein, R. F. *Physicochemical Hydrodynamics. An Introduction* (John Wiley & Sons, New York, 1994).
11. Stellwagen, N. C., Gelfi, C. & Righetti, P. G. The free solution mobility of DNA. Biopolymers, **42**, 687─703 (1997).
12. Slater, G. W., Mayer, P. & Drouin, G. Migration of DNA through gels. *Methods Enzymol.* **270**, 272─295 (1996).
13. Viovy, J.-L. Electrophoresis of DNA and other polyelectrolytes: physical mechanisms. *Rev. Mod. Phys.* **72**, 813─872 (2000).
14. Ogston, A. G. The spaces in a uniform random suspension of fibres. *Trans. Faraday Soc.* **54**, 1754─1757 (1958).
15. Rodbard, D. & Chrambach, A. Unified theory for gel electrophoresis and gel filtration. *Proc. Natl. Acad. Sci. U. S. A.* **65**, 970─977 (1970).
16. Tietz, D. Evaluation of mobility data obtained from gel electrophoresis: strategies in the computation of particle and gel properties on the basis of the extended Ogston model. *Advances in Electrophoresis* (VCH Publishers, New York, 1988), Vol. 2, 109─169.
17. Muthukumar, M. & Baumgärtner, A. Effects of entropic barriers on polymer dynamics. *Macromolecules* **22**, 1937─1941 (1989).
18. Smisek, D. L. & Hoagland, D. A. Electrophoresis of flexible macromolecules: evidence for a new mode of transport in gels. *Science* **248**, 1221─1223 (1990).
19. Rousseau, J., Drouin, G. & Slater, G. W. Entropic trapping of DNA during gel electrophoresis: effect of field intensity and gel concentration. *Phys. Rev. Lett.* **79**, 1945─1948 (1997).
20. de Gennes, P. G. Reptation of a polymer chain in the presence of fixed obstacles. *J. Chem. Phys.* **55**, 572─579 (1971).

21. Doi, M. & Edwards S. F. Dynamics of concentrated polymer systems. Part 1. ─Brownian motion in the equilibrium state. *J. Chem. Soc. Faraday Trans. II* **74**, 1789─1801 (1978).
22. Lumpkin, O. J., Dejardin, P. & Zimm, B. H. Theory of gel electrophoresis of DNA. *Biopolymers* **24**, 1573─1593 (1985).
23. Slater, G. W. & Noolandi, J. On the reptation theory of gel electrophoresis. *Biopolymers* **25**, 431─454 (1986).
24. Han, J., Turner, S. W. & Craighead, H. G. Entropic trapping and escape of long DNA molecules at submicron size constriction. *Phys. Rev. Lett.* **83**, 1688─1691 (1999).
25. Liu, L., Li, P. & Asher, S. A. Entropic trapping of macromolecules by mesoscopic periodic voids in a polymer hydrogel. *Nature* **397**, 141─144 (1999).
26. Nykypanchuk, D., Strey, H. H. & Hoagland, D. A. Brownian motion of DNA confined within a two-dimensional array. *Science* **297**, 987─990 (2002).
27. Kozulic, B. Models of gel electrophoresis. *Anal. Biochem.* **231**, 1─12 (1995).
28. Casassa, E. F. Equilibrium distribution of flexible polymer chains between a microscopic solution phase and small voids. *J. Polym. Sci. Polym. Lett.* **5**, :773─778 (1967).
29. White, J. A. & Deen, W. M. Equilibrium partitioning of flexible macromolecules in fibrous membranes and gels. *Macromolecules* **33**, 8504─8511 (2000).
30. Smith, F. G. & Deen, W. M. Electrostatic effects on the partitioning of spherical colloids between dilute bulk solution and cylindrical pores. *J. Colloid Interface Sci.* **91**, 571─590 (1983).
31. White, J. A. & Deen, W. M. Effects of solute concentration on equilibrium partitioning of flexible macromolecules in fibrous membranes and gels. *Macromolecules* **34**, 8278─8285 (2001).

Chapter 3

Ogston sieving of DNA and proteins through patterned nanofilter arrays

In this chapter, we present the design and fabrication of nanofluidic filter (nanofilter) arrays, and further demonstrate size-based separation of short DNA molecules and proteins based on the Ogston sieving mechanism. Nanofilter arrays with a gap size of 40 nm to 180 nm were successfully fabricated and characterized. Complete separation of short DNA molecules and proteins were achieved within a few minutes with a separation length of 5 mm. The fabrication strategy for the nanofilter array device allows further increasing of the nanofilter density and decreasing of the nanofilter gap size, leading, in principle, to even faster separation. In this chapter, we will first discuss Ogston sieving as the separation mechanism for biomolecules crossing a nanofilter constriction. Then we will proceed with more details of the design and fabrication of the nanofilter array devices that will be used for separation experiments with short DNA molecules and proteins.

3.1 Ogston sieving of biomolecules across a nanofilter

The main goal of this thesis work is to design efficient nanofluidic structures to achieve rapid separation of physiologically-relevant biomolecules such as double-stranded DNA molecules (dsDNA), proteins, and carbohydrates. To achieve this goal, we need to understand different transport properties of biomolecules in confining nanofluidic structures and further identify proper separation mechanisms and sieving structure designs to provide novel basis for efficient size-based separation of these physiologically-relevant biomolecules. In **Chapter 2**, we have discussed different sieving modes of biomolecules when migrating through confining sieving media. Of particular interest, the Ogston sieving mechanism is relevant to separation of biomolecules whose sizes are smaller than the pore and constriction size [1-6]. Since we are interested in separation of biomolecules of rather small sizes (for example, most globular proteins have radii of gyration about 1 nm to 10 nm), we will apply the Ogston sieving mechanism and further design efficient molecular sieving structures to achieve rapid separation of biomolecules based on the Ogston sieving mechanism.

In this project, we propose using the nanofluidic filter (nanofilter) array device to separate biologically-relevant molecules such as dsDNA and proteins based on the Ogston sieving mechanism. The design of the nanofilter array device is similar to the entropic trap array Han *et al.* devised to separate long linear dsDNA molecules (10-200 kbp) [7]. However, the nanofilter array device utilizes a different sieving mechanism (the Ogston sieving mechanism). In contrast to the entropic trapping method of separation, Ogston sieving involves molecular transport through nanofilter constrictions whose diameters are greater than the molecular size; therefore, the sieving does not necessarily involve molecules deforming and internal conformational entropy penalty (an enthalpy effect) as in the case of entropic trapping [7, 8]. **Figure 3.1** illustrates the nanofilter array device geometry. Essentially, an electric field drives negatively charged molecules (*e.g.*, dsDNA molecules under normal physiological conditions) through a microfluidic channel with alternating deep and shallow regions. Biomolecules experience sieving effects caused by steric constraints whenever they jump across a nanofilter shallow region. The configurational freedom of the molecules inside the nanofilter shallow region is limited due to steric repulsion from the wall [9, 10], and this creates a size-dependent configurational entropic energy barrier for the molecule passage from the nanofilter deep region to the confined space of the shallow region. Smaller-sized biomolecules are favored to jump across the nanofilter constrictions due to their greater retained configurational freedom. Therefore, smaller-sized biomolecules jump across the nanofilter constriction with higher probability, leading to faster migration speed or higher mobility through the whole nanofilter array.

The configurational entropic energy barrier is responsible for the differential penetration of biomolecules into porous materials, for applications like ultrafiltration and differential dialysis, along with the gel exclusion chromatography [9-11]. Presumably this configurational entropy effect is also responsible for the sieving process of small and relative globular molecules in gel electrophoresis [4, 6]. In this chapter, we will examine the interesting possibility of separating dsDNA and proteins with nanofilters larger than the molecular dimensions.

For the Ogston sieving regime in gel electrophoresis, optimal separation is expected when the size of the biomolecules is comparable with the average gel pore and constriction size [6]. Therefore, to achieve efficient Ogston sieving of biomolecules through the nanofilter array, we need to design the model pore-constriction system with the constriction size comparable to the molecules to be analyzed. To this end, the nanofilter shallow region depth should be in the range of 10 nm to 100 nm, and the nanofilter deep region depth should be in the range of 100 nm to 500 nm. Remember that the average pore size in agarose gel is typically about 200 nm to 500 nm, and in acrylamide gel about 5 nm to 100 nm [6].

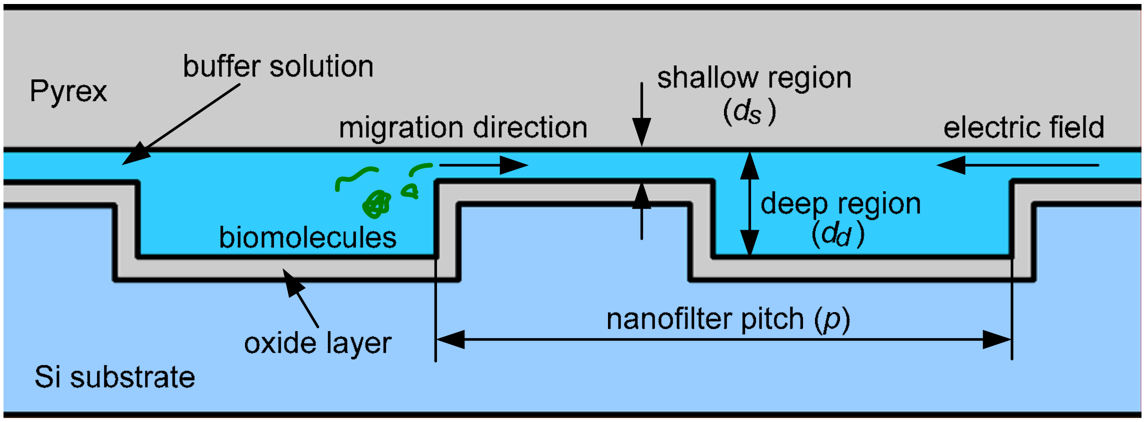

Figure 3.1: Schematic of the one-dimensional nanofilter array device with alerting deep and shallow regions. The nanofilter array has shallow regions with gap thickness of d_s, and deep regions with gap thickness of d_d, and a nanofilter pitch number of p. When biomolecules (*green*) jump across the nanofilter constriction from the deep region to the shallow region, the steric constrains within the shallow region limit the biomolecule configurational freedom. Therefore, there will be a size-dependent configurational entropic free energy barrier for the passage of biomolecules through the nanofilter constriction. This size-dependent free energy barrier will cause smaller biomolecules to jump across the constriction with higher probability. Therefore, smaller molecules will migrate through the whole nanofilter array with higher mobility.

3.2 Nanofilter array: device design and fabrication

To realize Ogston sieving of biomolecules in a nanofluidic device and possibly use the device to separate biomolecules based on size, we designed a restrictive channel with many "nanopores" and shallow gaps, and used a fluorescence detection method to observe the migration of fluorescent-labeled biomolecules through the channel. The microfluidic channel has alternating regions with deep (nanofilter deep region, 100 nm to 500 nm) and shallow (nanofilter shallow region, 10 nm to 100 nm) gap thickness (**Fig. 3.1**). Compared with the high-configurational-entropy deep region, the limited biomolecule configurational space inside the nanofilter shallow region creates a configurational entropic energy barrier for biomolecule passage at the abrupt interface between the nanofilter deep and shallow regions [9, 10]. This configurational entropic barrier originates from the steric constraints that prevent a partial overlap of the biomolecules with the nanofilter wall, and is different from the conformational entropic barrier associated with molecular deformation and entropic elasticity [7, 8]. Using a similar nanofluidic device, Han *et al.* had observed *in situ* long DNA (λ DNA, 48.5 kbp, radius of gyration R_g about 730 nm) deforming and stretching at the entrance of the nanofluidic constriction with a thickness of 90 nm [7]. However, since the biomolecules (*e.g.*, proteins) we are interested in this project has much smaller dimensions, it is difficult to observe single biomolecule jump dynamics across the nanofilter constriction. Nevertheless, we can use the fluorescence microscopy to observe ensembles of biomolecules of different sizes migrating through the nanofilter array with different mobilities.

The nanofilter array device can be fabricated in the clean room environment using conventional semiconductor microfabrication techniques. **Figure 3.2** shows a schematic of the three-mask fabrication process. First, shallow and deep regions of the nanofilter array were defined and etched into a 6-inch silicon wafer using conventional photolithography and reactive-ion etching (RIE) techniques. For nanofilter arrays with different pitch numbers, we have used different photolithography tools: contact lithography (EV620, Electronic Visions Group, AZ) for a nanofilter pitch number greater than 4 μm, and step-and-repeat projection lithography (Nikon NSR2005i9, Nikon Precision Inc., CA) for a nanofilter pitch number less than 2 μm. Using chlorine (Cl_2) and hydrogen bromide (HBr) etching chemistry, the etch rate of the silicon substrate during the RIE step (AME P5000, Applied Materials Inc., CA) can be well-controlled to be about 2.7 nm/sec. Therefore we can control the etch time of the RIE process to determine the nanofilter shallow and deep region depths. Then potassium hydroxide (KOH) etching was performed at 80°C to etch through the whole Si wafer to create buffer access holes. As a protection layer for the KOH etching, we had beforehand deposited a low-stress silicon nitride (Si_3N_4) layer on both sides of the Si wafer using the low-pressure chemical vapor deposition method (LPCVD). A thick thermal oxide layer (200 nm to 500 nm) was then grown on the silicon wafer using LPCVD furnaces to provide an electrical isolation between the conductive Si substrate and buffer solution. Finally, nanofilter array devices were sealed by anodically bonding a Pyrex wafer on the front surface of the silicon wafer. The bonded wafers were cut by diesaw into individual nanofilter array devices for channel filling and separation experiments. The depths of shallow and deep regions of the nanofilters were measured with a surface profilometer (Prometrix P-10, KLA-Tenco Co., CA) before the anodic bonding process. The depths and surface uniformity of the nanofilter shallow regions were further checked by imaging the cross-section of the nanofilter with scanning electron microscopy (SEM, JEOL6320FV, JEOL USA, Inc., Peabody, MA) after anodic bonding.

Using the standard fabrication process, we can easily control different structural parameters of the nanofilter array, for example, the nanofilter shallow and deep region depths and the nanofilter pitch number. **Figure 3.3** shows the cross-sectional SEM images of the sealed nanofilter array devices. **Figure 3.3A** shows two SEM images of the alternating deep and shallow regions of the nanofilter array. In this particular example, the nanofilter deep region depth is about 300 nm, and the shallow region depth is about 55 nm. The pitch number of the nanofilter array is about 2 um. **Figure 3.3B** shows four different nanofilter shallow regions with different depths. As seen clearly from these SEM images, the nanofilter shallow region depth is very uniform, and its depth can be easily controlled during the fabrication process. We also checked the nanofilter array geometries across the whole 6-inch wafer using the surface profilometer before the anodic bonding step. We found very good uniformity of the nanofilter etch profile across the whole 6” wafer, with a variation of less than 8%.

In this thesis, the nanofilter array devices were fabricated on silicon substrates. However, similar fabrication process can also be applied to other common semiconductor substrates, such as quartz and glass. The nanofilter array devices can also be fabricated using standard sacrificial layer removal techniques [12].

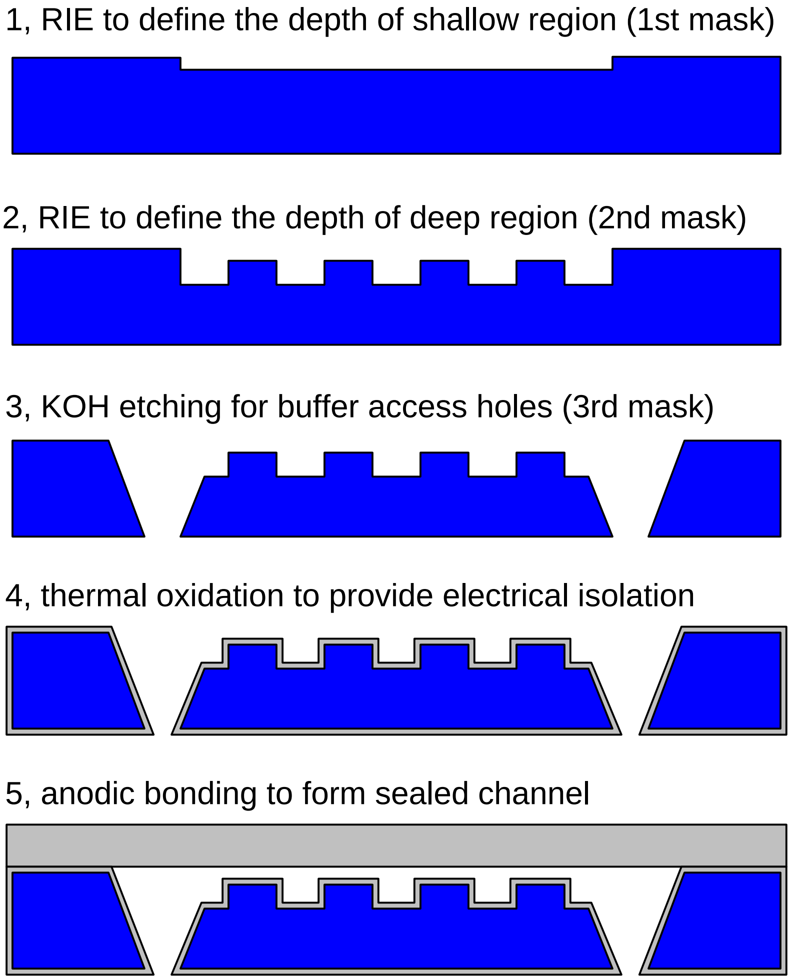

Figure 3.2: Fabrication process of the nanofilter array device.

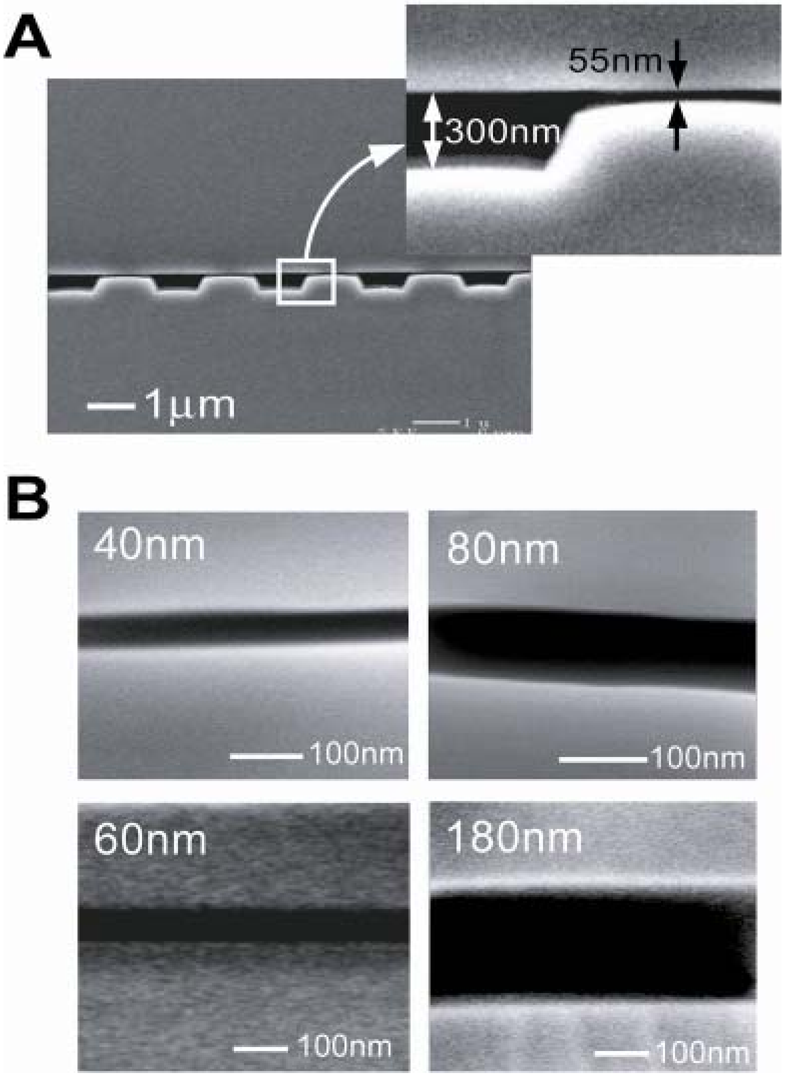

Figure 3.3: Cross-sectional scanning electron microscopy (SEM) images of the nanofilter array. (**A**) SEM images of an alternating deep (300 nm) and shallow (55 nm) regions of a nanofilter array. (**B**) SEM images of the cross section of different shallow regions with different depths (40, 60, 80, and 180 nm).

3.3 Experimental conditions

Figure 3.4 shows the experimental setup we used for testing the nanofilter array device with fluorescent-labelled DNA and protein molecules. The nanofilter array device was first filled with Tris-Borate-EDTA (TBE) buffer, and then the probe DNA and protein molecules were labelled with different fluorescence dyes.

Various dsDNA molecular weight (MW) ladder samples had been tested through the course of this thesis. All the dsDNA samples were purchased from New England BioLabs (Beverly, MA), and were labeled with the intercalating fluorescence dye YOYO-1 (Molecular Probes, Eugene, OR) in the TBE buffer. The dye to DNA base pair ratio was about 1:20 and the final DNA concentration in the sample solution was from about 10 μg/ml up to 100 μg/ml. We also applied the one-dimensional nanofilter array device to separate mixtures of proteins under denaturing conditions. The following commercially available Alexa Fluor 488-conjugated proteins were investigated in this thesis work (all purchased from Molecular Probes): cholera toxin subunit B (degree of labeling: 5 moles dye/mole, MW: 11.4 kDa), lectin phytohemagglutinin-L (degree of labeling: 3 moles dye/mole, MW: 120 kDa) and low density human lipoprotein (degree of labeling: 1 moles dye/mole, MW: 179 kDa). The complete denaturation and dissociation of these proteins was performed by adding sodium dodecyl sulfate (SDS, Sigma) and dithiothreitol (DTT, Sigma) to the protein mixture. The SDS-DTT-protein mixture contained 2 wt% SDS and 0.1M DDT and was incubated at 85°C for at least 10 minutes. The resultant SDS-protein complex solution was further diluted in the TBE buffer to a protein concentration of about 40 μg/ml. The final SDS-protein complex sample solution contained 0.1 wt% SDS and 5 μM DTT.

The dsDNA molecules can be considered as uniformly charged linear polyelectrolytes, since the phosphate groups associated with each nucleotide approximately carry two intrinsic negative charges [6]. It is also worthy to mention that the SDS and DTT treatment of the native proteins completely disrupts their native three-dimensional structures and shapes, dissociate them into polypeptide chains (the amino acid subunits), and impose comparable shapes and net charge densities on these chains. Dodecyl sulfate molecules bind strongly to polypeptide chains, with approximately one dodecyl sulfate molecule per two amino acid residues [13]. Each dodecyl sulfate molecule carries a negative charge, so a typical polypeptide of molecular weight of 40 kDa (with about 360 amino acids) acquires about 180 negative charges, which is far in excess of any net charge that might exist on the polypeptide chain originally in the buffer solution. Consequently, the charge to size ratio is virtually identical for all SDS-denatured proteins. Therefore separation of the dsDNA molecules and denatured proteins through the nanofilter array can occur only as a result of the size-sieving effect through the nanofilter constriction.

In all the experiments with dsDNA molecules and denatured proteins, the one-dimensional nanofilter array devices were filled with the high ionic strength TBE buffer (TBE 5×, 0.445 M Tris-Borate, 10 mM EDTA, pH~8.3). Additional 0.1 wt% SDS was added to the TBE 5× buffer for the denatured protein experiments. There are two effects of the high ionic strength buffer in our electrophoresis experiments. First, the high ionic strength buffer effectively diminishes the electroosmotic flow in the nanofilter array device [14]; therefore, in all our experiments, migration of dsDNA and denatured proteins followed the direction of electrophoresis. This enables us to easily control the migration direction of both dsDNA molecules and denatured proteins in our devices using the applied electric fields. The electroosmotic flow is associated with the device surface charge density (or the *zeta* potential), which is dependent on the surface treatment and cleaning methods during the fabrication process [14]. Therefore, the electroosmotic flow in the nanofluidic device can be difficult to control. Second, since the TBE 5× buffer has an equivalent ionic strength about 130 mM with a corresponding Debye length λ_D of about 0.84 nm (much smaller than the nanofilter shallow region depth d_s tested in this thesis) [15], the Debye layer should have negligible effects for the migrating biomolecules across the nanofilter array. Therefore, the jump dynamics of biomolecules across the nanofilter is dictated by steric interactions.

The one-dimensional nanofilter array devices were mounted on an inverted epi-fluorescence microscope (IX-71, Olympus, Melville, NY). The microscope was equipped with a thermoelectrically cooled CCD camera (Sensicam QE, Cooke Co., Auburn Hill, MI) for fluorescence imaging. A 100W mercury lamp (Chiu Technical Corp., Kings Park, NY) was used for illumination. Laser induced fluorescence (LIF) detection system was also used in some electrophoresis experiments. All the biomolecules were observed using a FITC filter set (exitation: 482 nm, emission: 536 nm, Semrock, Rochester, NY). The images were further analyzed with image processing software (IPLab, Scanalytics, BD Bioscience, Rockville, MD).

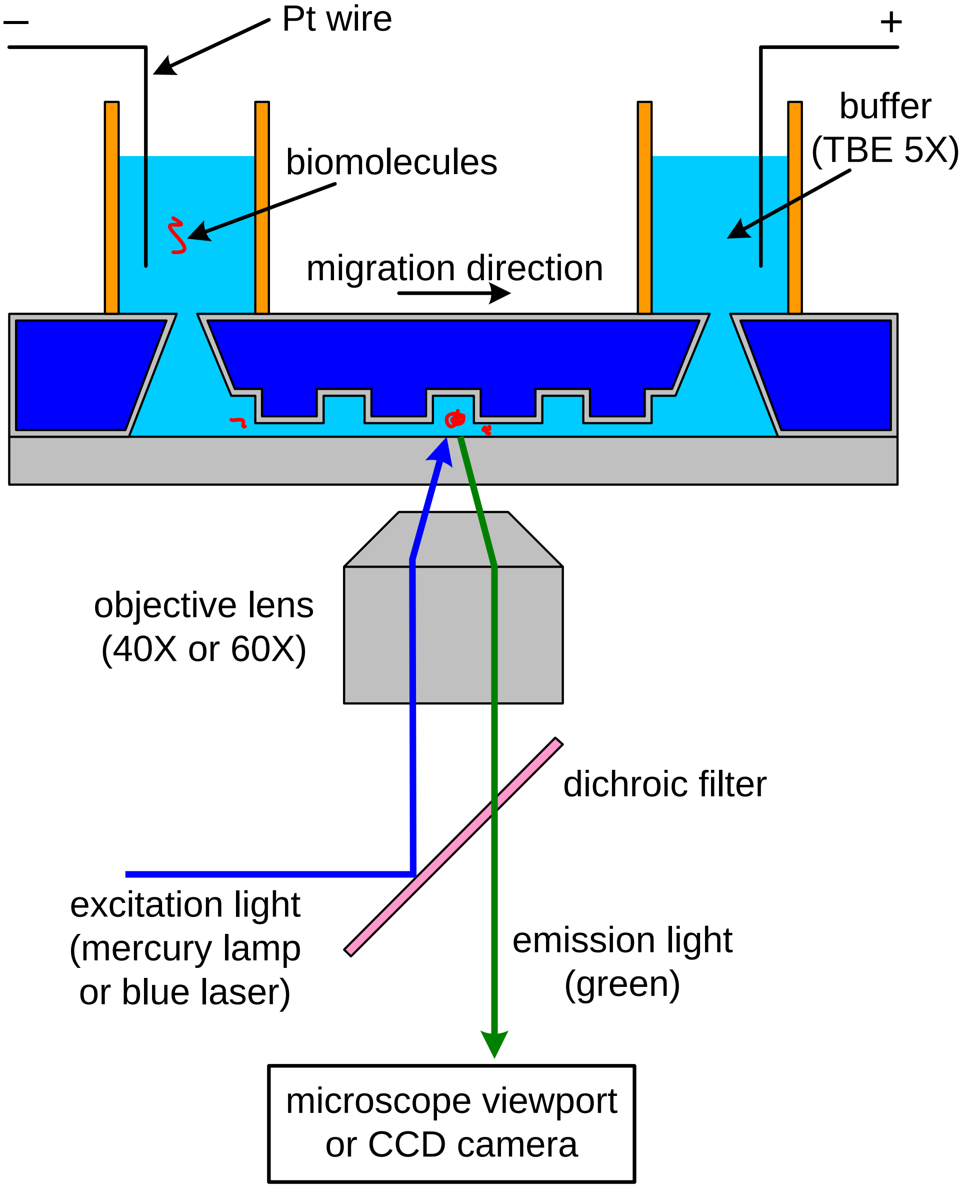

Figure 3.4: Experimental setup for observation of migration of fluorescent-labeled biomolecules through the nanofilter array devices.

3.4 Ogston sieving for size-based separation of DNA and proteins

The layout of the one-dimensional nanofilter array device is presented in **Fig. 3.5**. At the very beginning of the 1-cm long nanofilter array, a T-shaped injector for electrokinetic sample injection was fabricated to define and launch an initial biomolecule mixture plug of 40-μm wide. **Figure 3.6** shows a sequence of fluorescence images recorded by the CCD camera when a protein mixture was injected into the nanofilter array using the T-shaped injector. The injection volume for each injection was around 1 pL.

Figure 3.7 presents a sequence of fluorescence images showing separation of three different sized denatured proteins through the one-dimensional nanofilter array (d_s: 60 nm, d_d: 300 nm, p: 1 μm). The three proteins were cholera toxin subunit B (molecular weight (MW): 11.4 kDa), lectin phytohemagglutinin-L (MW: 120 kDa), and low density human lipoprotein (MW: 179 kDa). The three images were taken near the T-shaped injector region, shortly after the launching of the protein mixture. The applied electric field through the nanofilter array was 100 V/cm. The three proteins were quickly separated within 30 sec and a 570 μm separation length (about 500 nanofilters). Different sized proteins can be clearly identified from each other as evidenced by the three distinct migration bands (**Fig. 3.7**). Smaller protein fragments migrated faster than larger ones, which is consistent with the Ogston sieving mechanism and is different from the entropic trapping-based separation of long DNA molecules in similar nanofluidic devices [7].

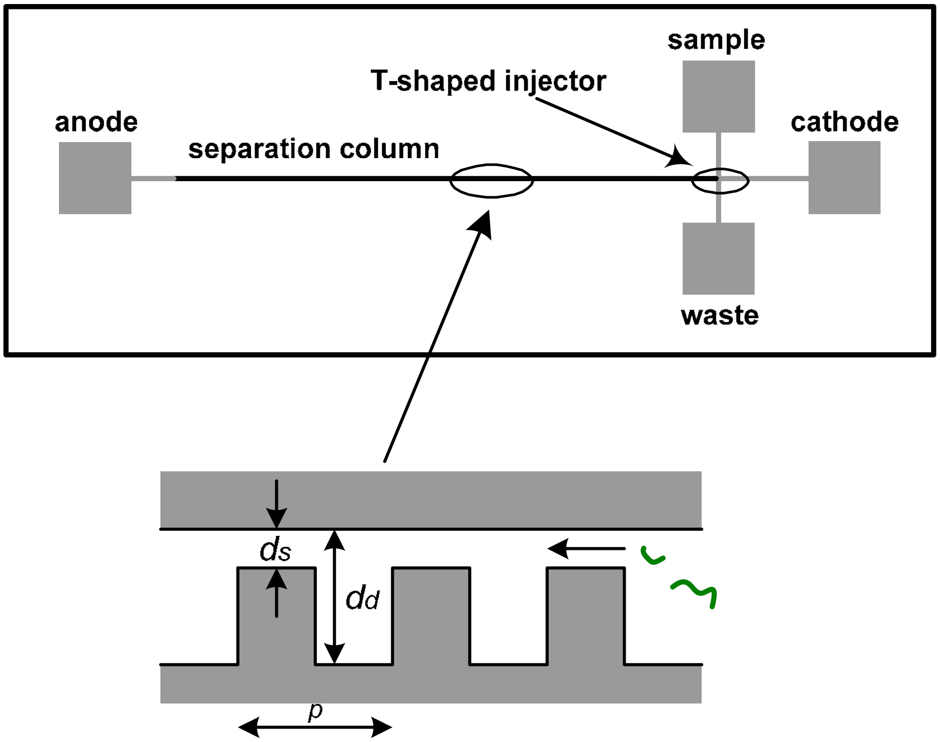

Figure 3.5: Layout of the one-dimensional nanofilter array device. The device includes four buffer access holes (anode, cathode, sample and waste), a 1-cm separation column (the one-dimensional array of nanofilter) and a T-shaped injector.

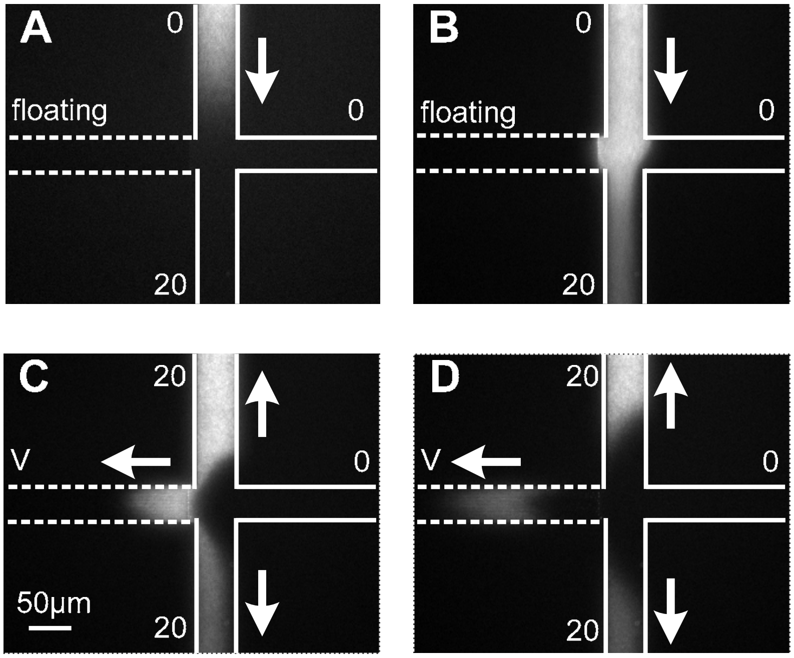

Figure 3.6: Sequence of fluorescence images showing the protein mixture injected into the nanofilter array using the T-shaped injector. The solid lines indicate the T-shaped injector and the dashed lines indicate the nanofilter array. The numerical values listed on the images indicate the different voltages applied at the four buffer access holes (unit: V, top: sample, bottom: waste, left: anode, right: cathode). *V* is the voltage applied at the anode. The thick arrows indicate the biomolecule migration directions inside different regions of the nanofilter device.

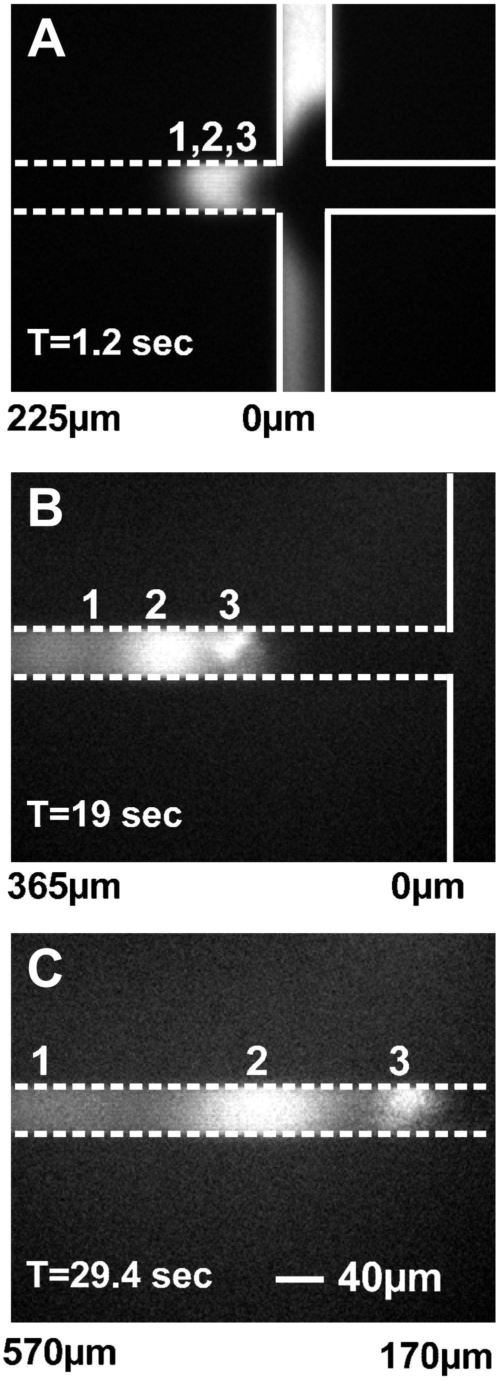

Figure 3.7: Sequence of fluorescence images showing separation of proteins through the one-dimensional nanofilter array device (d_s: 60nm, d_d: 300nm, p: 1μm). Band assignment: (1) cholera toxin subunit B; (2) lectin phytohemagglutinin-L; (3) low density human lipoprotein.

Figure 3.8 summarizes the electropherograms we recorded in the middle of the 1-cm separation channel (separation distance: 5 mm) under different applied electric fields. The base-line separation of the proteins was achieved within 4 min under an electric field of 90 V/cm (**Fig. 3.8**).

We can quantitatively characterize the separation efficiency of the one-dimensional nanofilter array by calculating the theoretical plate number N_p, the theoretical plate height H, and the separation resolution R_s between the different protein peaks [16]. The one-dimensional nanofilter array device is an elusion separation system, therefore the theoretical plate number N_p for each peak can be calculated as $N_p = 1.39 \times (t / \Delta t_{1/2})^2$, where t is the migration time and $2\Delta t_{1/2}$ is the measured full width at half maximum of the peak. In this thesis work, we have used Gaussian functions for fitting to determine the means (the maximum intensity) as well as the peak widths for all the electropherograms and fluorescence intensity profiles measured. The theoretical plate height (H) can be calculated as $H = n_{trap}p/N_p$, where $n_{trap}p$ represents the separation column length or separation distance (n_{trap}: number of nanofilter, p: nanofilter pitch number). The separation resolution $R_{s,12}$ between two peaks (peak 1 and 2) is calculated by using the expression $R_{S,12} = 0.59 \times (t_2 - t_1)/(\Delta t_{1/2,1} + \Delta t_{1/2,2})$, where t_1 and t_2 are the migration time of peak 1 and 2 and $2\Delta t_{1/2,1}$ and $2\Delta t_{1/2,2}$ are the respective full widths at half maximum.

The theoretical plate number N_p for cholera toxin subunit B was about 1523 and the plate number per column length was about 3×10^5 plates/m under the electric field of 90 V/cm (**Fig. 3.8**). Such separation performance obtained by the one-dimensional nanofilter array chip is comparable to microchip-based gel electrophoresis system, and is better than current state of the art separation systems (*i.e.* capillary gel electrophoresis) without using any sieving gel [17]. Since the denatured proteins tested are smaller than the 60 nm nanofilter shallow region depth, **Figure 3.8** clearly demonstrates the effectiveness of Ogston sieving in the nanofilter array and further is a direct experimental confirmation of Ogston sieving in a well-defined, regular nanopore system.

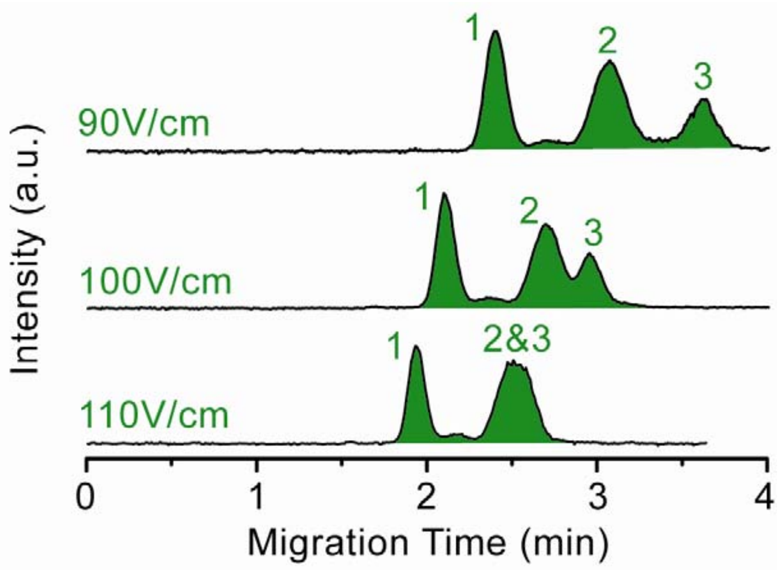

	$R_{S,12}$	$R_{S,23}$	N_{p1}	H_1	N_1/L
90V/cm	2.16	1.61	1523	3.28	3×10^5

Figure 3.8: Separation of proteins in a nanofilter array device (d_s: 60 nm, d_d: 300 nm, p: 1 μm) under different applied fields. Separation length: 5 mm. Band assignment: (1) cholera toxin subunit B (11.4 kDa); (2) lectin phytohemagglutinin-L (120 kDa); (3) low density human lipoprotein (179 kDa). $R_{S,\,ij}$: separation resolution between peak i and j; N_i, H_i: theoretical plate number and plate height (in μm) for peak i; N_i/L: theoretical plate number per column length (in plates/m).

Separation results of short dsDNA molecules in the one-dimensional nanofilter array device are shown in **Fig. 3.9**. The PCR marker contains 5 different DNA fragments of sizes ranging from 50 bp to 766 bp. Since the persistence length of DNA is about 50 nm (about the contour length of 150 bp DNA) [18], the PCR marker fragments appear relatively straight, and recognizable as rigid, rod-like molecules with an end-to-end distance of about 16 nm to 150 nm [19]. A complete separation of the PCR marker was achieved in about 10 min with a separation length of 5 mm under an electric field of 70 V/cm. Similar to the observations with the proteins, higher electric fields led to fast biomolecule separation; however, separation resolution was very much compromised. Reducing electric field led to improved separation resolution (**Fig. 3.8 & 3.9**).

The molecular sieving power of the nanofilter array showed dependence on the electric field strength. When the field was increased, the size dependence of electrophoretic mobility (or size selectivity) disappeared. This dependence of mobility on field strength was more apparent for longer molecules. For instance, when the electric field was increased from 70 V/cm to 100 V/cm, the 50 bp and 150 bp DNA fragments achieved 8.4% and 18.2% mobility increases, respectively, while the 766 bp DNA fragment achieved a 90.2% mobility increase (**Fig. 3.9**). This observation suggests that there is a competition between the electrical potential energy drop ΔW in the translation of charged DNA molecules over the nanofilter barrier ($\Delta W \sim ENq$, E: field strength, N: DNA base pair number, q: effective charge of dsDNA molecule per base pair) and the Ogston sieving induced entropic energy barrier ($\sim k_B T$). The Ogston sieving effect becomes less dominant as the electric field is increased, and this is especially true for longer DNA molecules. Therefore, the separation resolution worsened as the field was increased (**Fig. 3.8 & 3.9**).

It had also been proposed in the gel electrophoresis community that the field-dependent behavior of Ogston sieving can be attributed to the fact that, under a high electric field, biomolecules tend to be aligned with the direction of the field, and tend to have more favorable configurations to migrate through the nanofilter constriction [3, 6]. This field dependent reorientation phenomenon again effectively lowers the entropic barrier height, and this is especially true for longer biomolecules, since they are more readily to be deformed and re-oriented along the field direction [20]. Discussion of the high field effect on the re-orientation of the biomolecule along the field direction when crossing the nanofilter constriction is out the scope of this thesis; more details can be refereed elsewhere [20].

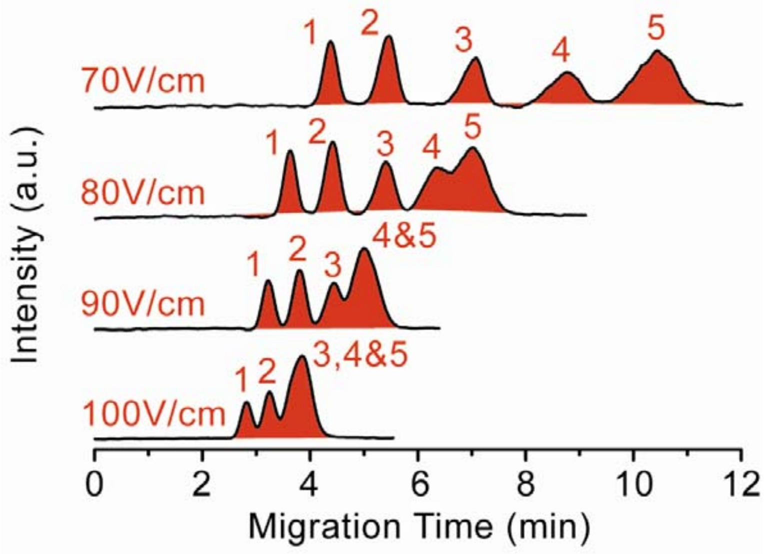

	μ_1	μ_2	μ_5	$R_{S,12}$	$R_{S,25}$
70V/cm	**2.72**	**2.17**	**1.14**	**2.17**	**5.41**
100V/cm	**2.95**	**2.57**	**2.17**	**1.14**	**1.05**

Figure 3.9: Separation of rigid, rod-like DNA molecules (PCR marker sample) in a nanofilter array device (d_s: 60 nm, d_d: 300 nm, p: 1 μm) under different applied fields. Separation length: 5 mm. Band assignment for DNA: (1) 50 bp; (2) 150 bp; (3) 300 bp; (4) 500 bp; (5) 766 bp. $R_{S,\,ij}$: separation resolution between peak i and j; μ_i: electrophoretic mobility of peak i (10^{-5} cm^2/(V·sec)).

3.5 Control experiments in flat nanofluidic channels

To ensure that separation of proteins and dsDNA with the one-dimensional nanofilter array devices was indeed due to the size-dependent molecular jump dynamics across the nanofilter constriction, we have performed control experiments with both proteins and DNAs inside flat nanochannels (with depth d_s of 60 nm to 100 nm) (**Fig. 3.10**). The control experiments were performed under TBE 5× buffer. Since the corresponding Debye length λ_D is about 0.84 nm, which is much smaller than the nanochannel depth, the Debye layer should have negligible effects for the migrating biomolecules inside the flat nanofluidic channels. The smallness of the Debye length λ_D ($\lambda_D << d_s$) also resulted in a plug flow profile of the electroosmotic flow (EOF) inside the nanochannel (**Fig. 3.10**) [21]. Please notice that the electroosmotic flow inside our nanofluidic devices is in the opposite direction as the electrophoresis of the negative-charged biomolecules.

We tested the PCR marker sample in a nanofluidic channel with a depth of 60 nm (**Fig. 3.11**). The PCR marker sample again contains 5 different DNA fragments of sizes ranging from 50 bp to 766 bp. However, as we can see from the electropherograms we recorded under a broad range of electric fields, no separation could be observed for the PCR marker. Similar experimental results have been observed with proteins.

From **Fig. 3.11**, we can easily conclude that the DNA electrophoretic mobility μ inside the nanochannel is size-independent and also field-independent. The constant value of the electrophoretic mobility μ can be treated as the free-draining mobility μ_0 of dsDNA molecules in our nanofluidic channels (which includes the effect of the EOF), and $\mu_0 = 1.01 \times 10^{-4}$ cm^2/(sec·V). Here we need to acknowledge that, the magnitude of the DNA free-draining mobility μ_0 in the nanofluidic channels is about four times less than the value reported by other groups from bulk free solution experiments where the free solution mobility was measured at about μ_0~4.5×10^{-4} cm^2/(sec·V) [22]. We suspect this discrepancy is due to the fact that the EOF inside the nanofluidic devices is in the opposite direction as the electrophoresis of the negative-charged biomolecules, and the electroosmotic flow can exert a certain drag force on the molecules, leading to reduced mobility.

The control experiments with the flat nanochannel (**Fig. 3.11**) confirmed that separation of proteins and DNA in the one-dimensional nanofilter array device was indeed due to the existence of the nanofilters, not due to chromatographic interaction between the nanofilter walls and the molecules. The small Debye length also excluded the possibility of hydrodynamic chromatography caused by the parabolic velocity profile in the large Debye length limit [23]. The possibility of the dielectrophoretic trapping, induced by the field gradient at the boundaries between the nanofilter deep regions and shallow regions, may cause the separation of molecules with different sizes [24], even at DC conditions [25]. However, if that were the case, the increased driving electric fields should have resulted in stronger trapping and therefore more resolved separation, which is a contradiction from our experimental observations.

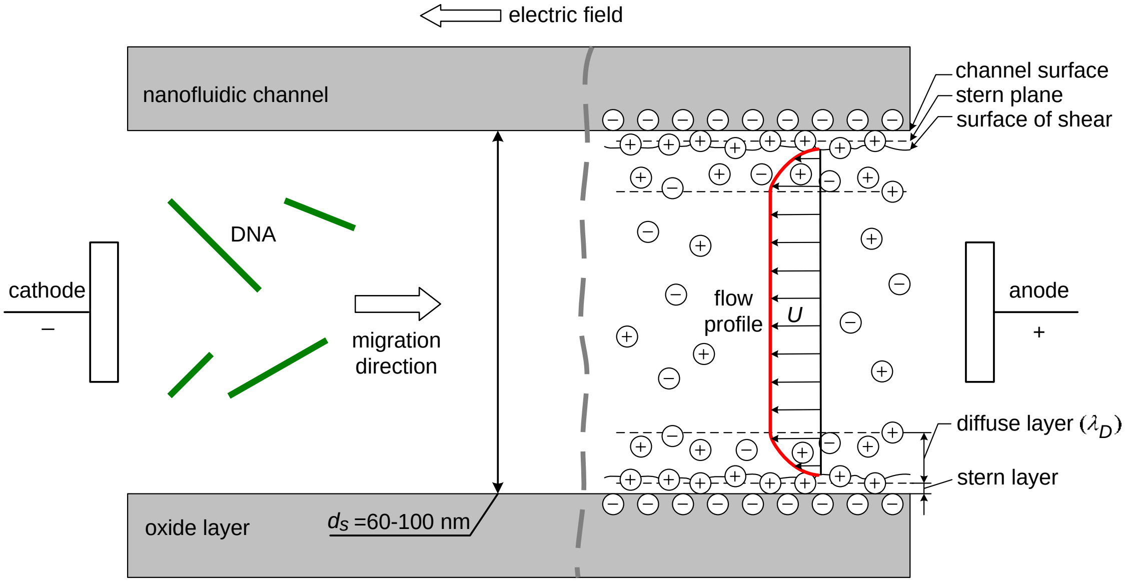

Figure 3.10: Electromigration of rigid, rod-like DNA molecules in a flat nanofluidic channel with depth of 60 nm to 100 nm (d_s). Right side shows a schematic of electroosmotic flow inside the nanofluidic channel including the structure of the Debye layer with inner Stern layer (not to scale).

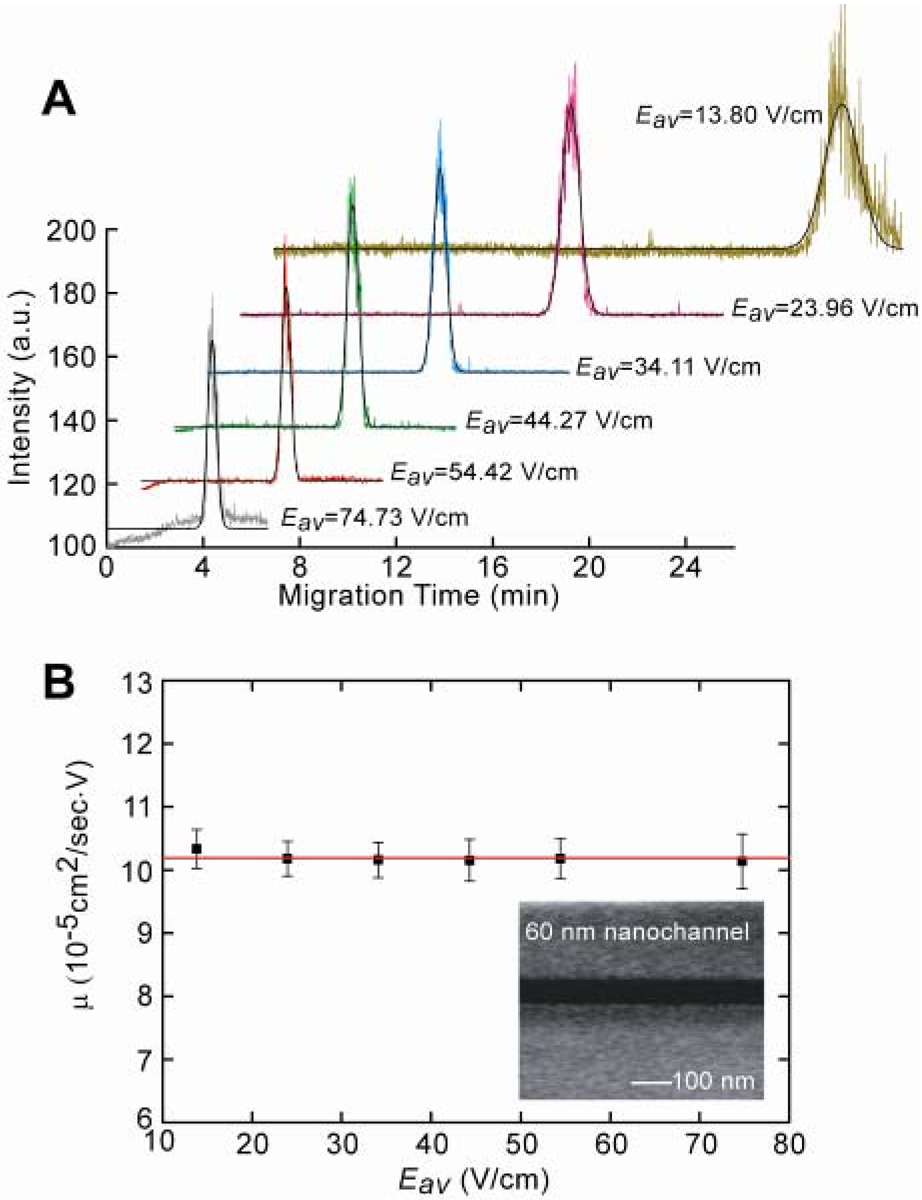

Figure 3.11: Separation of the PCR marker in the 60 nm flat nanochannel. (**A**) Electropherograms recorded at a separation distance of 2 cm under different electric fields. (**B**) Apparent electrophoretic mobility μ of the PCR marker sample as a function of applied electric fields.

3.6 Separation efficiency depending on nanofilter array geometry

Separation of biomolecules through the one-dimensional nanofilter array depends on both the operational conditions and the nanofilter structural parameters. The operation conditions include the applied electric field, temperature, and buffer conditions. The nanofilter structural parameters include the shallow and deep region depths, and the nanofilter pitch number. Since the effects of temperature and buffer conditions on the separation have been well-documented elsewhere [26, 27], here we focus only the effects of the applied electric field and the nanofilter geometry on the separation.

To investigate the electric field effect on the separation, we further performed electrophoresis experiments with two different DNA ladder samples (low molecular weight DNA ladder sample and 100 bp DNA ladder sample) in two different nanofilter array devices. The size dependent electrophoretic mobilities μ of dsDNA molecules were measured and analyzed. **Figure 3.12** shows the electropherograms of these two ladder samples under varied applied electric fields. **Figure 3.13** plots the mobility μ of dsDNA fragments as a function of the dsDNA length. Again, we found the Ogston sieving effect of the nanofilter array was modulated by the electric field strength. Higher electric fields resulted in fast separation; however, separation resolution was compromised. Reducing the electric field led to improved separation resolution. The size selectivity of the nanofilter array (defined as $d\mu/dN$) can be calibrated from the slopes of the mobility curves. As the electric field E_{av} was decreased, the mobility slope showed tendency to become steeper, indicating better selectivity (**Fig. 3.13**). The field-dependent observation could not be correlated directly to the extended Ogston model for the conventional gel electrophoresis, since the extended Ogston model is essentially a low-field (near equilibrium) model. This difficulty leads us to think more carefully about the local biomolecular jump dynamics across the nanofilter. We will get back to this point with more details in the next chapter.

Here it is worth mentioning the tradeoff between increasing the nanofilter size selectivity by reducing the electric field E_{av} and the separation time. A first-order of estimation of the separation speed can be calculated from the maximum sieving free mobility μ_{max} and the electric field E_{av} in the nanofilter array. The maximum sieving free mobility μ_{max} depends solely on the nanofilter structural parameters. Since all the nanofilter arrays tested in this thesis consist of equal deep and shallow region lengths, μ_{max} can be expressed as [28]

$$\mu_{\max} = \mu_0 \frac{4\gamma}{(1+\gamma)^2} \tag{3.1}$$

where γ is the ratio of the nanofilter deep region and shallow region depths and $\gamma=d_d/d_s$. Therefore, the total separation time T_{travel} under a certain separation condition can be roughly estimated by

$$T_{travel} \approx \frac{n_{trap}p}{E_{av}\mu_{\max}} = \frac{n_{trap}p(1+\gamma)^2}{4\gamma E_{av}\mu_0} \tag{3.2}$$

From Eq. (3.2), we can determine that the separation time is linearly proportional to the separation distance and inversely proportional to the electric field E_{av}. Therefore, reducing E_{av} lengthens the separation time. The total separation time decreases faster than $1/E_{av}$, since the DNA mobility decreases with decreasing electric field strength (**Fig. 3.13**).

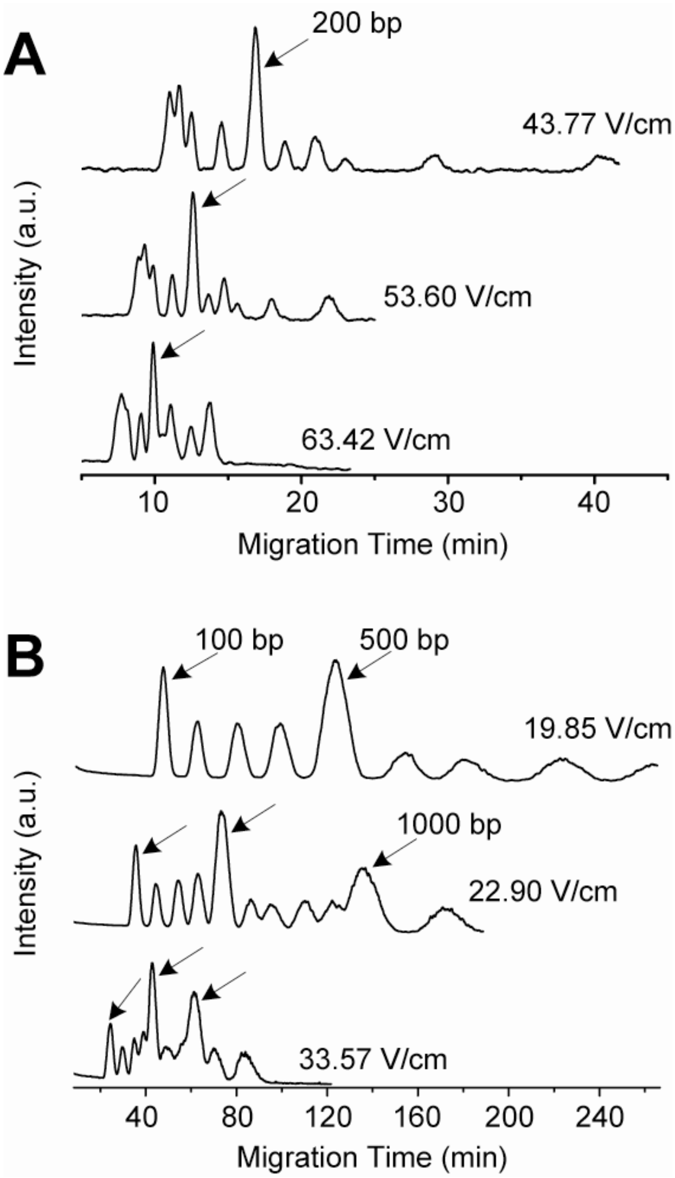

Figure 3.12: Separation of low molecular weight DNA ladder (**A**) and 100 bp DNA ladder (**B**) in nanofilter array devices (for **A**: d_s=55 nm, d_d=300 nm, and p=1 μm; for **B**: d_s=80 nm, d_d=500 nm, and p=4 μm). The low molecular weight DNA ladder includes 11 fragments with sizes ranging from 25 bp to 766 bp, and the 200 bp fragment has increased intensity to serve as a reference peak (see arrow mark); the 100 bp DNA ladder contains 12 bands with sizes ranging from 100 bp to 1517 bp, and the 100, 500 and 1000 bp bands have increased intensity to serve as reference peaks. The electropherograms were all taken 1 cm from the injection point with the indicated fields.

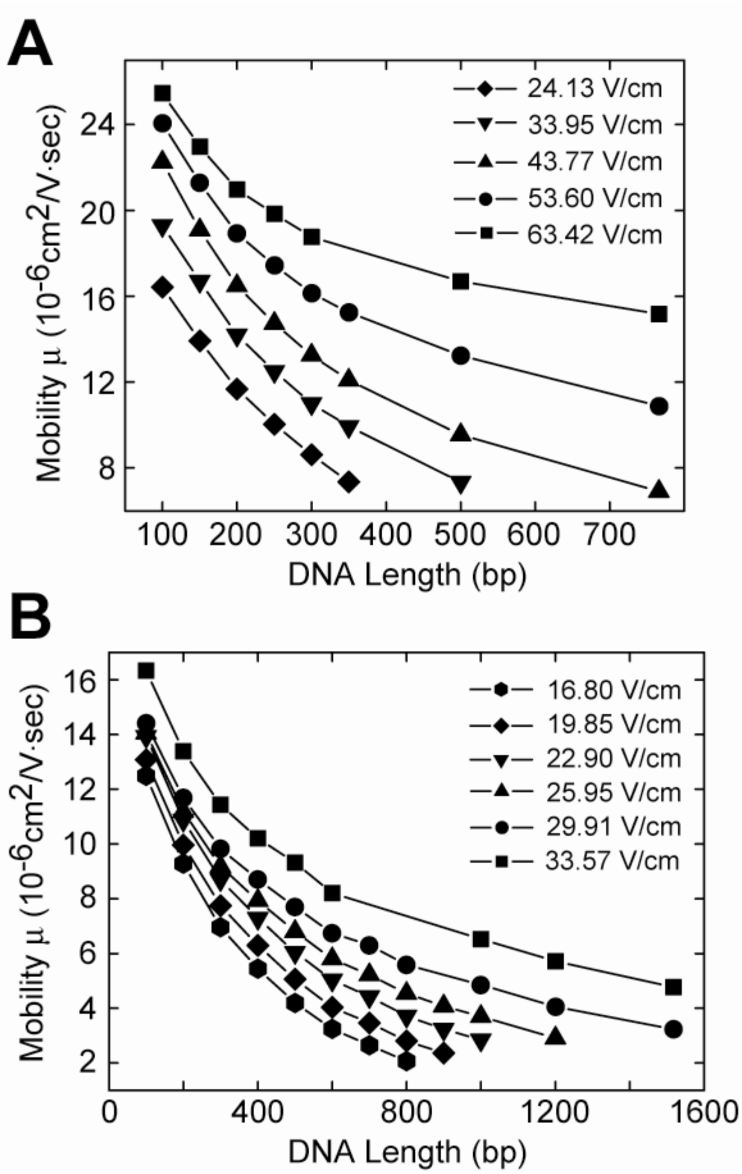

Figure 3.13: Electrophoretic mobility *μ* of DNA fragments as a function of dsDNA length. **A**: the low molecular weight DNA ladder sample in the 55 nm nanofilter device; **B**: the 100 bp DNA ladder sample in the 80 nm nanofilter device.

In **Fig. 3.14**, we compared three different nanofluidic devices with different structures but the same nanochannel depth to separate proteins (d_s=60 nm). In the flat nanofluidic channel device (*device 1*), no separation over a 2 cm separation length was observed for the protein mixture under a broad range of fields applied (**Fig. 3.14A**). Again, this experiment confirmed that separation in the nanofilter array was indeed due to the nanofilters, not due to other interactions between the nanofilter walls and the molecules. *device 2* and *device 3* had different periods (p) and different deep region depths (d_d). It was possible to achieve separation with high fields (up to ~100 V/cm) in *device 3* but not in *device 2* due to the difference in their geometries (separation resolution would be lost with a field higher than ~60 V/cm in *device 2*). A more than 10-fold increase of the separation speed was obtained in *device 3* than in *device 2* for comparable separation resolution. This can be attributed to three different separation relevant parameters of these two devices: the separation length, the electric field and the aspect ratio of the nanofilter ($\gamma=d_d/d_s$). The decrease of γ with shallower depth of d_d in *device 3* increased the separation speed (μ_{max}/μ_0(*device 3*)=0.55>μ_{max}/μ_0(*device 2*)=0.34). Overall, the shorter separation length, the greater field and the reduced aspect ratio leaded to the more than 10-fold increase of the separation speed in *device 3*. Similar improvement is expected when the nanofilter period is further decreased, possibly either by e-beam lithography [29] or by nanoimprint lithography [30]. A nanofilter with a period of 100- to 200 nm is still much larger than the size of proteins and other biomolecules, so similar sieving behavior is expected in such devices.

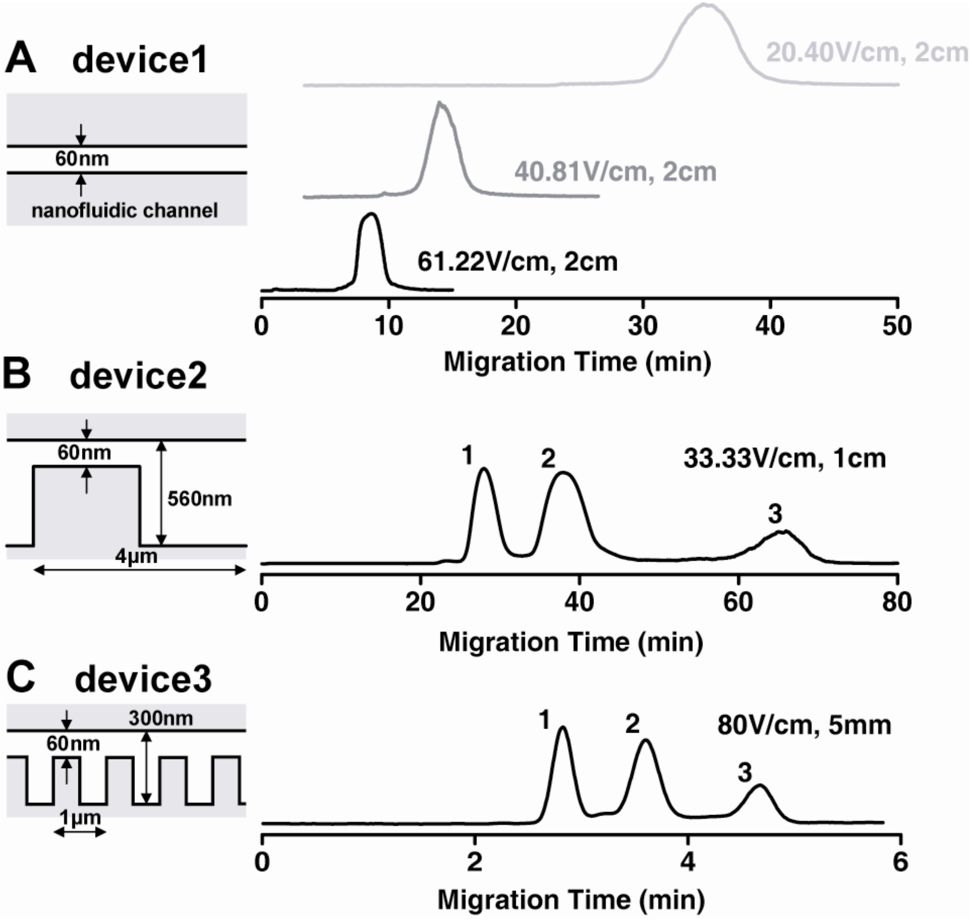

Figure 3.14: Comparison of separation performance in three different nanofluidic devices. *Device 1* has only a 60 nm thin, flat channel without any nanofilter. *Device 2*: d_s=60 nm, d_d=560 nm, p=4 µm; *Device 3*: d_s=60 nm, d_d=300 nm, p=1 µm. Band assignment is the same as in **Fig. 3.6** for proteins. The separation lengths and the applied fields are indicated in the figures.

3.7 References

1. Ogston, A. G. The spaces in a uniform random suspension of fibres. *Trans. Faraday Soc.* **54**, 1754–1757 (1958).
2. Rodbard, D. & Chrambach, A. Unified theory for gel electrophoresis and gel filtration. *Proc. Natl. Acad. Sci. U. S. A.* **65**, 970–977 (1970).
3. Tietz, D. Evaluation of mobility data obtained from gel electrophoresis: strategies in the computation of particle and gel properties on the basis of the extended Ogston model. *Advances in Electrophoresis* (VCH Publishers, New York, 1988), Vol. 2, 109–169.
4. Kozulic, B. Models of gel electrophoresis. *Anal. Biochem.* **231**, 1–12 (1995).
5. Slater, G. W., Mayer, P. & Drouin, G. Migration of DNA through gels. *Methods Enzymol.* **270**, 272–295 (1996).
6. Viovy, J.-L. Electrophoresis of DNA and other polyelectrolytes: physical mechanisms. *Rev. Mod. Phys.* **72**, 813–872 (2000).
7. Han, J., Turner, S. W. & Craighead, H. G. Entropic trapping and escape of long DNA molecules at submicron size constriction. *Phys. Rev. Lett.* **83**, 1688–1691 (1999).
8. Nykypanchuk, D., Strey, H. H. & Hoagland, D. A. Brownian motion of DNA confined within a two-dimensional array. *Science* **297**, 987–990 (2002).
9. Giddings, J. C., Kucera, E., Russell, C. P. & Myers, M. N. Statistical theory for the equilibrium distribution of rigid molecules in inert porous networks. Exclusion chromatography. *J. Phys. Chem.* **72**, 4397–4408 (1968).
10. Deen, W. M. Hindered transport of large molecules in liquid-filled pores. *AIChE J.* **33**, 1409–1425 (1987).
11. Giddings, J. C. *Dynamics of Chromatography. Part 1. Principles and Theory* (Marcel Dekker, New York, 1965).
12. Madou, M. *Fundamentals of Microfabrication*. (CRC Press, Boca Raton, 1997).
13. Scopes, R. K. *Protein Purification, Principles and Practice* (Springer-Verlag, New York, ed. 3, 1993).
14. Han, J. & Craighead, H. G. Characterization and optimization of an entropic trap for DNA separation. *Anal. Chem.* **74**, 394–401 (2002).
15. Lide, D. R. *CRC Handbook of Chemistry and Physics* (Taylor and Francis, Boca Raton, FL, ed. 87, 2007).
16. Giddings, J. C. *Unified Separation Science* (John Wiley & Sons, New York, 1991).
17. Yao, G., *et al.* SDS capillary gel electrophoresis of proteins in microfabricated channels. *Proc. Natl. Acad. Sci. U. S. A.* **96**, 5372–5377 (1999).
18. Hagerman, P. J. Flexibility of DNA. *Annu. Rev. Biophys. Chem.* **17,** 265–286 (1988).
19. Rubenstein, M. & Colby, R. H. *Polymer Physics* (Oxford, New York, 2003).
20. Laachi, N., Declet, C., Matson, C. & Dorfman, K. D. Non-equilibrium transport of rigid macromolecules in periodically constricted geometries. *Phys. Rev. Lett.* **98**, 098106 (2007).
21. Probstein, R. F. *Physicochemical Hydrodynamics. An Introduction* (John Wiley & Sons, New York, 1994).
22. Stellwagen, N. C., Gelfi, C. & Righetti, P. G. The free solution mobility of DNA. Biopolymers, **42**, 687–703 (1997).

23. Blom, M. T., Chmela, E., Oosterbroek, R. E., Tijssen, R. & van den Berg, A. On-chip hydrodynamics chromatography separation and detection of nanoparticles and biomolecules. *Anal. Chem.* **75**, 6761─6768 (2003).
24. Chou, C. F., *et al.* Electrodeless dielectrophoresis of single- and double-stranded DNA. *Biophys. J.* **83**, 2170─2179 (2002).
25. Cummings, E. B. & Singh, A. K. Dielectrophoresis in microchips containing arrays of insulating posts: theoretical and experimental results. *Anal. Chem.* **75**, 4724─4731 (2003).
26. Rothman, C. Temperature effect on separation of DNA in a nanofluidic molecular filter array. Advanced Undergraduate Project, Electrical Engineering, MIT (2005).
27. Bow, H. Characterization of nanofilter array for small molecule separation. Master Thesis, Electrical Engineering, MIT (2006).
28. Streek, M., Schmid, F., Duong, T. T. & Ros, A. Mechanisms of DNA separation in entropic trap arrays: a Brownian dynamics simulation. *J. Biotechnol.* **112**, 79─89 (2004).
29. Turner, S. W., Perez, A. M., Lopez, A. & Craighead. H. G. Monolithic nanofluid sieving structures for DNA manipulation. *J. Vac. Sci. Technol. B* **16**, 3835─3840 (1998).
30. Cao, H. *et al.* Fabrication of 10 nm enclosed nanofluidic channels. *Appl. Phys. Lett.* **81**, 174─176 (2002).

Chapter 4

Molecular sieving in periodic free-energy landscapes created by patterned nanofilter arrays

In this chapter, we present an experimental study of Ogston sieving process of rigid rod-like DNA in patterned one-dimensional periodic nanofluidic filter arrays. The electrophoretic motion of DNA through the nanofilter array is described as a biased, thermally activated (Brownian) motion overcoming periodically modulated free energy landscapes. A kinetic model, constructed based on the equilibrium partitioning theory and the Kramers rate theory, explains the field-dependent DNA mobility well. At the end of the chapter, we further show experimental evidence of the crossover from Ogston sieving to entropic trapping, depending on the ratio between nanofilter constriction size and DNA size.

4.1 Introduction: the extended Ogston model in gel electrophoresis

The standard model for interpreting gel electrophoresis mobility μ in the Ogston sieving regime is the so-called "extended Ogston model" [1-6], where the relative mobility μ^*, the ratio between the mobility μ in gel and the free solution mobility μ_0, of a molecule of given size is assumed to equal the partition coefficient K of the molecule in the gel (K

revolves around excluded volume in general configuration space). Even though the assumption of $\mu^*=\mu/\mu_0=K$ has never been properly tested experimentally, largely because the mobility μ and the partition coefficient K of the molecule cannot be measured independently for a gel system, the extended Ogston model has been applied as the theoretical basis for the widely accepted empirical method proposed by Ferguson for determining the molecular weights of biomolecules [3]. The extended Ogston model in gel electrophoresis is essentially a low-field (near equilibrium) model, and therefore it cannot account for many important characteristics of gel electrophoresis. For example, the extended Ogston model is known for failing to explain field-dependent mobility shifts that occur in a medium-to-high field gel electrophoresis [3, 6].

The theoretical study of sieving mechanisms in gel electrophoresis has been fundamentally limited by the lack of well-controlled experimental platforms for correlating the size and shape of the sieving pores to the observed molecular dynamic behavior. Recently, various microfabricated structures have been proposed as an alternative to the gels (see discussions in **Chapter 1**). These regular sieving structures have also proven ideal for theoretical study of molecular dynamics and stochastic motion in confining spaces, due to their precisely defined environments [7, 8]. For example, detailed theoretical models of entropic trapping have been developed based on the first principles to optimize the separation process in the entropic trap array device [9, 10].

In the previous chapter, we have proven that patterned one-dimensional periodic nanofilter arrays can provide fast separation of physiologically-relevant molecules such as proteins based on the Ogston sieving mechanism [11]. More interestingly, we found the Ogston sieving process of the nanofilter array showed dependence on the electric field strength, and this field-dependent observation could not be correlated directly to the extended Ogston model for the conventional gel electrophoresis, since the extended Ogston model is essentially a quasi-equilibrium model that doesn't account for the electric field effect on the biomolecule migration in the gel.

In this chapter, by using a theoretical model based on the equilibrium partitioning theory and the Kramers rate theory, we quantitatively characterized the local biomolecular jump dynamics across the nanofilter, and further calculated the size- and field-dependent mobility of biomolecules in different microfabricated periodic nanofilter arrays.

4.2 Kramers rate theory

Before we proceed to calculate the DNA mobility in the nanofilter array, we will introduce the well-known calculation by Kramers of the rate of passage of a Brownian particle over a potential-energy barrier. The general Kramers result comes from the Fokker-Planck equation in the full phase space of the Brownian particle [12, 13]. Here to simplify the calculation, we focus ourselves on the simple case of the diffusion limit (the overdamped regime), which permits direct use the solution of the simplified one-dimensional Fokker-Planck equation. The discussion below is patterned after very clear expositions by Brinkman and Stockmayer [14, 15].

We can write down the force balance equation F for molecules in the dilute solution as (here we treat the molecules as point-like particles)

$$\eta(u-v)=F=-\nabla(k_B T\ln f+U) \tag{4.1}$$

where η is the friction constant, u represents the molecular velocities and v represents the solvent velocities at the positions of the molecules. In this thesis work, we neglect the solvent flow (*e.g.*, EOF flow), and therefore v=0. U is the Gibbs free energy and in our case, U is entirely intramolecular (a dilute solution case), but contains contributions from interaction with external fields as well as from the free energy of the chain conformational and bonding interactions. Finally, f is the time-dependent distribution function of the molecule coordinates.

In this thesis, we are interested in the steady-state net rate of passage of Brownian particles from the left to the right side of the barrier (**Fig. 4.1**). Therefore, we can re-write Eq. (4.1) in terms of molecular current in one dimension as

$$J = uf = -\frac{k_B T}{\eta}\left(\frac{df}{dx} + \frac{f}{k_B T}\frac{dU}{dx}\right) \tag{4.2}$$

Eq. (4.2) can be easily re-arranged to read

$$Je^{U/k_B T} = -\frac{k_B T}{\eta}\frac{d}{dx}\left(fe^{U/k_B T}\right) \tag{4.3}$$

Integration of Eq. (4.3) from points A and B yields

$$\int_A^B Je^{U/k_B T}dx = -\frac{k_B T}{\eta}\left(f_B e^{U_B/k_B T} - f_A e^{U_A/k_B T}\right) \tag{4.4}$$

The discussion of the left hand side of Eq. (4.4) is facilitated by the assumption that the barrier height U^* is sufficiently high compared to thermal energy ($k_B T$). Therefore, we can safely assume the flat region near the top of the barrier gives the majority contribution to the integral (with the current at the top of the barrier as J_c). Then from Eq. (4.4), we can have

$$\begin{aligned}&\int_A^B J e^{U/k_BT}dx \approx J_C\int_A^B e^{U/k_BT}dx \approx -\frac{k_BT}{\eta}(f_Be^{U_B/k_BT}-f_Ae^{U_A/k_BT})\\&\Rightarrow\ J_C \approx -\frac{k_BT}{\eta}\left[\int_A^B e^{U/k_BT}dx\right]^{-1}(f_Be^{U_B/k_BT}-f_Ae^{U_A/k_BT})\end{aligned}\tag{4.5}$$

The fraction of molecules in the total ensemble which are on the left side of the barrier can be calculated as

$$n_A=\int_{-\infty}^{C} f dx=\int_{-\infty}^{C} f_A e^{-(U-U_A)/k_BT}dx \approx f_A e^{U_A/k_BT}\int\limits_{trap\ A} e^{-U/k_BT}dx \tag{4.6}$$

where we have assumed the majority of the molecules on the left side will be found near the bottom of the potential trap *A*, and in the region, the molecule distribution is approximated with a Boltzmann distribution ($f=f_Ae^{-(U-U_A)/k_BT}$). Similarly, the fraction of molecules on the right side is

$$n_B=\int_{C}^{\infty} f dx \approx f_B e^{U_B/k_BT}\int\limits_{trap\ B} e^{-U/k_BT}dx \tag{4.7}$$

Combining Eq. (4.5), (4.6) & (4.7), we have

$$J_C=k_An_A-k_Bn_B \tag{4.8}$$

where k_A, the forward escape rate constant is given by

$$k_A=\frac{k_BT/\eta}{\int_A^B e^{U/k_BT}dx\int\limits_{trap\ A} e^{-U/k_BT}dx} \tag{4.9}$$

Eq. (4.9) can be specialized to various shapes of potential-energy barriers. For example, if we assume parabolic shapes of the energy profiles in the neighborhoods of the points *A* and *C* as

$$U = U_A + (m\omega_A^2 / 2)(x - x_A)^2 + \cdots$$
$$\Rightarrow \int_{trap\ A} e^{-U/k_BT} dx = e^{-U_A/k_BT} (2\pi k_B T / m\omega_A^2)^2 \tag{4.10}$$

and

$$U = U_C - (m\omega_C^2 / 2)(x - x_C)^2 + \cdots$$
$$\Rightarrow \int_A^B e^{U/k_BT} dx = e^{U_C/k_BT} (2\pi k_B T / m\omega_C^2)^2 \tag{4.11}$$

where m is the molecular weight, ω_A and ω_C denote the angular frequencies of the energy profile near the points A and C. Combining Eq. (4.9), (4.10) and (4.11), we can obtain the famous form of the escape rate constant of passage over the barrier in the Kramers rate theory (in the diffusion limit) as

$$k_A = \frac{\omega_A \omega_C m}{2\pi\eta} \cdot e^{-(U_C - U_A)/k_BT} = \frac{\omega_A \omega_C m}{2\pi\eta} \cdot e^{-U^*/k_BT} \tag{4.12}$$

If we assume linear shapes of the energy profiles in the neighborhoods of the points A and C as

$$U = U_A - S_A(x - x_A)$$
$$\Rightarrow \int_{trap\ A} e^{-U/k_BT} dx \approx \int_{-\infty}^{x_A} e^{-U/k_BT} dx = \frac{k_B T}{S_A} e^{-U_A/k_BT} \tag{4.13}$$

and

$$U = U_C - S_C(x - x_C)$$
$$\Rightarrow \int_A^B e^{U/k_BT} dx \approx \int_{x_C}^{+\infty} e^{U/k_BT} dx = \frac{k_B T}{S_C} e^{U_C/k_BT} \tag{4.14}$$

where S_A and S_C denote the linear slopes of the energy profile near the points A and C. Combining Eq. (4.9), (4.13) and (4.14), we can obtain another escape rate constant of passage over the barrier as

$$k_A = \frac{k_B T / \eta}{\int_A^B e^{U/k_B T} dx \int\limits_{trap\ A} e^{-U/k_B T} dx} = \frac{S_A S_C}{k_B T \eta} \cdot e^{-U^*/k_B T} \tag{4.15}$$

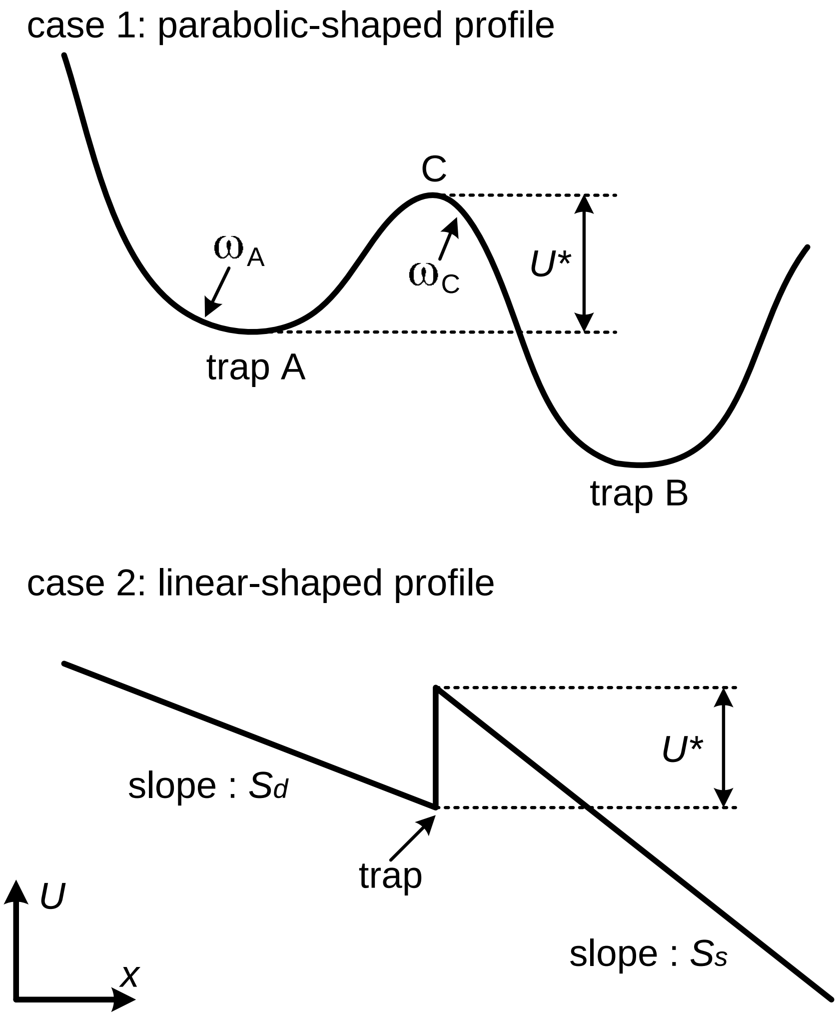

case 1: parabolic-shaped profile

case 2: linear-shaped profile

Figure 4.1: Double well potential for the Kramers problem. The free energy profile contains two minima *A* and *B* along the coordinate *x*. The two minima are separated by the barrier at point *C*. Top: parabolic-shaped energy profile. Bottom: linear-shaped energy profile.

4.3 Molecular sieving in period free-energy landscapes created by patterned nanofilter arrays

To facilitate theoretical study of the local biomolecule jump dynamics across the nanofilter constriction, we have used rigid, rod-like dsDNA molecules as probe molecules (**Fig. 4.2**). These rigid, regular shaped molecules enabled us to obtain analytical solutions of the configurational entropic barrier for the molecule passage through the nanofilter constriction [16, 17].

We quantitatively characterized the sieving process of various short dsDNA molecules in different microfabricated periodic nanofilter arrays (**Fig. 4.3**; see other results in **Fig. 3.10 & 3.11**) [18]. The nanofilter arrays serve as the model pore-constriction system. The depth of the nanofilter shallow region (d_s) is of the same order of magnitude as the size of probing DNA molecules. Details of the nanofilter array structure and fabrication, and the experimental procedures are described in the previous chapters.

The electrophoretic drift of DNA through the nanofilter is essentially an electric-field-driven partitioning process [6]. Compared with the high-entropy nanofilter deep region, the limited DNA configurational space inside the nanofilter shallow region creates a configurational entropic barrier for DNA passage at the abrupt interface between the deep and shallow regions. This configurational entropic barrier originates from the steric constraints that prevent a partial overlap of DNA with the wall [16], and is different from the conformational entropic barrier associated with deformation and entropic elasticity (which are intrinsically enthalpy effects) [19, 20]. The configurational entropic barrier can be calculated as $-T\Delta S^0 \sim -k_B T \ln(\Omega_s/\Omega_d)$ (T: absolute temperature, S^0:

configurational entropy, k_B: Boltzmann's constant, Ω_s/Ω_d: ratio of accessible microscopic configuration state integrals within shallow and deep regions). By definition, Ω_s/Ω_d is equal to K ($K=K_s/K_d$), the ratio of the partition coefficients in the shallow and deep regions.

As discussed in **Chapter 2**, the partitioning of rigid molecules in various nanopore geometries has been studied both analytically and numerically with geometrical and statistical arguments [16, 17]. Therefore, in the dilute solution limit, the partition coefficients K_i ($i=s$, d) of thin rod-like DNA of length L in both shallow and deep regions are calculated as

$$K_i = 1 - \frac{1+\rho_i}{2\rho_i}\beta_i + \frac{2\beta_i^2}{3\pi\rho_i} \qquad (\beta_i \le 1)$$

$$K_i = \frac{1}{2\beta_i} - \frac{\beta_i}{2\rho_i} + \frac{2\beta_i^2}{3\pi\rho_i} + \frac{\beta_i}{\pi\rho_i}\arccos\frac{1}{\beta_i} - \frac{1}{3\pi\rho_i}(\beta_i^2 - 1)^{1/2}(2\beta_i + \frac{1}{\beta_i}) \quad (1 \le \beta_i \le \rho_i) \qquad (4.16)$$

where $\beta_i = L/d_i$ (scaled molecular length) and $\rho_i = w/d_i$ (scaled nanofilter width). For the DNA lengths tested (with contour length l_c and persistence length l_p), L can be safely treated as equal to the DNA's mean end-to-end distance $<R^2>^{1/2}$ calculated from the worm-like chain model (the Kratky-Porod model, see **Chapter 2**)

$$L = <R^2>^{1/2} = \left\{ 2 l_c l_p [1 - \frac{l_p}{l_c}\{1 - \exp(-\frac{l_c}{l_p})\}] \right\}^{1/2} \qquad (4.17)$$

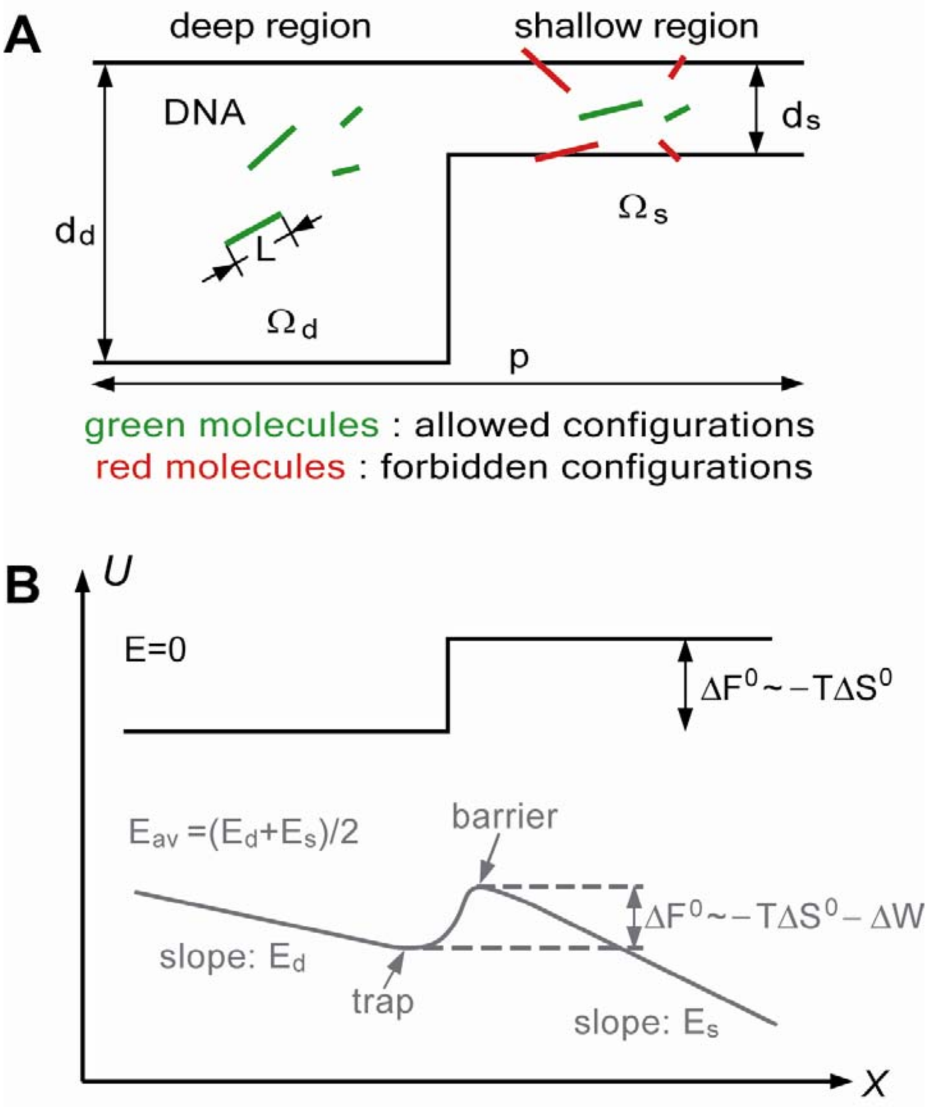

Figure. 4.2: Partitioning of rigid, rod-like DNA across a nanofilter. (**A**) Schematics. (**B**) Free energy landscapes experienced by DNA while crossing a nanofilter (black curve: E=0, grey curve: E_{av}>0). E_s, E_d: electric fields in shallow and deep regions, respectively. E_{av}: average electric field over the nanofilter. DNA preserves the free draining property in the shallow and deep region, resulting in the slopes for both regions proportional solely to the local electric field.

The motion of DNA through the nanofilter array can be described as a biased thermally activated process overcoming periodically modulated free energy barriers ΔF^0 (**Fig. 4.2A**). The free energy landscape U tilted by the electric field E_{av} contains local maxima (barriers) and minima (traps), similar to a double well potential for the Kramers problem (**Fig. 4.1**). As we proved experimentally in **Chapter 3**, the DNA molecules can preserve the free draining property in both the nanofilter shallow regions and deep regions. This property resulted in the free energy slopes for both the nanofilter shallow and deep regions proportional solely to the local electric field (**Fig. 4.2B**).

We define τ_{travel} as the DNA drift time between two consecutive trapping events, so $\tau_{travel}=p/\mu_{max}E_{av}$. Here p is the nanofilter pitch number, and μ_{max} is the maximum sieving free mobility inside the nanofilter array and $\mu_{max}=4d_sd_d\mu_0/(d_s+d_d)^2$ [21], where μ_0 is the DNA free solution mobility inside the nanofluidic channel. After DNA reaches a trap, it is trapped for a certain lifetime τ_{trap} before it enters the nanofilter constriction. The relative mobility $\mu*$ therefore can be written as [9]

$$\mu^* = \frac{\mu}{\mu_{\max}} = \frac{\tau_{travel}}{\tau_{travel} + \tau_{trap}} \qquad (4.18)$$

Two energy terms are included in the barrier ΔF^0 expression ($\Delta F^0 = -T\Delta S^0 - \Delta W$) (**Fig. 4.2B**). The positive $-T\Delta S^0$ term accounts for the entropic energy increase for DNA entering a confining nanofilter constriction. The ΔW term accounts for the electrical potential energy drop in the translation of DNA over the nanofilter barrier along the field direction. Approximately, the electrical potential energy drop ΔW can be expressed as $\Delta W=NqE_{av}d_d$ (N: DNA bp number, q: effective charge per bp derived from μ_0). Since the characteristic diffusion length estimated from the *Peclet* number is always greater than the nanofilter deep region depth d_d. Therefore, the nanofilter transition region radius is approximately equal to d_d, which leads to $\Delta W=NqE_{av}d_d$.

The applied electric field E_{av} effectively lowers the energy barrier in the field direction. When $E_{av}\rightarrow 0$, $|T\Delta S^0/\Delta W|\gg 1$, the entropic energy dominates. This regime provides the greatest size selectivity, but the separation speed and thus efficiency are severely reduced. When $|T\Delta S^0/\Delta W|\ll 1$, the trapping effect becomes negligible and no separation should be expected. The optimized separation performance is expected when $|T\Delta S^0/\Delta W|\sim 1$. Since ΔF^0 in this regime is comparable to or larger than k_BT, k_{esc}, the escape transition rate for DNA to surmount the barrier, as well as the mean trapping time τ_{trap}, can be obtained from Eq. (4.15) for the overdamped regime

$$k_{esc}^{-1} \sim \tau_{trap} \sim \frac{\eta}{E_s E_d} \cdot \exp(-\Delta F^0 / k_B T) \tag{4.19}$$

where η is the DNA friction constant. From the Rouse chain model, the DNA friction constant can be treated to be linearly proportional to DNA length, therefore $\eta\sim N$. Since $E_s = E_{av} \cdot \frac{2d_d}{d_d + d_s}$ and $E_d = E_{av} \cdot \frac{2d_s}{d_d + d_s}$ [9], we can easily conclude E_s, $E_d\sim E_{av}$. Based on the calculation of ΔF^0 depicted in **Fig. 4.2B**, τ_{trap} can be calculated as

$$\tau_{trap} = \frac{\alpha N}{E_{av}^2 K} \exp(-\varepsilon) \tag{4.20}$$

where α is a proportional constant and ε is the reduced electric field ($\varepsilon=\Delta W/k_BT$). By combining Eqs. (4.18) and (4.20), we obtain the expression for the DNA relative mobility μ^* through the nanofilter array as

$$\mu^* = \frac{\mu}{\mu_{\max}} = \left[1 + \frac{\alpha N \mu_{\max}}{pKE_{av}} \exp(-\varepsilon)\right]^{-1} \tag{4.21}$$

It is worthy to emphasize that the theoretical model developed above is applicable to molecules of shapes in addition to rods (for example, globular proteins in their native states or flexible linear ssDNA), even though in this work we studied small rod-like dsDNA as probe molecules to investigate the Ogston sieving process in the nanofilter array. The equations derived above (Eq. (4.18-4.21)) are applicable to other biomolecules and therefore offer general design guidelines for further separation performance improvement for the nanofilter array. For molecules of more complex shapes, analytical solutions to the partition coefficients K_i ($i=s$, d) are not readily available, however solutions may be available using numerical methods [17].

Here we also like to emphasis that the nanofilter shallow and deep region length should have no effect on the trapping of DNA molecules at the nanofilter constriction entrance. The free energy barrier exists right at the boundary between the nanofilter shallow and deep regions, and this energy barrier is due to the limited configuration space of DNA starting right from the nanofilter entrance. We can estimate the effect of the converging electric field on the translational and rotational freedom of DNA when approaching the nanofilter constriction entrance by calculating the reduced electric field ε that compares the electrical potential energy drop ΔW in the transition region with the thermal energy k_BT ($\varepsilon \sim NqE_{av}d_d/k_BT$). In all the experiments we conducted, the values of ε are around 0.1 or less. These small values of ε validate our statement of the near-equilibrium state and ensure the translational and rotational freedom of DNA intact when approaching the nanofilter slit entrance. The limited translational and rotational freedom of DNA inside the nanofilter is also ensured since the DNA translocation time through the whole nanofilter shallow region ($\sim\tau_{travel}=p/\mu_{max}E_{av}$, ranging from 10 ms to 1 sec) is much longer than the DNA lateral diffusion time across the depth of the nanofilter shallow region ($\sim d_s^2/D_{diff}$, ranging from 0.01 μs to 0.1 μs). Therefore, DNA can sample every possible configuration with the Boltzmann probability before exiting the nanofilter.

4.4 Length- and field-dependence of DNA mobility

The DNA mobility μ was determined by measuring an ensemble-averaged band migration time T_{travel} over thousands of nanofilters under various electric fields E_{av} (**Fig. 4.3A**). We have used Gaussian functions (red) for fitting to determine T_{travel}. The mobility μ can be calculated from T_{travel} as $\mu = n_{trap}p/(T_{travel}E_{av})$, where n_{trap} is the total number of nanofilters of the array, and p is the nanofilter pitch number. The maximum sieving free mobility μ_{max} in the nanofilter array is obtained by linearly extrapolating the mobility data μ to zero DNA length under various electric fields E_{av}. The maximum sieving free mobility μ_{max} shows little variance and is practically independent of E_{av}. From μ_{max}, we can further determine the value of the free draining mobility μ_0 in the nanofilter array as $\mu_0 = (d_s + d_d)^2 \mu_{max}/(4 d_s d_d)$. The value of the free draining mobility μ_0 is useful to extract the value of the DNA effective charge per base pair q.

The experimental data of μ^* and τ_{trap} for 100-bp DNA ladder (**Fig. 4.3**) and low molecular weight DNA ladder (**Fig. 4.4**) agree very well with the theoretical curves calculated from Eqs. (4.20) & (4.21), especially in the regime of low field (E_{av}<30 V/cm) and short DNA. The best fitting constant α was found fairly constant for all the electric fields E_{av}, which gives us additional confidence about the validity of the kinetic model.

As discussed, the near-equilibrium state of DNA crossing a nanofilter can be estimated with the reduced electric field ε. When E_{av}<30 V/cm, ε is less than 0.1 for DNA of one persistence length. The small ε values associated with low fields validate our near-equilibrium kinetic model, and further suggest the trivial role of the exponential term $exp(-\varepsilon)$ in Eqs. (4.20) & (4.21) for fitting the experimental data in the low field regime. The factor of $N/(E_{av}^2 K)$ is explicitly derived from both the equilibrium partitioning theory (K) and the double well potential (N/E_{av}^2), and clearly serves as the determinant for the fitting. The $exp(-\varepsilon)$ term only plays a role as E_{av} increases and thus ΔW becomes more comparable to the entropic barrier.

From the kinetic model, the intrinsic size selectivity of the nanofilter array $d\mu^*/dN(N\to 0)$ is calculated as $d\mu^*/dN(N\to 0)\sim-(pE_{av})^{-1}$. Therefore reduced nanofilter pitch number p and reduced electric field E_{av} both decreases the size non-differentiating DNA drift time τ_{travel} and further reduced E_{av} maximizes the entropic barriers height. All the effects accentuate the size-differentiating barrier surmounting process and lead to greater size selectivity. Our kinetic model also implicitly defines a critical field ε_c above which the electric force overcomes the entropic force ($\Delta W > -T\Delta S^0$). By combining Eq. (4.16) and the expression of ΔW, we calculated ε_c in the short DNA limit to be independent of N and $\varepsilon_c \sim d_s^{-1}$, where d_s accounts for the nanofilter sieving property.

The derivative of relative mobility μ^* with respect to DNA size N, $d\mu^*/dN$, is a useful measure of the size selectivity of the nanofilter array for a particular DNA size range. From Eq. (4.21), we obtain

$$\frac{d\mu^*}{dN} = \frac{\alpha p E_{av} \mu_{\max} (\frac{dK}{dN} \cdot N - K)}{(pKE_{av} + \alpha N \mu_{\max})^2} \tag{4.22}$$

where we have neglected the local electric field lowering the energy barrier height ΔW at the entropic barrier, since ΔW is insignificant compared to thermal energy ($k_B T$). For short DNA with the scaled molecular length $\beta_s \le 1$ (the DNA contour length is less than the nanofilter shallow region depth), $\frac{dK}{dN} \cdot N - K \approx -1$. Additionally, under experimental conditions where drift time τ_{travel} dominates mean trapping time τ_{trap} ($pKE_{av} >> N\mu_{max}$), Eqs. (4.21) and (4.22) can be further simplified to $\mu^* = 1 - \alpha N \mu_{max}/(pKE_{av})$ and $d\mu^*/dN \sim -(pK^2E_{av})^{-1}$, respectively.

The most important index of success for the analytical separation of two specific components is the resolution R_s. The nanofilter array is essentially an elution system, and therefore the resolution R_s between two bands corresponding to monodisperse DNA samples of close bp numbers of $N - n$ and $N + n$ (with $n << N$) is

$$R_{s(N-n,N+n)} \sim \frac{\partial T_{travel}}{\partial N} \cdot \frac{n}{\tau_{1/2,N}} \tag{4.23}$$

where T_{travel} is the size-dependent DNA migration time through the whole nanofilter array and $\tau_{1/2,N}$ represents the standard deviation of a Gaussian peak in time units. The migration time T_{travel} can be written as $T_{travel} \sim n_{trap} p / (E_{av} \mu_{\max} \mu^*)$. Bow *et al.* has developed an analytical model to calculate band dispersion in the Ogston sieving regime through the nanofilter array, which was loosely based on the macrotransport theory [22]. In the kinetic model, the effective dispersion coefficient D^* of short DNA fragments has been calculated to be approximated as $D^* \sim pE_{av}\mu_{\max}\mu^*$. Therefore, the standard deviation $\tau_{1/2,N}$ of a Gaussian peak under a particular separation condition can be calculated as

$$\tau_{1/2,N} \sim n_{trap}^{1/2} p / (E_{av} \mu_{\max} \mu^*) \tag{4.24}$$

Combining Eqs. (4.23) and (4.24) for the limit of $\tau_{\text{travel}} >> \tau_{\text{trap}}$ ($pKE_{av} >> N\mu_{max}$), we obtain the expression for separation resolution as

$$R_{s(N-n,N+n)} \sim \frac{n_{trap}^{1/2}\mu_{\max}}{pE_{av}} \cdot \frac{n}{K^2} \tag{4.25}$$

From Eq. (4.25), it is clear that reducing the nanofilter pitch number p should greatly improve the separation performance of the one-dimensional nanofilter array, since R_s is inversely proportional to p, and reducing p can also effectively increase the number of nanofilters per unit separation length (n_{trap}). Our theory here is consistent with our experimental observations in Chapter 3.

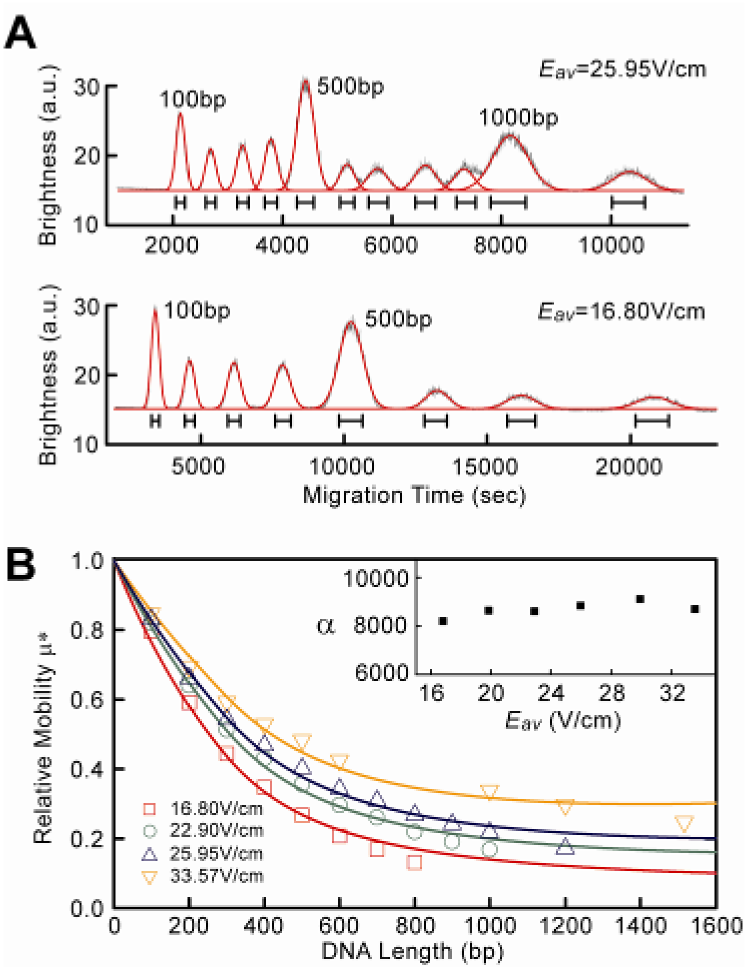

Figure 4.3: 100 bp DNA ladder separated in a nanofilter array (d_s=80 nm, d_d=580 nm, and p=4 µm). (**A**) Electropherograms (grey) were taken 1 cm from the injection point. Gaussian functions (red) were used for fitting and the black bars label the peak widths (±s.d.). (**B**) Relative mobility μ^* of 100-bp DNA ladder with solid fitting curves. The ±s.d. of μ^* derived from the half peak width are all less than 4%, so statistical error bars for μ^* are not plotted. The inset shows the best fitting constant α for different field strengths. α has a mean about 8684 and a ±s.d. about 3%. All the fitting curves in (**B**) are calculated with $q=2.49\times10^{-21}$ J/V·bp, l_p=53 nm, and $l_c=0.36\cdot N$ nm.

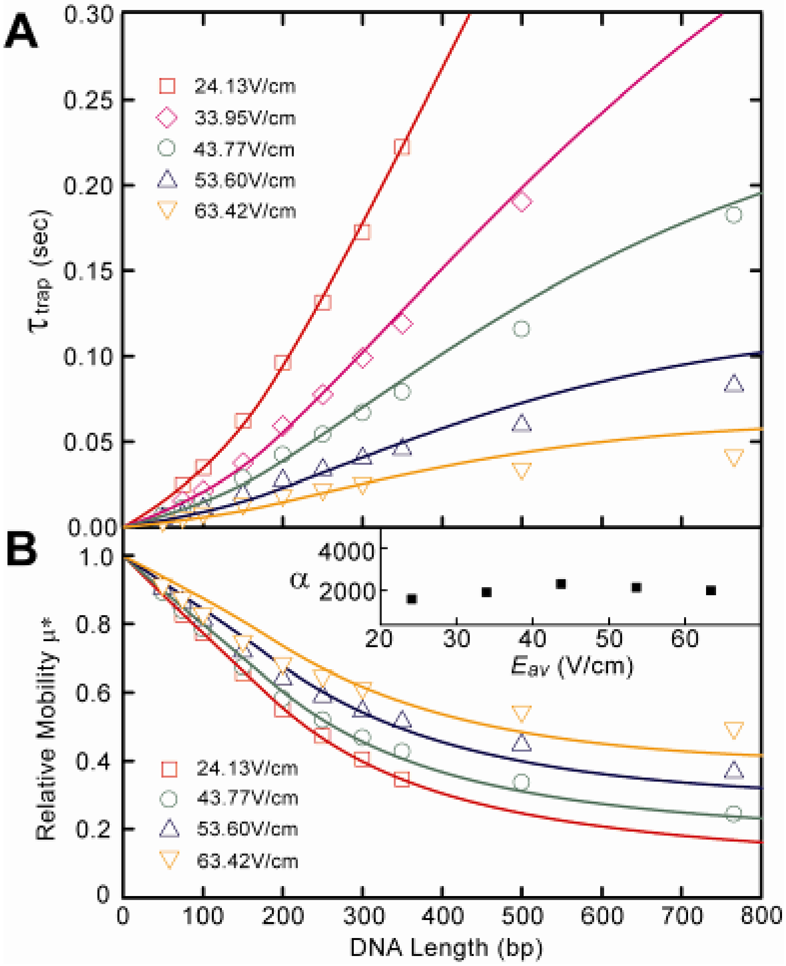

Figure 4.4: Mean trapping time τ_{trap} (**A**) and relative mobility μ^* (**B**) with the best fitting curves. τ_{trap} and μ^* were measured for low molecular weight DNA ladder in a nanofilter array with d_s=55 nm, d_d=300 nm, and p=1 µm. Separation length was 5 mm and $\tau_{trap}=T_{travel}/5000-\tau_{travel}$. The ±s.d. of μ^* are all less than 6%, so statistical error bars for μ^* are not plotted. The inset shows α with a mean about 1990 and a ±s.d. about 13%. All the fitting curves are calculated with $q=2.49\times10^{-21}$ J/V·bp, l_p=53 nm, and $l_c=0.36\cdot N$ nm.

4.5 Crossover from Ogston sieving to entropic trapping

The experimental data in **Fig. 4.3** and **Fig. 4.4** deviated slightly from the theoretical curves as the DNA length increases to several persistence lengths. This is expected since for long DNA, other degrees of entropic freedom, such as internal conformation, become non-negligible in the kinetics of crossing the nanofilter barriers. The (conformational) entropic trapping mechanism was used to explain separation of long DNA (>5 kilobase pairs (kbp)) in similar intervening entropic barriers where longer DNA were found to advance faster than shorter ones because of their greater hernia nucleation possibility [19]. We demonstrate the crossover from Ogston sieving to entropic trapping by measuring mobility of DNA of a size ranging from 0.5-8 kbp in a 73 nm nanofilter array. The radius of gyration R_g of these DNA, estimated from the worm-like chain model, span a range of 40 nm to 220 nm, covering the region around R_g/d_s~1. **Figure 4.5** clearly shows two distinct sieving regimes as evidenced by the valleys existing on the mobility curves. The left side of the valley is Ogston sieving, and the mobility μ decreases as DNA length increases. The right side shows evidence of entropic trapping, and the mobility μ increases with DNA length.

The transition points from Ogston sieving to entropic trapping under different electric fields E_{av} were all at about DNA of 1.5 kbp, where R_g(1.5 kbp)~80 nm, comparable to d_s=73 nm. This observation supports the intuitive physical picture that the transition regime between Ogston sieving and entropic trapping is around R_g/d_s~1. The electric field E_{av} shows different effects on the trapping in the two regimes: in Ogston sieving, the higher entropic barrier height associated with lower E_{av} leads to greater size selectivity (as seen with the steeper mobility curves); as in entropic trapping, nanofilter shows little size selectivity at low E_{av}, but mobility curves become steeper as E_{av} increases. All the mobility curves reach a plateau as DNA length becomes larger than about 5 kbp. The complex field effect pattern near the transition regime cannot be explained by the simple kinetic model proposed in Ref. [19], and further more detailed characterization needs to be conducted.

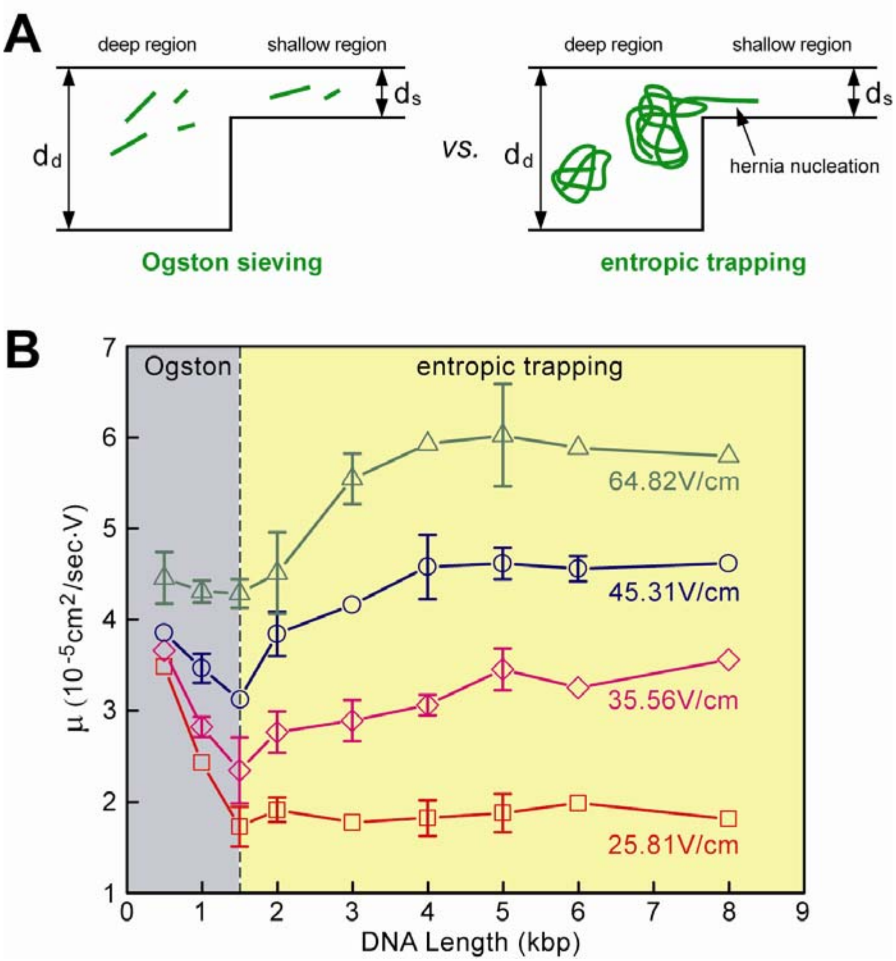

Figure 4.5: Transition from Ogston sieving to entropic trapping. (**A**) Schematic of Ogston sieving and entropic trapping. (**B**) Mobility μ as a function of DNA length. DNA fragments were extracted after agarose gel separation. The nanofilter array has d_s=73 nm, d_d=325 nm, p=1 μm. The relative large statistical error bars (drawn if larger than the symbol) is likely due to the low DNA concentrations. The grey and yellow areas indicate Ogston sieving and entropic trapping, respectively. The transition points are marked with the vertical dashed line drawn for DNA length=1.5-kbp.

4.6 References

1. Ogston, A. G. The spaces in a uniform random suspension of fibres. *Trans. Faraday Soc.* **54**, 1754–1757 (1958).
2. Rodbard, D. & Chrambach, A. Unified theory for gel electrophoresis and gel filtration. *Proc. Natl. Acad. Sci. U. S. A.* **65**, 970–977 (1970).
3. Tietz, D. Evaluation of mobility data obtained from gel electrophoresis: strategies in the computation of particle and gel properties on the basis of the extended Ogston model. *Advances in Electrophoresis* (VCH Publishers, New York, 1988), Vol. 2, 109–169.
4. Kozulic, B. Models of gel electrophoresis. *Anal. Biochem.* **231**, 1–12 (1995).
5. Slater, G. W., Mayer, P. & Drouin, G. Migration of DNA through gels. *Methods Enzymol.* **270**, 272–295 (1996).
6. Viovy, J.-L. Electrophoresis of DNA and other polyelectrolytes: physical mechanisms. *Rev. Mod. Phys.* **72**, 813–872 (2000).
7. Bakajin, O. B. *et al*. Electrohydrodynamic stretching of DNA in confined environments. *Phys. Rev. Lett.* **80**, 2737–2740 (1998).
8. Tegenfeldt, J. O. *et al*. The dynamics of genomic-length DNA molecules in 100-nm channels. *Proc. Natl. Acad. Sci. U. S. A.* **101**, 10979–10983 (2004).
9. Han, J. & Craighead, H. G. Characterization and optimization of an entropic trap for DNA separation. *Anal. Chem.* **74**, 394–401 (2002).
10. Tessier, F., Labrie, J. & Slater G. W. Electrophoretic separation of long polyelectrolytes in submolecular-size constrictions: a Monte Carlo study. Macromolecules **35**, 4791–4800 (2002).
11. Fu, J., Mao, P. & Han, J. Nanofilter array chip for fast gel-free biomolecule separation. *Appl. Phys. Lett.* **87**, art. no. 263902 (2005).
12. Gardiner, C. W. *Handbook of Stochastic Methods for Physics, Chemistry and the Natural Sciences* (second edition, Springer-Verlag, Berlin, 1985).
13. Risken, H. *The Fokker-Planck Equation* (Springer-Verlag, Berlin, 1996).
14. Brinkman, H. C. Brownian motion in a field of force and the diffusion theory of chemical reactions. II. *Physica* **7**, 149–155 (1956).
15. Stockmayer, W. H. Dynamics of chain molecules. *Molecular Fluids*, eds. R. Balian and G. Weill (Gordon & Breach, London, 1976).
16. Giddings, J. C., Kucera, E., Russell, C. P. & Myers, M. N. Statistical theory for the equilibrium distribution of rigid molecules in inert porous networks. Exclusion chromatography. *J. Phys. Chem.* **72**, 4397–4408 (1968).
17. Deen, W. M. Hindered transport of large molecules in liquid-filled pores. *AIChE J.* **33**, 1409–1425 (1987).
18. Fu, J., Yoo, J. & Han, J. Molecular sieving in periodic free-energy landscapes created by patterned nanofilter arrays. *Phys. Rev. Lett.* **97**, art. no. 018103 (2006).
19. Han, J., Turner, S. W. & Craighead, H. G. Entropic trapping and escape of long DNA molecules at submicron size constriction. *Phys. Rev. Lett.* **83**, 1688–1691 (1999).
20. Nykypanchuk, D., Strey, H. H. & Hoagland, D. A. Brownian motion of DNA confined within a two-dimensional array. *Science* **297**, 987–990 (2002).

21. Streek, M., Schmid, F., Duong, T. T. & Ros, A. Mechanisms of DNA separation in entropic trap arrays: a Brownian dynamics simulation. *J. Biotechnol.* **112**, 79─89 (2004).
22. Bow, H. Characterization of nanofilter array for small molecule separation. Master Thesis, Electrical Engineering, MIT (2006).

Chapter 5

A patterned anisotropic nanofilter array for continuous-flow separation of DNA and proteins

In this chapter, we introduce a microfabricated anisotropic sieving structure consisting of a two-dimensional periodic nanofilter array (an anisotropic nanofilter array, ANA) [1-3]. The designed structural anisotropy in the ANA causes different-sized biomolecules to follow distinct migration trajectories, leading to efficient separation. Continuous-flow Ogston sieving-based separation of short DNA and proteins as well as entropic trapping-based separation of long DNA were achieved within a few minutes, thus demonstrating the potential of the ANA as a generic molecular sieving structure for an integrated biomolecule sample preparation and analysis system.

5.1 Introduction: continuous-flow bioseparation for sample preparation

In the previous chapters, we have demonstrated that the nanofilters can be used as controllable molecular sieving structures for rapid analytical separation of various physiologically-relevant macromolecules, such as DNA and proteins. We have successfully demonstrated the Ogston sieving mechanism to separate biomolecules with diameters smaller than the size of the nanofilter constriction. The configurational entropic energy barrier at the nanofilter threshold causes different-sized biomolecules to jump across the nanofilter constriction with different probabilities (or speeds), leading to efficient size-based separation. In this chapter, we will extend the nanofluidic sieving structure design paradigm to implement a widely applicable anisotropic sieving structure for continuous-flow separation of biomolecules covering very broad biological size scales. More specifically, we will design and fabricate a nanofilter-based two-dimensional anisotropic sieving structure that is suitable for continuous-flow separation of dsDNA molecules and proteins. Such continuous-flow separation has promising implications for on-chip based sample preparation for different biological and biomedical applications.

There are four highly-desirable benefits associated with continuous-flow preparative separation (spatial separation) when compared with one-dimensional analytical separation (temporal separation):

1) Increased sample throughput ideal for sample preparation based on micro/nanosystems. Most micro/nanofluidic systems can only process low quantities of samples due to their small handle volumes. The continuous-flow operation can remove the limitation of the amount of sample the device can analyze, and the fractionated biomolecules can be continuously collected and therefore accumulate over time.
2) Fractionated biomolecule streams can be easily collected for downstream analysis or subsequent manipulation. By virtue of the continuous flow operation, the fractionated biomolecule streams can be easily recovered or routed to different downstream reaction chambers or detection channels for further analysis.

Therefore, the continuous-flow separation scheme is ideal for a highly integrated microanalysis system that includes multiple analytical steps and separation channels and reaction chambers.

3) Continuous-flow separation permits continuous harvesting of the subset of biomolecules of interest to enhance the specificity and sensitivity for downstream biosensing and detection, whish is highly desirable for integrated bioanalysis microsystems. Operation in continuous flow can enable the integration of the signal over time or to collect the sample over time, thus decreasing the downstream detection limit (or enhancing downstream detection sensitivity). This advantage may prove useful for preparative separation of complex biological samples (such as human blood serum), which has promising implications for proteomic research and biomarker discovery.

4) In one-dimensional analytical separation systems, separation speed and resolution are normally controlled and mediated by a single force field applied along the direction of the separation column (for example, electrostatic force field for capillary electrophoresis systems and hydrodynamic force field for high performance liquid chromatography systems (HPLC)). Therefore, the separation speed and resolution in one-dimensional separation systems are coupled with each other and can often complicate the optimization process of the separation system. The one-dimensional nanofilter array demonstrated in the previous chapters is a clear example for such a complication. In the one-dimensional nanofilter array, the separation speed and resolution cannot both be enhanced without compromising one another. While in continuous-flow preparative separation

systems, the separation speed and resolution are decoupled in two orthogonal directions, and are modulated, respectively, by two independent orthogonal force fields. Therefore, careful regulation of both the force fields in the two orthogonal directions can help achieve rapid separation with concurrent high resolution.

5.2 Anisotropic sieving structure: a new paradigm for continuous-flow bioseparation

Continuous-flow separation is highly desirable as we discussed in the previous section. However, in conventional biomolecule separation systems that use a random isotropic sieving medium in their separation channels and chambers (such as gel, liquid gel or ampholytes), continuous-flow separation is not readily possible. **Figure 5A** shows an example of an isotropic sieving medium that contains a two-dimensional random gel. Upon application of two uniform orthogonal electric fields E_x and E_y in the gel, two different-sized biomolecules can be continuously injected into the gel and form straight molecular steams. Due to the sieving property of the gel, the mobility of two different-sized biomolecules can be different (here we simply assume the smaller *red* molecule and larger *green* molecule have mobility of μ_1 and μ_2, respectively, and $\mu_1>\mu_2$). The stream deflection angle θ in a two-dimensional sieving medium can be calculated using a simple expression

$$\tan\theta = V_x / V_y = (\mu_x / \mu_y)\cdot(E_x / E_y) \tag{5.1}$$

where V_x and V_y are the migration velocities along the *x*- and *y*-axis, respectively, and μ_x and μ_y are the two orthogonal mobility along the *x*- and *y*-axis, respectively. In an isotropic sieving medium, the mobility is isotropic in nature, thus, in Eq. (5.1), μ_x and μ_y simply cancel out, and the expression of the stream deflection angle θ becomes $\tan\theta = E_x / E_y$. Therefore, in an isotropic sieving medium, the stream defection angle θ is solely determined by the two electric fields E_x and E_y, and different-sized biomolecules will follow the same trajectory without separation (**Fig. 5.1A**). Here we need to point out that the mobility μ in the two-dimensional gel is still size-dependent, therefore, the migration speeds of the two different-sized biomolecules will be different.

The structural anisotropy in an anisotropic sieving medium can cause molecules of different properties (for example, size, charge, and hydrophobicity) to follow different migration trajectories, leading to efficient separation. In an anisotropic medium (**Fig. 5.1B**), the function of μ_x / μ_y in Eq. (5.1) becomes more complex, and could be a function of both the structural anisotropy of the sieve and molecular properties. Therefore, the expression of the stream deflection angle θ can be modified based on Eq. (5.1) as

$$\begin{aligned}\tan\theta = V_x / V_y &= (\mu_x / \mu_y)\cdot(E_x / E_y) \\ &= \text{func(size,charge,etc.)}\cdot(E_x / E_y)\end{aligned} \qquad (5.2)$$

Thus, molecules of different properties will follow different trajectories in the anisotropic sieving medium, if such properties cause the values of the function *func*(size, charge, etc.) to be dependent on molecular properties. In **Fig. 5.1B**, we assume the mobility along the *y*-axis μ_y is size-independent, and the mobility along the *x*-axis μ_x is size-dependent. Therefore, in **Fig. 5.1B**, smaller *Red* molecule will display a larger deflection angle θ than the larger *Green* one. The unknown function *func*(size, charge, etc.) could be difficult to determine, especially when the function of μ_x / μ_y is associated with both molecular properties and the structural anisotropy of the sieve.

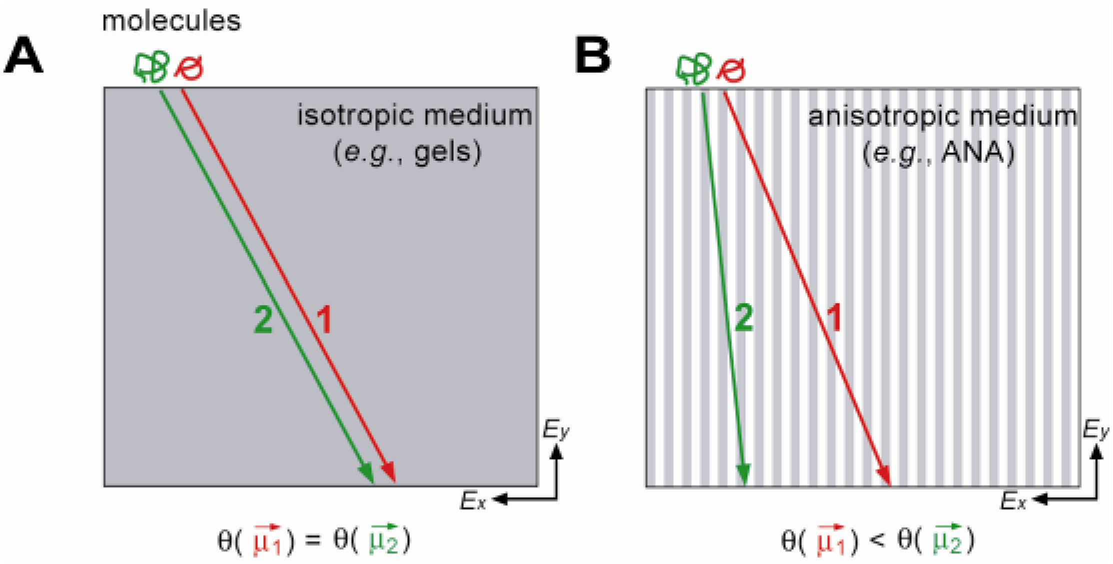

Figure 5.1: Continuous-flow separation of different-sized biomolecules (large biomolecule in *Green*, small biomolecule in *Red*) in two-dimensional isotropic (**A**) and anisotropic (**B**) sieving media. For continuous-flow separation, the vectorial direction of the mobility $\vec{\mu}$ determines the trajectory (and separation), and the absolute magnitude of $\vec{\mu}$ determines the migration speed. (**A**) No separation can be achieved in an isotropic sieving medium. Different-sized biomolecules follow the same trajectory that is solely determined by the two independent orthogonal electric fields E_x and E_y. (**B**) In an anisotropic sieving medium, different-sized biomolecules follow different trajectories that are determined by both the electric fields as well as by certain molecular properties (for example, size). The stream deflection angle θ is defined with respect to the y-axis.

5.3 A patterned anisotropic nanofilter array (ANA): device design and fabrication

In this section, we will introduce a unique molecular sieving structure design, called the anisotropic nanofilter array (anisotropic nanofilter array, ANA), and its implementation for continuous-flow separation of DNA and proteins based on size. The designed structural anisotropy of the ANA is critical to continuous-flow separation, which is not readily possible with a random isotropic sieving medium. Moreover, the ANA allows for various sieving mechanisms (*e.g.*, Ogston sieving and entropic trapping) to take effect in the separation of biomolecules in very broad biological size scales.

The design of the ANA consists of a two-dimensional periodic nanofilter array (**Fig. 5.2**). The separation mechanism of the ANA relies on different sieving characteristics along two orthogonal directions within the ANA, which are set perpendicular and parallel to the nanofilter rows (indicated as x- and y-axis, respectively, in **Fig. 5.2**). Upon application of an electric field E_y along the positive y-axis, uniformly negative-charged biomolecules (*e.g.*, dsDNA and proteins) injected into the array assume a drift motion in deep channels with a negative velocity V_y that is size-independent. An orthogonal electric field E_x is superimposed along the negative x-axis across the nanofilters, and this field selectively drives the drifting molecules in the deep channel to jump across the nanofilter in the positive x-direction to the adjacent deep channel. Molecular crossings of the nanofilter under the influence of the electric field E_x can be described as biased, thermally activated jumps across free energy barriers at the nanofilter threshold [4, 5], and these free energy barriers depend on both steric and electrostatic interactions between charged macromolecules and charged nanofilter walls

[6-8]. At high ionic strength where the Debye length λ_D is negligible compared to the nanofilter shallow region depth d_s, electrostatic interactions between charged macromolecules and charged nanofilter walls are largely screened. The free energy barriers are therefore solely determined by the configurational or conformational entropy loss within the constriction due to the steric constraints or exclusion of the nanofilter wall (a purely steric limit) [4-6]. For biomolecules with diameters smaller than the nanofilter constriction (*i.e.*, Ogston sieving) (**Fig. 5.2A**), the entropic energy barrier favors DNA and proteins with a smaller size for passage, resulting in a greater jump passage rate P_x for smaller molecules. Therefore, in Ogston sieving, smaller molecules exercise a shorter mean characteristic drift distance L_d in the deep channels between two consecutive nanofilter crossings, leading to a larger stream deflection angle θ.

For molecules with diameters greater than the nanofilter constriction size, passage requires the molecules to deform and form hernias at the cost of their internal conformational entropy (*i.e.*, entropic trapping) [4, 9, 10]. A previous study on long DNA molecules trapped at a similar nanofluidic constriction showed that the activation free energy barrier for DNA escape depends solely on the inverse of the electric field strength ($\sim 1/E_x$) [4]. Furthermore, longer molecules have a larger surface area contacting the constriction and thus have a greater probability to form hernias that initiate the escape process (in other words, they have a higher escape attempt frequency) (**Fig. 5.2B**) [4, 10]. Therefore, in the entropic trapping regime, longer molecules assume a greater jump passage rate P_x, resulting in a larger deflection angle θ.

Here it is worthy to emphasis that in the ANA, the mean characteristic drift distance L_d between two consecutive nanofilter crossings plays a determinant role for the migration trajectory, and the stream deflection angle θ is directly related to L_d with the expression of $\tan\theta=(l_d+l_s)/L_d$, where l_d and l_s are the deep channel width and nanofilters length, respectively. The mean characteristic drift distance L_d is determined by both the complex structural geometry of the ANA and the two independent orthogonal fields E_x and E_y. We will discuss more on the theoretical modeling of the mean characteristic drift distance L_d and the stream deflection angle θ in the following sections of this chapter.

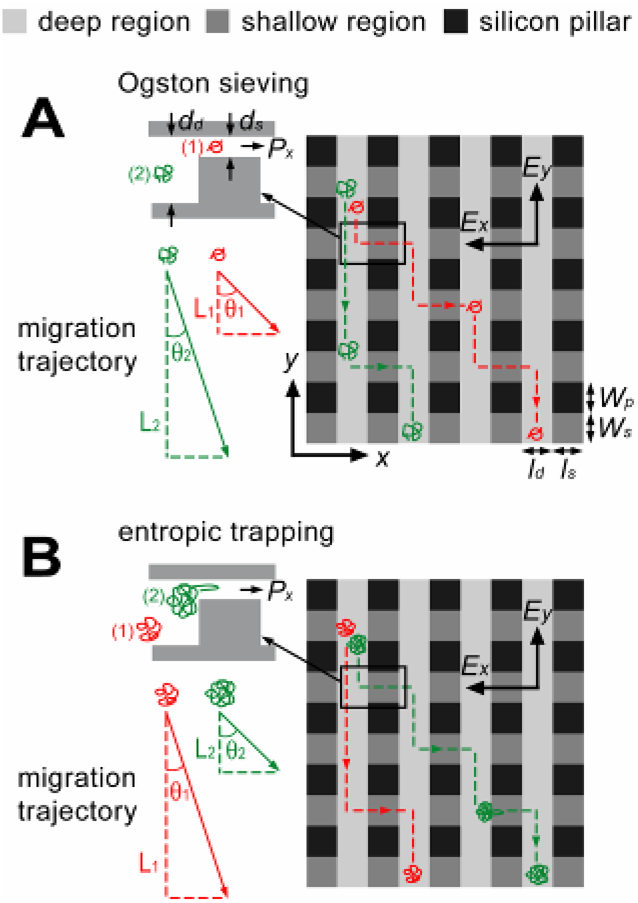

Figure 5.2: Schematic showing negatively charged macromolecules assuming bidirectional motion in the ANA under two orthogonal electric fields E_x and E_y. Dashed lines and arrows indicate migration trajectories projected onto the *x*-*y* plane. Nanofilters (with width of w_s, length of l_s and depth of d_s) arranged in rows are separated by deep channels (with width of l_d and depth of d_d). Rectangular pillars (with width of w_p and length of l_s) between nanofilters serve as supporting structures to prevent collapse of the top ceiling. (**A**) Ogston sieving. Shorter molecules (*red*) are preferred for passage through the nanofilter due to their greater retained configuration freedom, resulting in a greater nanofilter jump passage rate P_x (the inset). The mean drift distance L_d between two consecutive nanofilter crossings plays a determinant role for the migration trajectory, with a shorter L_d leading to a larger stream deflection angle θ that is defined with respect to the negative *y*-axis. (**B**) Entropic trapping. Longer molecules (*green*) have larger surface area contacting the nanofilter threshold (the inset), resulting in a greater probability for hernia formation and thus a greater nanofilter passage rate P_x.

We designed and fabricated a silicon-based microfluidic device that incorporates the ANA as the sieving structure (**Fig. 5.3**). The shallow and deep regions of the ANA, as well as the microfluidic channels were defined and etched into a Si wafer using photolithography and reactive-ion etching techniques. The fabrication process for the ANA device was the same as for the one-dimensional nanofilter array (see Chapter 3). The ANA contains nanofilters with a constriction size of 55 nm (d_s) and a width of 1 μm (w_s). Deep channels separating the nanofilter rows are 1 μm wide (w_d) and 300 nm deep (d_d). The initial biomolecule stream is continuously injected into the deep channels through some injection channels on the top left of the device. Injection channels connecting sample reservoir (1 mm from the ANA top left corner) inject biomolecule samples as a 30 μm wide stream. The fractionated biomolecule streams are collected at intervals along the opposite edge. Microfluidic channels surrounding the ANA connect to fluid reservoirs, where voltages can be applied. The microfluidic channels provide sample loading and collection ports, and further act as electric-current injectors to create uniform electric fields E_x and E_y over the entire ANA structure. For more discussion on the method of using microfluidic channels as boundary electric-current injectors for creating uniform electric fields over sieving structures, please refer to Ref. [11, 12].

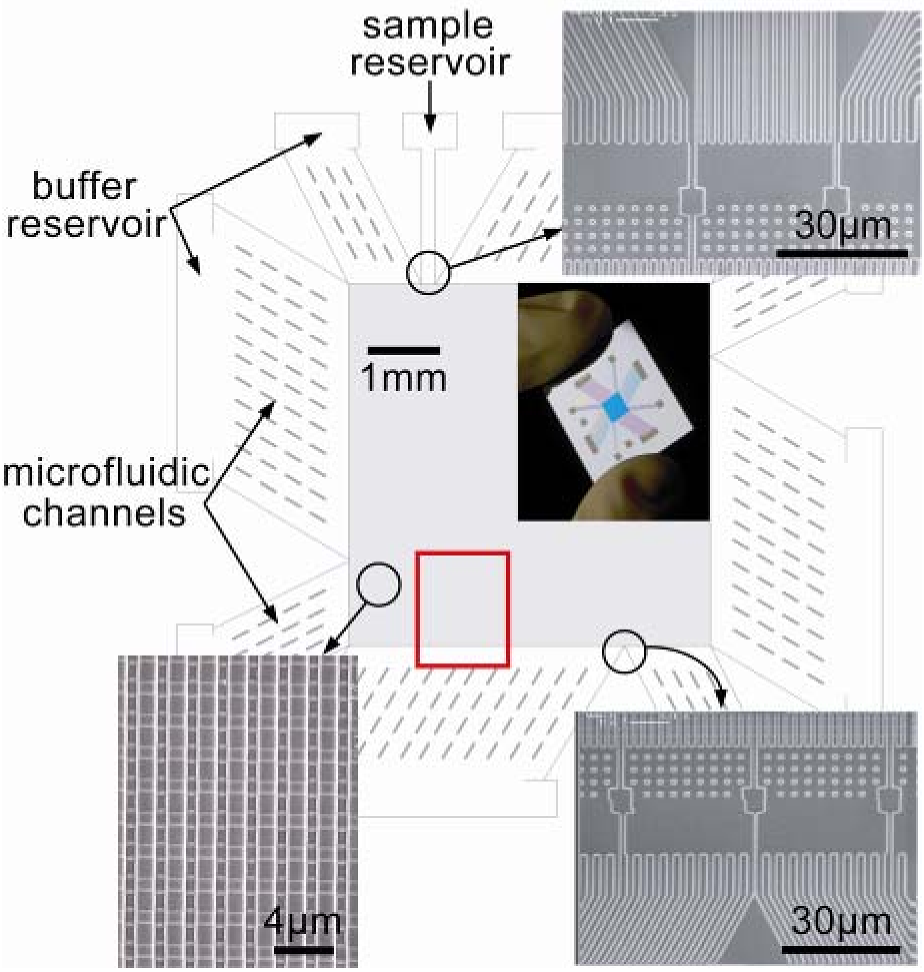

Figure 5.3: Structure of the microfabricated device incorporating the ANA. Scanning electron microscopy images show details of different device regions (clockwise from top right: sample injection channels, sample collection channels, and ANA). The inset shows a photograph of the thumbnail-sized device. The rectangular ANA is 5 mm × 5 mm, and nanofilters (w_s=1 μm, l_s=1 μm and d_s=55 nm) are spaced by 1 μm × 1 μm square-shaped silicon pillars. Deep channels are 1 μm wide (w_d) and 300 nm deep (d_d). Injection channels connecting sample reservoir (1 mm from the ANA top left corner) inject biomolecule samples as a 30 μm wide stream. The red rectangle highlights the area in which fluorescence photographs in **Fig. 5.4** were taken.

5.4 Sample preparation and experimental conditions

To explicitly demonstrate both Ogston sieving and entropic trapping in the ANA, we prepared two different DNA ladder samples covering broad size scales (a low molecular weight DNA ladder: the PCR marker, from 50 bp to 766 bp; a high molecular weight DNA ladder: the λ DNA−Hind III digest, from 2,027 bp to 23,130 bp). The PCR marker and λ DNA−Hind III digest were both labeled with the YOYO-1 in TBE 5× buffer. The dye to DNA base pair ratio was about 1:2 and the final DNA concentration was about 42.18 μg/ml (PCR) and 104 μg/ml (λ DNA−Hind III digest).

We also applied the ANA structure to separate mixtures of proteins under both native and denaturing conditions. The following commercially available proteins and protein-conjugates were investigated: fluorescent B-phycoerythrin (Alexis Biochemicals, San Diego, CA), fluorescein isothiocyanate (FITC) conjugated lectin from *Lens culinaris* (lentil) (Sigma-Aldrich, St. Louis, MO). The final concentration of B-phycoerythrin and lectin were about 0.1–0.2 mg/ml and 0.2–0.4 mg/ml, respectively. For denatured protein experiments, Alexa Fluor 488 conjugated cholera toxin subunit B was purchased from Molecular Probes (degree of labeling: 5 moles dye/mole). *β*-galactosidase from *E. coli* was obtained from Sigma, and was custom labeled with Alexa Fluor 488 by Molecular Probes (degree of labeling: 3 moles dye/mole). The complete denaturation of both proteins was performed by adding SDS and DTT. The SDS-DTT protein mixture contained 2 wt% SDS and 0.1M DDT and was treated in an 85°C water bath for 10 min. The resultant SDS-protein complex solutions were mixed and further diluted in TBE 5× buffer. The final SDS-protein complex sample solution contained 15.1 μg/ml cholera toxin subunit B, 90.9 μg/ml *β*-galactosidase, 0.1 wt% SDS, and 5 μM DTT.

The ANA was filled with TBE 5× buffer before the separation experiments with DNA and proteins. Additional 0.1wt% SDS was added to TBE 5× buffer for the denatured protein experiments. In all experiments, migration of DNA and denatured protein complexes followed the direction of electrophoresis; proteins under native conditions however followed the direction of electroosmosis (presumably due to their lower net charge and therefore less strongly experienced electrophoretic drag).

5.5 Ogston sieving for continuous-flow separation of short DNA

To explicitly demonstrate the steric sieving effect of the ANA, we first injected a low molecular weight DNA ladder sample (the PCR marker) at TBE 5× buffer under a broad range of field conditions (**Fig. 5.4**). Since TBE 5× buffer has an equivalent ionic strength about 130 mM with a corresponding Debye length λ_D of about 0.84 nm [13] (much smaller than the nanofilter shallow region depth d_s, ~55 nm), steric interactions dominate molecular jump dynamics across the nanofilter. The PCR marker contains 5 different DNA fragments of sizes ranging from 50 bp to 766 bp. Since the persistence length of dsDNA is about 50 nm [14], these PCR marker fragments behave as rigid, rod-like molecules with an end-to-end distance of about 16 nm to 150 nm [15]. The entry into the confining nanofilter can only be realized if the rod-like DNA molecules are properly positioned and oriented without overlapping the wall, which limits the configurational freedom and creates an entropic barrier (*i.e.*, Ogston sieving) [5].

Figure 5.4A–F show 6 fluorescence photographs of the PCR marker stream pattern in the ANA when horizontal and vertical fields of different values were applied (all the photographs were taken in the area highlighted by the red rectangle in **Fig. 5.3**).

Figure 5.4A–C shows the PCR marker stream pattern as E_x was raised from 0 V/cm to 60 V/cm at fixed E_y=25 V/cm. In the experiment of **Fig. 5.4A**, only the vertical field E_y=25 V/cm was applied, and the PCR marker sample formed a vertical stream without any separation. The initial stream width W of 30 μm gradually widened to about 50 μm at the end of the ANA after drifting for about 210 sec (less than 4 min). The applied horizontal field E_x quickly deflected DNA fragments according to their molecular weights (size), with the stream deflection angle θ and the stream width W depending on the exact field conditions. Increasing the horizontal field E_x resulted in larger deflection angles as well as wider spreading of the streams, as shown in **Fig. 5.5**. Please note that, for all the fluorescence intensity profiles measured at the bottom of the ANA, we have used Gaussian functions for fitting to determine the means (the maximum intensity) as well as the stream widths.

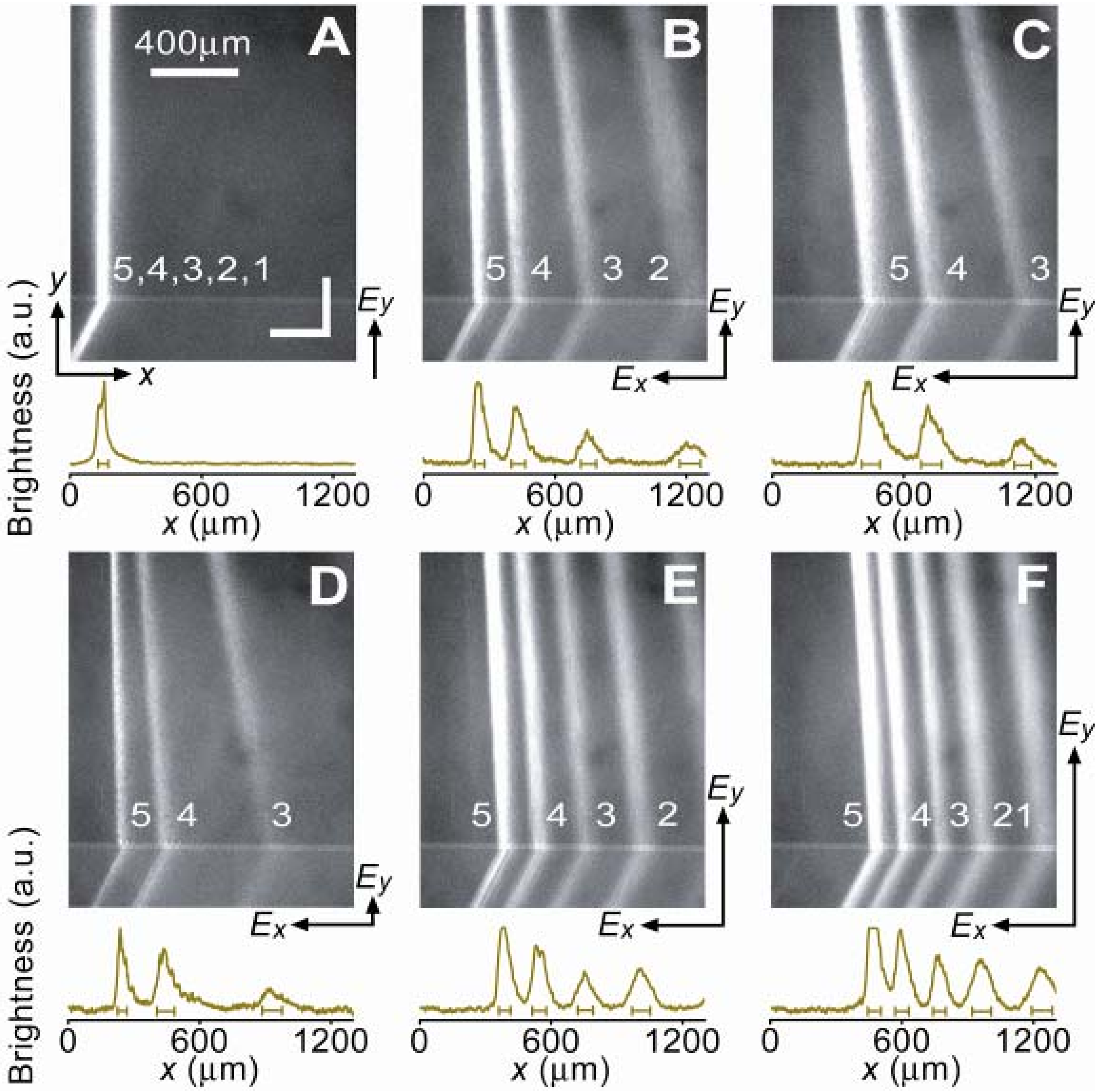

Figure 5.4: Ogston sieving of the PCR marker through the ANA. Fluorescent photographs of the PCR marker stream pattern were taken in the area highlighted by the red rectangle in **Fig. 5.3**. For **A**, only E_y applied and E_y=25 V/cm; for **B**, E_x=35 V/cm, E_y=25 V/cm; for **C**, E_x=60 V/cm, E_y=25 V/cm; for **D**, E_x=35 V/cm, E_y=12.5 V/cm; for **E**, E_x=35 V/cm, E_y=50 V/cm; for **F**, E_x=35 V/cm, E_y=75 V/cm. Band assignment: (1) 50-bp; (2) 150-bp; (3) 300-bp; (4) 500-bp; (5) 766-bp. Fluorescence intensity profiles (of arbitrary units) were measured at the ANA bottom edge. The bars underneath the peaks are centered at the means and label the stream widths (standard deviation, ±s.d.).

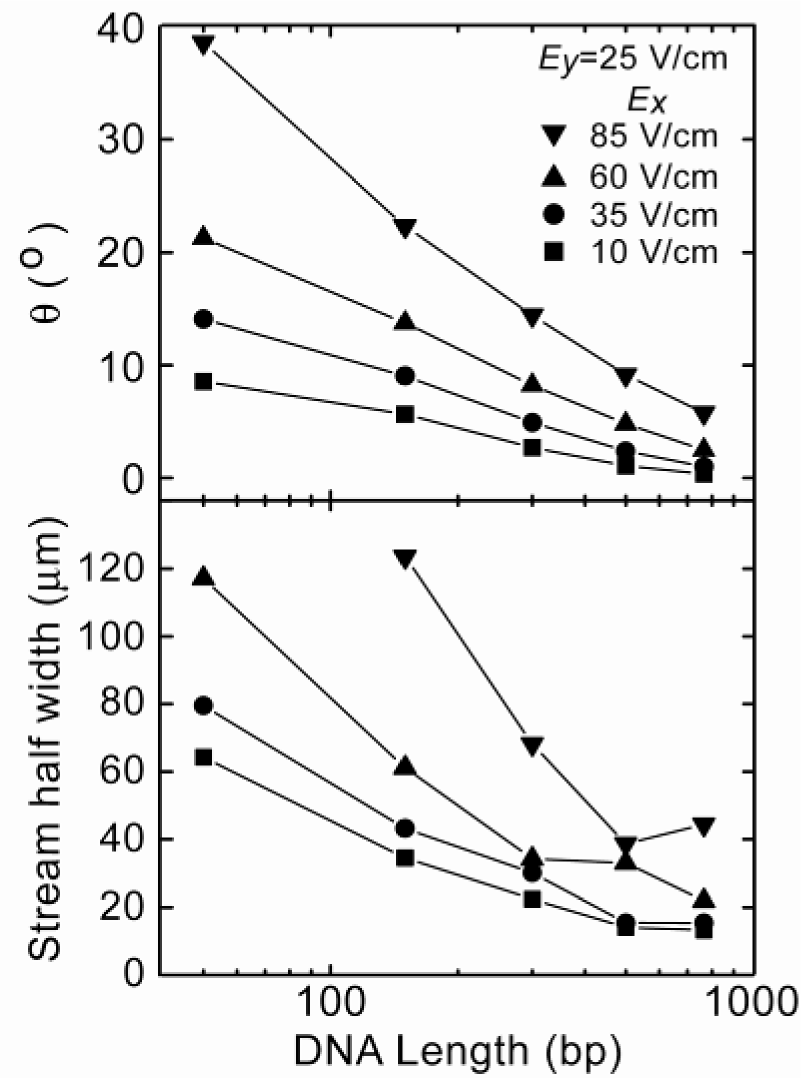

Figure 5.5: Stream deflection angle θ (top) and stream half width ($W/2$, bottom) as a function of DNA length. Data are taken from separation of the PCR maker through the ANA. The ±s.d. of θ derived from the stream half-width are all less than 1°, so statistical error bars for θ are not plotted.

As we have discussed in the previous chapters, in the Ogston sieving regime, the nanofilter jump passage rate P_x for short DNA of a bp number N can be calculated based on the equilibrium partitioning theory and the Kramer's rate theory. In the limit of low horizontal electric field, the nanofilter passage rate P_x is proportional to $E_x^2 K/N$ (see Eq. (4.19)), where K is the DNA equilibrium partitioning coefficient across the nanofilter. Therefore, increasing E_x enhances the jump passage rate P_x, leading to a shorter mean drift distance L_d and thus a larger deflection angle θ. Based on the calculation of P_x, we can construct a course-grained kinetic model to explain the field-dependent stream deflection angle θ. More details about the kinetic model will be presented in the following section.

For Ogston sieving, the stream widening in the ANA can be largely attributed to two factors: intrinsic diffusion and convective dispersion. Intrinsic diffusion originates from the Brownian motion that tends to cause the DNA streams to diffuse across the nanofilter constrictions along the x-direction. The stream widening associated with the intrinsic diffusion is approximately linearly proportional to the separation time. The convective dispersion is a more complicated term [16], and it is believed that the convective dispersion inside the nanofilter array is related to the number of nanofilters the biomolecules crossed during the separation. Therefore, increasing the horizontal field E_x resulted in longer separation time and larger deflection angles (more nanofilters crossed), both effects leading to wider spreading of the streams.

The vertical electric field E_y also affects the stream deflection angle θ. As E_y was raised from 25 V/cm to 75 V/cm at fixed E_x=35 V/cm (**Fig. 5.4D–F**), the DNA stream pattern became more focused with shorter DNA fragments (50 bp, 150 bp) shifting towards the negative *x*-direction and longer DNA fragments (300 bp, 500 bp, 766 bp) shifting towards the positive *x*-direction. A greater vertical field E_y shortens the time for DNA to explore the transition through a nanofilter threshold, and therefore reduces the nanofilter passage rate P_x. This explains the behavior of short DNA with increased E_y. The long DNA fragments shifted with E_y in ways not yet fully understood, although the changes were reproducible with E_y up to 125 V/cm (data not shown). We suspect this phenomenon might be due to the slight non-uniformity of E_x and E_y over the ANA.

We can calculate the coefficient of variation (*CV*) to estimate the size selectivity of the ANA [17]. The *CV* of biomolecules with molecular weight *m* is defined as $\sigma_\mathrm{m}/m\times100\%$, where σ_m is the standard deviation (±s.d.) of *m*. When used as a measure for size selectivity, *CV* is calculated according to $CV = \sigma_m / m = (dm/d\theta \cdot \sigma_\theta)/m$, where θ is the measured deflection angle, as a function of *m*, and σ_θ is the ±s.d. of the deflection angle derived from the stream half-width. From the fluorescence intensity profile of **Fig. 5.4B**, the coefficients of variation for the 150 bp, 300 bp, and 500 bp DNA stream profiles are 8.6, 6.0, and 4.5%, respectively. Therefore, the size selectivity of the ANA in the Ogston sieving regime is about 5 nm (corresponding to the end-to-end distance of 20 bp dsDNA). The separation efficiency of the ANA can be further characterized by the effective peak capacity n_c that defines the maximum number of separated streams that fit into the space provided by the separation. The effective peak capacity n_c is calculated based on some specified separation resolution value R_s of adjacent streams. In the ANA, the effective peak capacity n_c for adjacent streams separated at R_s=1 is calculated as $n_c = [5000 \cdot (\tan\theta_n - \tan\theta_1) + 2 \cdot \bar{\sigma}_W]/(4 \cdot \bar{\sigma}_W)$, where θ_1 and θ_n denote the smallest and greatest stream deflection angles, respectively, $\bar{\sigma}_W$ is the mean of ±s.d. of stream widths, and 5000 μm is the width of the rectangular ANA. **Figure 5.6** shows the dependence of n_c on the horizontal field E_x for the Ogston sieving regime where n_c initially increased quickly with E_x and then leveled off with an upper bound value of about 17. This asymptotic behavior of n_c can be largely attributed to the DNA stream widening with increased E_x, which cancels out the increased lateral separation between the streams.

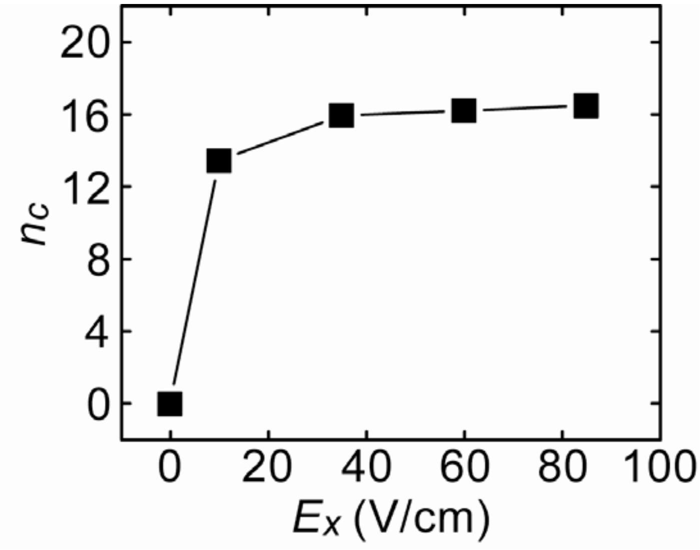

Figure 5.6: Dependence of the effective peak capacity n_c on the horizontal electric field E_x at fixed E_y=25 V/cm. Data are taken for the PCR marker sample separated in the ANA with the Ogston sieving regime.

5.6 Entropic trapping for continuous-flow separation of long DNA

The ANA can separate long DNA molecules based on the entropic trapping mechanism. We prepared a mixture of long DNA molecules (the λ DNA−Hind III digest) in TBE 5× buffer, which contains 6 DNA fragments with sizes ranging from 2,027 bp to 23,130 bp and corresponding equilibrium (unconfined) radii of gyration R_g of about 140 nm to 520 nm [18]. These equilibrium radii of gyration are useful estimates of the spherical DNA size, and they are all greater than the nanofilter constriction depth d_s. Therefore, the nanofilter jump dynamics involves necessarily the deformation and hernia nucleation (*i.e.*, entropic trapping). With application of the horizontal field E_x=185 V/cm and the vertical field E_y=100 V/cm, λ DNA−Hind III digest was separated in less than 1 min with base-line resolution (**Fig. 5.7A−B**; note that the shortest 2,027 bp fragment was too dim for clear visualization in **Fig. 5.7**, but with higher gain setting and longer exposure time of the charge-coupled device (CCD), the 2,027 bp fragment was identified to be base-line separated with the others). A closer look at the fluorescence photographs further revealed that, as expected, longer DNA fragments followed more deflected migration trajectories than shorter ones, a clear distinction of entropic trapping from Ogston sieving. The streams of λ DNA−Hind III digest followed more deflected and resolved trajectories as E_x was increased (**Fig. 5.7C−F**). This observation is consistent with the argument that increased horizontal field E_x lowers the activation energy barrier height leading to a higher jump passage rate P_x [4].

In all the experiments with the λ DNA−Hind III digest, we have observed a threshold value for the horizontal electric field, $E_{x,c}$ (~15 V/cm), below which long DNA molecules were virtually completely confined in the injection deep channels (**Fig. 5.8**).

This threshold phenomenon is likely due to the difficulty of hernia formation in the low field regime, since the nanofilter constriction size of 55 nm (d_s) is already comparable to the DNA persistence length [19]. Therefore, under low horizontal electric field where $E_x<E_{x,c}$, it is difficult for long DNA molecules to initiate hernia nucleation and jump across the nanofilter constriction. Our observation of the threshold field is also consistent with the one-dimensional entropic trap array developed by Han and Craighead, where they have used such phenomenon as effective ways for long DNA focusing and launching in the entropic trap array [20].

We plotted the stream deflection angle θ and the stream half width as a function of DNA length in **Fig. 5.9**. It can be seen clearly from **Fig. 5.9** that, the lateral separation between the long DNA fragments were improved as E_x was increased. However, the stream widening in the ANA for entropic trapping shows a more complex behavior than for Ogston sieving. Increasing E_x resulted in wider spreading of the streams of long DNA, and such stream widening was more profound for longer DNA molecules under larger horizontal electric fields (**Fig. 5.9**). It is a known fact that, for entropic trapping, the stream broadening in the ANA is not dependent on the intrinsic diffusion of the long DNA, since the existence of entropic barriers virtually blocks the diffusion across the nanofilter constriction along the orthogonal *x*-direction. Therefore, we believe our observation here can only be explained by the complex interactions of long DNA with the two-dimensional physical landscape under high electric fields. For example, the possible collisions of long DNA molecules with the supporting pillar can lead to “hook” and “roll-off” events [21, 22]. Such effects can increase dispersion of the long DNA streams dramatically.

We can calculate the effective peak capacity n_c for λ DNA–Hind III digest from the stream deflection angles and stream half widths. n_c is plotted in **Fig. 5.10** as a function of E_x. The n_c curve appears similar to the one observed for Ogston sieving, with an upper bound value of about 15.

Recent Monte Carlo simulations as well as fluorescence microscopy experiments have further suggested that the overall deformation of long DNA molecules approaching a nanofluidic constriction has great effect on entropic trapping, presumably because the DNA deformation affects the hernia initiation process and changes the escape attempt frequency [23, 24]. A quantitative assessment of the jump rate P_x for long DNA molecules in terms of the field strengths and the DNA length is involved and beyond the scope of this thesis. More detailed characterization needs to be conducted in the future to understand the complex dynamics of long DNA deform when crossing a constraining nanofilter and migrating through the ANA.

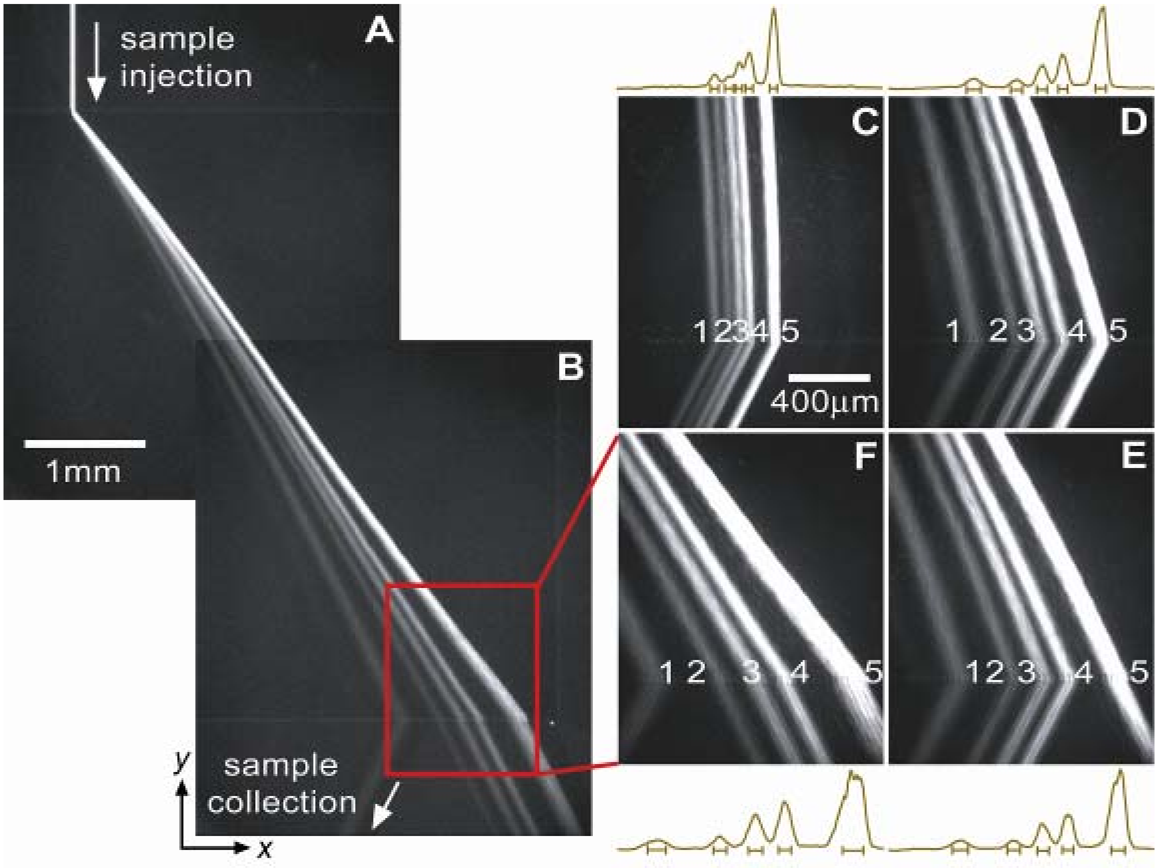

Figure 5.7: Entropic trapping of long DNA (the λ DNA–Hind III digest) through the ANA. Fluorescent photographs show separation of λ DNA–Hind III digest with different electric field conditions. **A**, **B**, **F**, E_x=185 V/cm and E_y=100 V/cm. **C**, E_x=50 V/cm and E_y=100 V/cm. **D**, E_x=145 V/cm and E_y=100 V/cm. **E**, E_x=170 V/cm and E_y=100 V/cm. Band assignments are 2,322 bp (1), 4,361 bp (2), 6,557 bp (3), 9,416 bp (4), 23,130 bp (5). Fluorescence intensity profiles were measured at the ANA bottom edge. The bars underneath the peaks are centered at the means and label the stream widths (±s.d.).

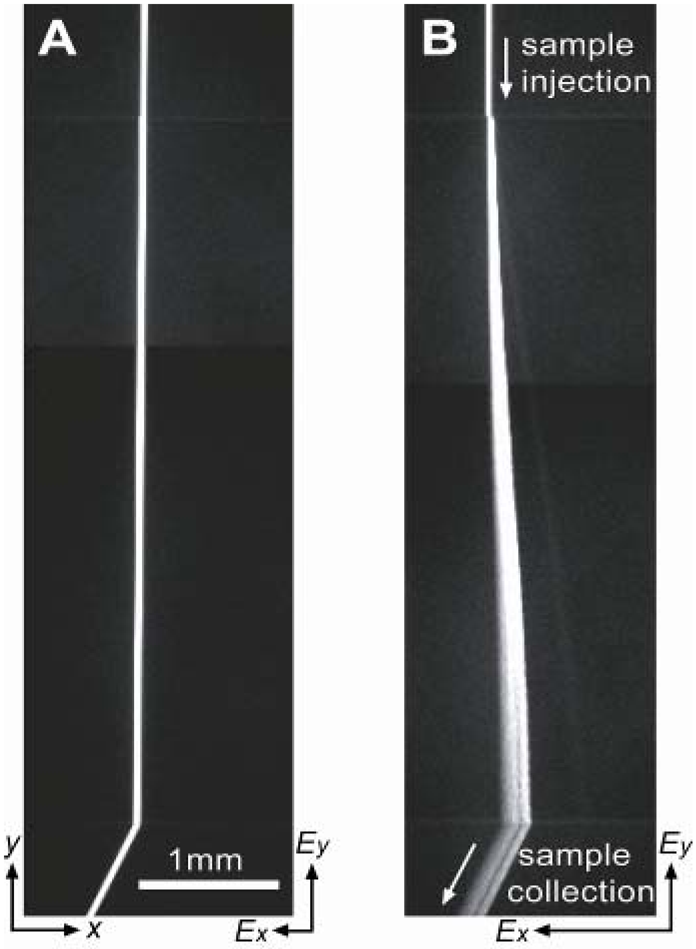

Figure 5.8: Observation of the threshold horizontal field $E_{x,c}$. **A**, Composite fluorescence photograph showing confining of λ DNA−Hind III digest in the initial injection deep channels with E_x=15 V/cm and E_y=25 V/cm. **B**, Composite fluorescence photograph showing DNA molecules starting to jump across the nanofilter with E_x=50 V/cm and E_y=25 V/cm.

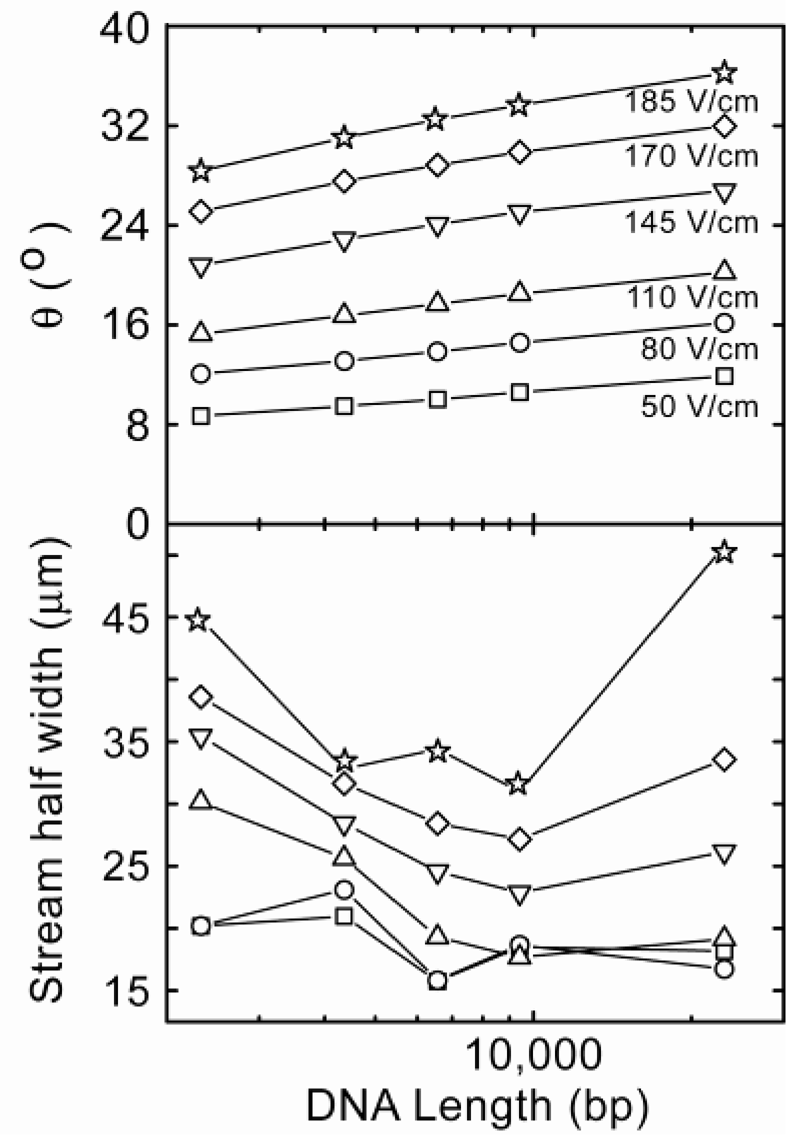

Figure 5.9: Stream deflection angle θ (top) and stream half width ($W/2$, bottom) as a function of DNA length. Data are extracted from separation of the λ DNA−Hind III digest through the ANA with fixed vertical field E_y at 100 V/cm (horizontal field E_x varied as indicated in the figure). The ±s.d. of θ derived from the stream half-width are all less than 1°, so statistical error bars for θ are not plotted.

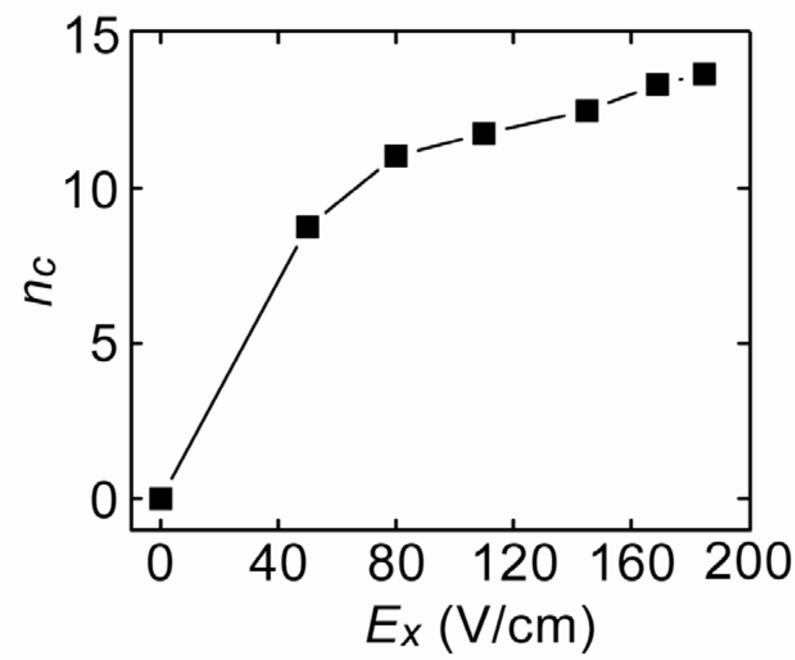

Figure 5.10: Dependence of the effective peak capacity n_c on the horizontal electric field E_x at fixed E_y=100 V/cm. Data are calculated for the λ DNA−Hind III digest separated in the ANA with the entropic entrapping mechanism.

5.7 Size-based separation of proteins with the ANA

The ANA is also capable of separating mixtures of proteins based on their molecular weights (MW), under both denaturing and native conditions. As proof of concept, we first prepared two Alexa Fluor 488-conjugated protein complexes: cholera toxin subunit B (MW~11.4 kDa) and β-galactosidase (MW~116.3 kDa), and denatured them by addition of SDS and DTT. With the horizontal field E_x=75 V/cm and the vertical field E_y= 50 V/cm, the denatured proteins were base-line separated into 2 streams within 2 min. The protein stream widths at 1 mm, 3 mm, and 5 mm from the injection point corresponded to separation resolutions R_s of 0.57, 0.94 and 1.47, respectively (**Fig. 5.11A**). Cholera toxin subunit B was deflected more than β-galactosidase in all the experiments, suggesting Ogston sieving to account for the jump dynamics of these linear denatured protein complexes (**Fig. 5.11B, top**). Further increasing E_x resulted in larger lateral separation between the two streams. However, resolution R_s was compromised due to broader lateral dispersion, as evidenced by the decrease in the resolution curve (**Fig. 5.11B, bottom**).

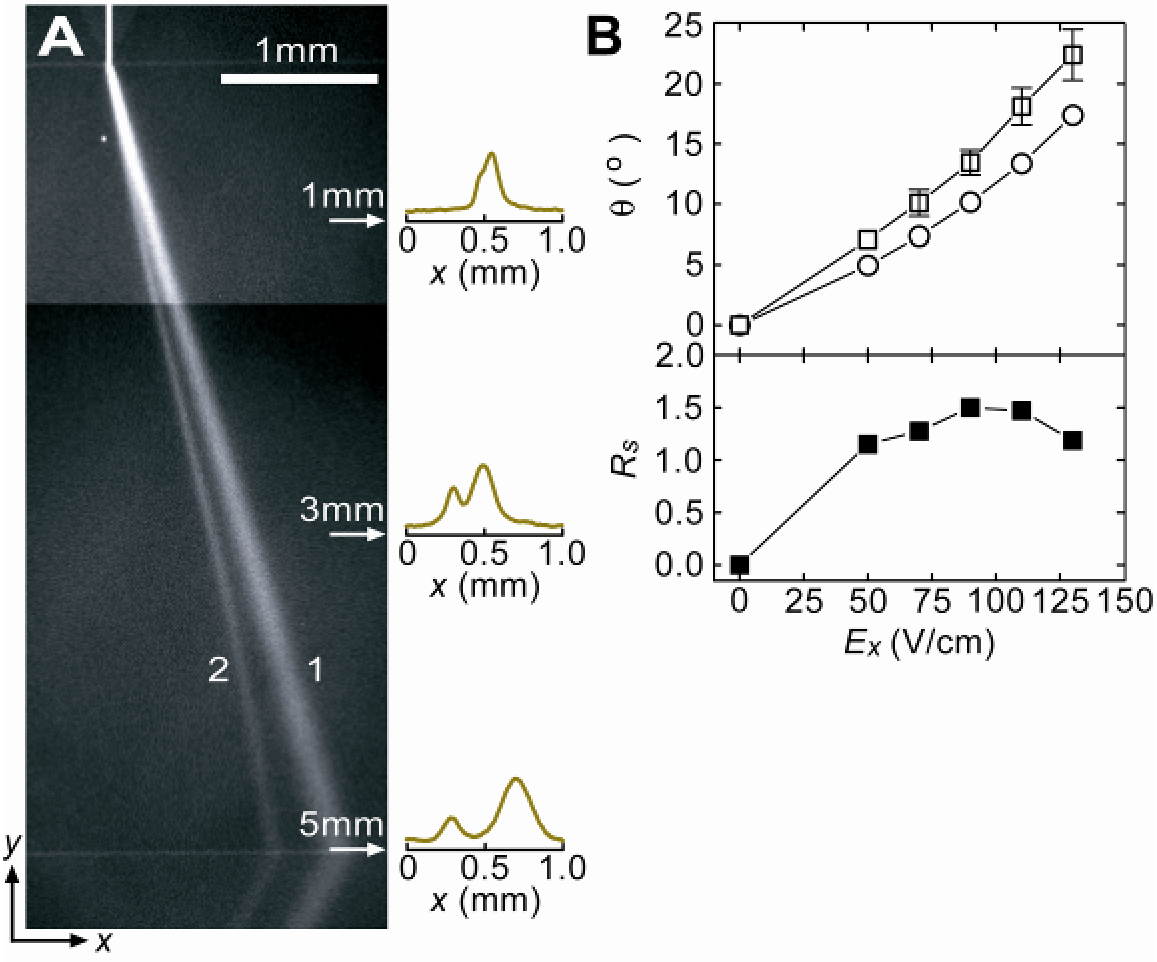

Figure 5.11: Continuous-flow separation of proteins under denaturing conditions through the ANA. **A**, Composite fluorescent photograph showing separation of Alexa Fluor 488-conjugated cholera toxin subunit B (band 1, MW~11.4 kDa) and β-galactosidase (band 2, MW~116.3 kDa) with E_x=75 V/cm and E_y= 50 V/cm. The protein stream widths at 1 mm, 3 mm, and 5 mm from the injection point corresponded to resolutions R_s of 0.57, 0.94 and 1.47, respectively. **B**, Measured deflection angle θ (top) of cholera toxin subunit B (□) and β-galactosidase (○) as a function of E_x when E_y=50 V/cm. The bottom shows the corresponding separation resolutions. The ±s.d. of θ are indicated as error bars (drawn if larger than the symbol).

The ANA can also separate proteins under native conditions. We injected lectin from *Lens culinaris* (lentil) (MW~49 kDa) and B-phycoerythrin (MW~240-kDa) into the ANA at TBE 5×. **Figure 5.12** shows the fluorescence photographs taken for the same ANA area but with different fluorescence filter sets (B-phycoerythrin with a Texas Red filter set and lectin with a FITC filter set). Under different electric field conditions, the two proteins were clearly separated into two distinct streams according to their molecular weight, and non-specific adsorption of the proteins on the ANA was not significant, possibly due to electrostatic repulsion from the like charged hydrophilic ANA walls. In all the experiments, lectin was deflected more than B-phycoerythrin, suggesting Ogston sieving to account for the separation of native proteins in the ANA.

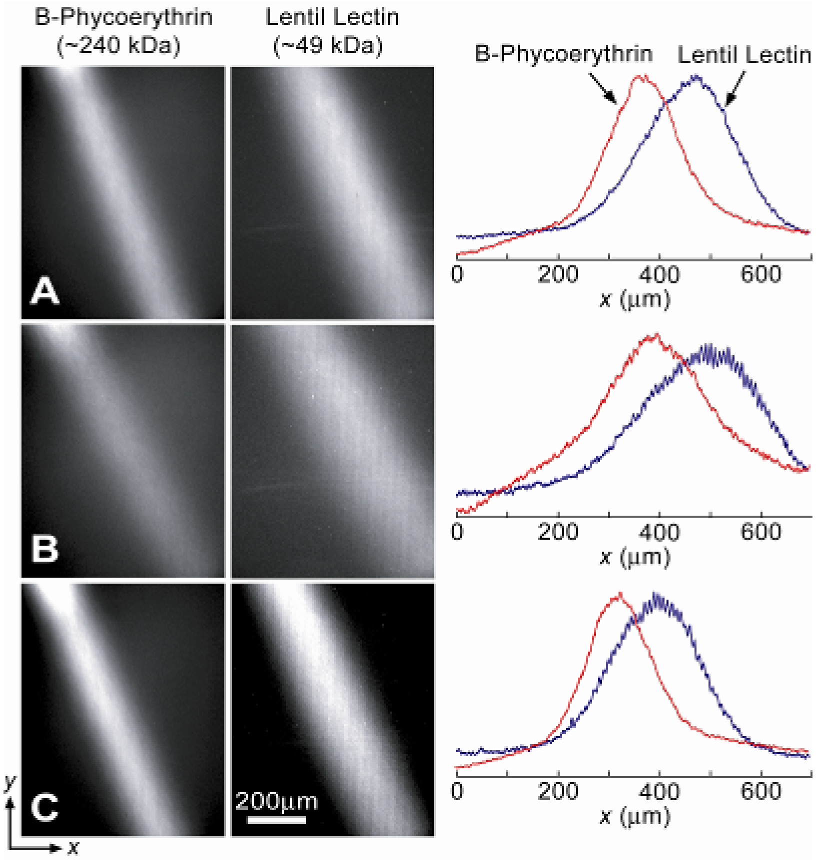

Figure 5.12: Continuous-flow separation of *Lens culinaris* (lentil) (MW~49 kDa) and B-phycoerythrin (MW~240-kDa) under native conditions through the ANA. **A**, E_x=150 V/cm and E_y= 100 V/cm. **B**, E_x=200 V/cm and E_y= 100 V/cm. **C**, E_x=200 V/cm and E_y= 125 V/cm.

5.8 Theoretical modeling of field-dependent stream deflection angles

In this section, we will introduce a course-grained kinetic model to explain the field-dependent stream deflection angle θ in the Ogston sieving regime. As discussed before, in the Ogston sieving regime, the nanofilter jump passage rate P_x for short DNA of a bp number N can be calculated based on the equilibrium partitioning theory and the Kramers rate theory. In the limit of low field, the passage rate P_x is proportional to $E_x^2 K/N$, where K is the DNA equilibrium partitioning coefficient that is calculated as the ratio of accessible microscopic configuration state integrals within shallow and deep regions across the nanofilter. Therefore, the relative mobility μ_x^* along the x-axis across the nanofilters can be calculated as (see Eq. (4.21))

$$\mu_x^* = (1+\frac{\alpha' N}{E_x K})^{-1} \tag{5.2}$$

where α' is a constant with a unit of V/(m·bp). By definition, μ_x^* is the ratio between the mobility μ_x along the x-axis and the maximum sieving free mobility $\mu_{x,max}$ across the nanofilter array. Thus, the tangent of the stream deflection angle θ can be approximately written as

$$\tan\theta = \frac{V_x}{V_y} = \frac{\mu_{x,\max}}{\mu_0}\cdot\frac{E_x}{E_y}\cdot\mu_x^* = \frac{\mu_{x,\max}}{\mu_0}\cdot\frac{E_x}{E_y}\cdot(1+\frac{\alpha' N}{E_x K})^{-1} \tag{5.3}$$

where V_x and V_y are the migration velocities along the positive x- and negative y-axis, respectively, and μ_0 is the DNA free draining mobility in the nanofilter array. In Eq. (5.3), we have implicitly assumed that DNA fragments preserve their free draining property in the ANA deep regions along the y-axis, therefore $\mu_y=\mu_0$. $\mu_{x,max}/\mu_0$ depends solely on the structural parameters of the ANA, and $\mu_{x,max}/\mu_0=4d_s d_d/(d_s+d_d)^2=0.52$ for the ANA tested in the experiments. The equilibrium partitioning coefficient K can be calculated using Eq.

(4.16). In the limit of short DNA ($N \rightarrow 0$), Eq. (5.3) becomes $\tan\theta = 0.52 E_x / E_y$, which indicates a maximum sieving free case in the ANA. The experimental data of $\tan\theta$ for the PCR maker sample in the Ogston sieving regime reasonably agree with the theoretical curves calculated from Eq. (5.3). The best fitting constant α' was found to be fairly constant for the different DNA fragments. The slight deviation of the theoretical curves from the deflection angle data in the low E_x regime might be attributed to the non-uniformity of E_x and E_y in the ANA.

5.9 Discussion

We have observed direct experimental evidence of an unambiguous transition between Ogston sieving and entropic trapping in the ANA. The trajectories of different-sized DNA molecules are consistent with either Ogston sieving or entropic trapping. Crossover from Ogston sieving to entropic trapping is between 1000 bp and 2000 bp, which is concurrently with the DNA rod-like conformation to coiled conformation transition and is consistent with observations in one-dimensional nanofilter arrays. No saturation plateau was observed for entropic trapping in the ANA, in contrast to the one-dimensional nanofilter array, indicating possible separation of long DNA in the ANA over an even broader size range. This different observation might be attributed to the more complex structural geometry of the ANA. In addition, the two-dimensional anisotropic energy landscapes of the ANA is modulated by the two independent orthogonal fields E_x and E_y; therefore, the local nanofilter jump dynamics of biomolecules is critically different from in the one-dimensional nanofilter array. It is largely unknown how our understanding of the local nanofilter jump dynamics in one-dimensional nanofilter array applies to the ANA. The effects of the two actively modulated orthogonal fields as well as all the ANA structural parameters need to be considered for a quantitative understanding of the different separation modes.

The separation efficiency of the ANA can be further improved by increasing separation distance. An optimized ANA structure with a gradient of decreasing constriction size along the positive *x*-direction (an equivalent “gradient gel”) should also provide better resolution and separate proteins over a wider molecular weight range, similar to the effect of gradient-SDS gels for protein separation [25, 26]. Incorporating gate electrodes on the nanofilter walls can allow for additional active adjustment of the surface potential, thus introducing a new degree of control to enhance the sieving across the nanofilter [27, 28].

Other regular sieving structures for continuous-flow sorting of long DNA molecules and microspheres have been reported recently (see discussions in Chapter 1); however, none of these techniques has demonstrated separation of smaller, physiologically-relevant macromolecules, such as proteins, as we reported here. The ANA also represents a significant advance compared to the one-dimensional nanofilter arrays, since the continuous-flow operation of the ANA permits continuous-harvesting of the subset of biomolecules of interest to enhance the specificity and sensitivity for downstream biosensing and detection, which is highly desirable for integrated bioanalysis microsystems because of the low sample throughput. In addition, separation speed and resolution in one-dimensional nanofilter arrays cannot be both enhanced without compromising each other, while in the ANA, they are mainly modulated by the two independent fields E_x and E_y, respectively. Therefore, careful regulation of both E_x and E_y can always achieve rapid separation with high resolution at the same time.

The designed structural anisotropy of the ANA is essential for continuous-flow separation. The continuous-flow separation through the ANA should be applicable to any interaction mechanism (either size-, charge-, or hydrophobicity-based) along the orthogonal *x*-direction that can lead to differential transport across the nanofilters. The high-resolution separation and ease of sample collection may prove useful for preparative separation of complex biological samples, which has promising implications for proteomic research and biomarker discovery [29, 30]. The sample throughput of the ANA can be further scaled up by parallelism with multi-device processing. We believe the ANA can be used as a generic sieving structure to separate other particles of interest with nanoscale dimensions, including nanoparticles and nanowires, viruses and cell organelles. In addition, we envisage it is possible to develop anisotropic gel- or membrane-based large-scale biomolecule separation systems operating in the continuous-flow mode by introducing structural anisotropy by either photo-patterning anisotropic gel structures or stacking membranes in layers [31].

5.10 References

1. Fu, J. & Han, J. A nanofilter array chip for fast gel-free biomolecule separation," *Proc. Micro Total Analysis Systems 2005*, 1531—1533 (2005).
2. Fu, J. & Han, J. Continuous-flow biomolecule separation through patterned anisotropic nanofluidic sieving structure. *Proc. Micro Total Analysis Systems 2006*, 519—521 (2006).
3. Fu, J., *et al.* A patterned anisotropic nanofluidic sieving structure for continuous-flow separation of DNA and proteins. *Nature Nanotech.* **2**, 121—128 (2007).
4. Han, J., Turner, S. W. & Craighead, H. G. Entropic trapping and escape of long DNA molecules at submicron size constriction. *Phys. Rev. Lett.* **83**, 1688—1691 (1999).
5. Fu, J., Yoo, J. & Han, J. Molecular sieving in periodic free-energy landscapes created by patterned nanofilter arrays. *Phys. Rev. Lett.* **97**, art. no. 018103 (2006).
6. Giddings, J. C., Kucera, E., Russell, C. P. & Myers, M. N. Statistical theory for the equilibrium distribution of rigid molecules in inert porous networks. Exclusion chromatography. *J. Phys. Chem.* **72**, 4397—4408 (1968).
7. Smith, F. G. & Deen, W. M. Electrostatic effects on the partitioning of spherical colloids between dilute bulk solution and cylindrical pores. *J. Colloid Interface Sci.* **91**, 571—590 (1983).
8. Deen, W. M. Hindered transport of large molecules in liquid-filled pores. *AIChE J.* **33**, 1409—1425 (1987).
9. Nykypanchuk, D., Strey, H. H. & Hoagland, D. A. Brownian motion of DNA confined within a two-dimensional array. *Science* **297**, 987—990 (2002).
10. Slater, G. W., Gratton, Y., Kenward, M., McCormick, L. & Tessier, F. Deformation, stretching, and relaxation of single-polymer chains: fundamentals and examples. *Soft Materials* **1**, 365—391 (2003).
11. Huang, L. R. *et al.* Generation of large-area tunable uniform electric fields in microfluid arrays for rapid DNA separation, *Tech. Dig. Int. Elect. Dev. Mtg.*, 363—366 (2002).
12. Huang, L. R. *et al.* A DNA prism: high speed continuous fractionation of large DNA molecules. *Nature Biotech.* **20**, 1048—1051 (2002).
13. Lide, D. R. *CRC Handbook of Chemistry and Physics* (Taylor and Francis, Boca Raton, FL, ed. 87, 2007).
14. Hagerman, P. J. Flexibility of DNA. *Annu. Rev. Biophys. Biophys. Chem.* **17**, 265—286 (1988).
15. Rubenstein, M. & Colby, R. H. *Polymer Physics* (Oxford, New York, 2003).
16. Bow, H., Fu. J., Rothman, C. & Han, J. Characterization and optimization of patterned nanofilter arrays for biomolecule separation. submitted to *Analytical Chemistry*, Nov. 2006.
17. Huang, L. R., Cox, E. C., Austin, R. H. & Sturm, J. C. Continuous particle separation through deterministic lateral displacement. *Science* **304**, 987—990 (2004).
18. Smith, D. E., Perkins, T. T. & Chu, S. Dynamical scaling of DNA diffusion coefficients. *Macromolecules* **29**, 1372—1373 (1996).
19. Åkerman, B. Barriers against DNA-loop formation in a porous matrix. *Phys. Rev. E* **54**, 6685—6696 (1996).

20. Han, J., & Craighead, H. G. Separation of long DNA molecules in a microfabricated entropic trap array. *Science* **288**, 1026─1029 (2000).
21. Viovy, J.-L. Electrophoresis of DNA and other polyelectrolytes: physical mechanisms. *Rev. Mod. Phys.* **72**, 813─872 (2000).
22. Randall, G. C. & Doyle, P. S. Electrophoretic collision of a DNA molecule with an insulating post. *Phys. Rev. Lett.* **93**, art. no. 058102 (2004).
23. Tessier, F., Labrie, J. & Slater, G. W. Electrophoretic separation of long polyelectrolytes in submolecular-size constrictions: a Monte Carlo study. *Macromolecules* **35**, 4791─4800 (2002).
24. Nykypanchuk, D., Strey, H. H. & Hoagland, D. A. Brownian motion of DNA confined within a two-dimensional array. *Science* **297**, 987─990 (2002).
25. Margolis, J. & Kenrick, K. G. Polyacrylamide gel-electrophoresis across a molecular sieve gradient. *Nature* **214**, 1334─1336 (1967).
26. Scopes, R. K. *Protein Purification, Principles and Practice* (Springer-Verlag, New York, ed. 3, 1993).
27. Karnik, R., Castelino, K. & Majumdar, A. Field-effect control of protein transport in a nanofluidic transistor circuit. *Appl. Phys. Lett.* **88**, art. no. 123114 (2006).
28. Eijkel, J. C. T. & van den Berg, A. Nanotechnology for membranes, filters and sieves. *Lab Chip* **6**, 19─23 (2006).
29. Wulfkuhle, J. D., Liotta, L. A. & Petricoin, E. F. Proteomic applications for the early detection of cancer. *Nat. Rev. Cancer* **3**, 267─275 (2003).
30. Righetti, P. G., Castagna, A., Herbert, B. Reymond, F. & Rossier, J. S. Prefractionation techniques in proteome analysis. *Proteomics* **3**, 1397─1407 (2003).
31. Fu, J. & Han, J. Continuous biomolecule separation in a nanofilter structure. United States Patent P-8195-USP, priority date 5 October 2006.

Chapter 6

Conclusions and future work

6.1 Thesis contributions

Direct analysis of biologically-relevant entities such as nucleic acids and proteins offers the potential to outperform conventional molecular analysis techniques and diagnostic methods through enhancements in speed, accuracy, and sensitivity. Moreover, direct biomolecule observations and manipulations help investigators probe fundamental molecular processes in biochemistry and biophysics that are often easily obscured in ensemble assays. Nanofluidic systems with critical dimensions comparable to the molecular scale open up new possibilities for direct observation, manipulation and analysis of biomolecules (single or ensemble), thus providing a novel basis for ultra-sensitive and high-resolution sensors and medical diagnostic systems. Inspired by this concept, this doctoral dissertation has centered on developing a new class of nanofluidic devices for rapid separation and analyses of biologically-relevant macromolecules, such as dsDNA, proteins, and carbohydrates. As a substantial step towards this long-term functional objective, we have proven, for the first time that nanofluidic structures can serve as controllable molecular sieves for analytical and preparative separation of various physiologically-relevant macromolecules (including proteins). We have successfully designed and fabricated a one-dimensional nanofluidic filter array to achieve high-speed analytical separation of dsDNA and proteins based on the Ogston sieving mechanism. The achieved separation speeds and resolution of these one-dimensional nanofluidic filters match the performance characteristics of current state of the art systems (*i.e.*, capillary gel electrophoresis) while at the same time eliminating the need to incorporate sieving gels into the device. In addition, we have successfully conducted theoretical studies of the Ogston sieving process of biomolecules in the context of the periodic free-energy landscapes created by the patterned nanofluidic filter arrays. The kinetic model constructed based upon the equilibrium partitioning theory and the Kramers rate theory properly describes the field-dependent sieving behavior of biomolecules, presenting notable progress beyond the existing equilibrium model (i.e., the so called "extended Ogston model") for Ogston sieving in conventional gels.

In this thesis, we have also designed and fabricated a widely-applicable anisotropic nanofluidic structure consisting of a two-dimensional periodic nanofluidic filter array (Anisotropic Nanofilter Array: ANA). The nano-engineered structural anisotropy manifested through orthogonally arranged sieving structures in the ANA causes biomolecules of different sizes to follow distinct migration trajectories, leading to efficient continuous-flow separation. Using this device, continuous-flow Ogston sieving-based separation of short DNA and proteins as well as entropic trapping-based separation of long DNA were achieved in minutes, thus elucidating the ANA's potential as a standard sieving structure for use in an integrated biomolecule sample preparation and analysis system. The continuous-flow operation of the ANA permits continuous-harvesting of biomolecule subsets, thus enhancing the specificity and sensitivity of downstream biosensing and detection. This operational characteristic presents beneficial implications for proteomic research and biomarker discovery. More importantly, the engineered anisotropic sieve design in the ANA represents a significant conceptual advance for molecular manipulation and separation, and the continuous-flow separation through the ANA should be applicable to any interaction mechanism (either size-, charge-, or hydrophobicity-based) that can lead to differential transport across the nanofluidic filters [1]. The conceptual advances of the ANA have already generated great interest from numerous scientific disciplines. This thesis work has been cited in a host of different review articles where it has been proclaimed "the most exciting and promising area for development over the coming years" [2].

More specifically, the contributions of this thesis include:

- We discovered for the first time Ogston sieving in a regular nanofluidic system. We demonstrated fast analytical separation of physiological-relevant biomolecules such as proteins. We demonstrated a clear roadmap for further separation improvement.
- We constructed a kinetic model based on the equilibrium partitioning theory and the Kramers rate theory to explain molecular sieving process across nanofluidic constrictions.
- We demonstrated unambiguous crossover from Ogston sieving to entropic trapping by using the regular nanofluidic sieving structures.
- We invented a widely-applicable two-dimensional anisotropic nanofluidic sieving structure for continuous-flow biomolecule separation.
- We demonstrated for the first time rapid continuous-flow separation of dsDNA molecules and proteins covering broad biological size scales.

☐ We constructed a course-grained kinetic model to explain field-dependent stream deflection angle through the two-dimensional anisotropic nanofluidic sieving structure.

6.2 Directions for future research

The development of artificial sieving structures represents a major step towards optimizing biomolecule separation methods and integrating them within other bioanalysis microsystems. The design flexibility and precise control over geometries within nanofluidic sieves constitute key advantages offered by artificial regular structures when compared to conventional random gel-based media. This doctoral work has clearly elucidated this advantage, as we have designed and implemented various nanofluidic sieving structures for rapid analysis of dsDNA and proteins covering broad size scales. It is of great interest to further pursue this research direction by designing artificial molecular sieves with more elaborate geometries while simultaneously examining novel sieving mechanisms to improve biomolecule separation. We could potentially design a molecular sieving structure with heightened size selectivity and a bias toward limited band broadening to enhance sample separation. In addition to biomolecule separation, artificial nanofluidic structures ideally serve theoretical studies of molecular dynamics and stochastic motion in confining spaces due to their precisely characterized on-chip environments. The transport properties of macromolecules through a constraining nanofluidic medium are largely affected by the molecular interactions with the confining physical landscape and the macromolecules' different responses to the external driving forces. In particular, studies of the jump dynamics of biomolecules with effective diameters smaller than the nanofluidic constriction size (i.e., Ogston sieving) have great implications for designing future artificial sieves to achieve rapid analytical separation of proteins, carbohydrates, and hormones. Such investigations and characterization could potentially aid in developing cheaper and more accurate screening and diagnostic medical devices. It would be interesting to further improve separation efficiency of the one-dimensional nanofluidic filter arrays developed in this doctoral thesis, by scaling down the nanofluidic filter structures (period, gap size, etc.) with advanced sub-100 nm resolution lithography techniques.

Incorporating gate electrodes on the nanofluidic walls can allow for additional active control of the surface potential, thus introducing a new degree of control to enhance the electrostatic interaction across the nanofluidic channel. It is possible to utilize the Debye layer, electro-osmosis, and surface chemistries, together with nanofluidic geometrical constraints, to achieve novel biomolecule separation based on a suite of molecular properties (e.g. size, charge or hydrophobicity). The two-dimensional anisotropic nanofilter array (ANA) we designed and fabricated serves as an ideal platform for these studies, since surface treatment of the ANA is straightforward, and its fabrication process is compatible with other semiconductor microfabrication techniques that would be necessary to incorporate gate electrodes on the nanochannel walls.

6.3 References

1. Austin, R. Nanofluidics: a fork in the nano-road. *Nature Nanotech.* **2**, 121─128 (2007).
2. Eijkel, J. C. T. & van den Berg, A. Nanotechnology for membranes, filters and sieves. *Lab Chip* **6**, 19─23 (2006).